LAYER BASED MANUFACTURING OF FUNCTIONAL MATERIALS AND COMPONENTS

Thesis submitted in accordance with the requirements of
the University of Liverpool for the degree of Doctor in
Philosophy

By

Adam Thomas Clare

April 2009

ABSTRACT

This thesis examines the potential for using new manufacturing techniques to process functional materials.

Within this remit several combinations of processes and materials have been investigated to establish firstly, so called smart functionality. That is functional materials which are responsive to their environment and secondly suitability to specific engineering applications. These include; shape memory springs/cantilevers, piezoelectric pads/films and mass spectrometer components. The manufacturing techniques employed within this work are usually exploited within the areas of so called rapid prototyping or rapid manufacture. Due to the complex geometries, nested features and high tolerance of parts which can be manufactured with these techniques manufacturing novel structures in this way has become of great interest.

This thesis demonstrates that layer based manufacturing techniques can be employed to produce parts made of smart materials which exhibit a controllable functionality.

Selective Laser Melting (SLM) has been used to produce high aspect ratio NiTi components which exhibit the shape memory effect. Details of the design of functional parts produced in this way are presented.

A second area considers the use of selective laser melting of the piezoelectric material $BaTiO_3$ in different forms/composites. The use of laser manufacturing techniques to produce consolidated parts is discussed and the effect of processing on the microstructure is described.

Lastly Digital Light Projection (DLP) has been used to produce precision polymeric components for mass spectroscopy applications. The incorporation of metallised parts produced in this way is also examined. The resulting quadrupole mass spectrometer is shown to compete favourably with those produced by conventional means.

CONTENTS

ACKNOWLEDGEMENTS

I would like to sincerely thank Prof P.R. Chalker for his supervision throughout the experimental and written stages of this work. I will be forever indebted to him for this opportunity.

The words of advice, questions, problems, thoughts, wisdom and tinkering of Dr R.T. Murray must also be acknowledged. Tuesday lunchtimes will never be the same again.

The kind contributions made by other academic staff at The University of Liverpool should also be acknowledged. These include; Dr C.J. Sutcliffe who facilitated apparatus and accommodated many interesting lines of investigation, Dr P. Fox for his expert consultations regarding all things metallic and Dr R. Potter for assistance with the preparation of this thesis.

Technical members of staff including Dr P. Beahan, Mr L. Bailey and Mr D. Atknson are thanked for their help, ensuring apparatus was not damaged and I didn't hurt myself. Mrs M. Robinshaw is also thanked for her help with binding and arranging this work.

Finally, I would like to thank friends and colleagues who provided a great atmosphere in which to work and study; Dr D. Potter, Dr K. Black, Dr L. Lari, Dr S. Davies, Mr Z. Fang, Mr N. Pham, Mr P. King, Mr K. Dawson. I look forward to reading my name in your acknowledgements!

LIST OF FIGURES

LIST OF TABLES

PUBLICATIONS

[1] Chalker, P. R., Clare A.T, et al. (2006). Selective Laser Melting of High Aspect Ratio 3D Nickel-Titanium Structures for MEMS Applications. *Surface Engineering for Manufacturing Applications.*

[2] Clare A.T, Chalker P.R et al (2007). Selective laser melting of high aspect ratio 3D nickel–titanium structures two-way trained for MEMS applications. *International Journal of Mechanics and Materials in Design*

[3] Clare A.T, Chalker P.R et al (2007). Selective Laser Sintering of Barium Titanate – Polymer Composite Films. *Journal of Materials Science*

[4] Hauser C, Clare A.T et al (2008). Rotational 3D Printing of Sensor Devices Using Reactive Ink Chemistries. *Solid Freeform Fabrication Proceedings Austin, Texas.*

[5] Chalker, K.M. Berggreen, A. T. Clare, J. Singh, and C.J. Sutcliffe (2008). Rapid prototyping methodologies for ceramic micro components, *Journal of Solid State Phenomena.*

[6] Brkić B, France N, Clare A. T, Sutcliffe C. J, Chalker P. R and Taylor S (2008), Towards Portable Mass Spectrometry: Design, Simulations, Fabrication and Testing of a Miniature Quadrupole Mass Spectrometer, *Proceedings of the 30th Annual BMSS Meeting*, University of York.

---

[7] Brkić B, France N, Clare A. T, Sutcliffe C. J, Chalker P. R and Taylor S (2009), Development of Quadrupole Mass Spectrometers using Rapid Prototyping Technology, *Journal of the American Society of Mass Spectrometry.*

[8] Hauser C, Clare A.T, Taylor S, Chalker P.R, Sutcliffe C.J, Brkić B. (2009) Rapid Manufacture of Quadrupole Mass Spectrometers, *Proceedings of the 4th Rapid Manufacturing Conference,* University of Loughborough.

[9] A.T. Clare, C. Hauser, S. Taylor, P.R. Chalker, C.J. Sutcliffe, B. Brkic, N. France (2009) [PEND] Rapid Manufacture for Custom Mass Filter Electrodes, *Rapid Prototyping Journal.*

NOMENCLATURE

A	area
c	compliance
D	electric charge displacement
d	piezoelectric strain coefficient
E	Young's modulus
e	electric field strength
E_ρ	energy density
f	volume fraction
G	Gibb's free energy
H	enthalpy
H^*	volumetric enthalpy
L	Length
r	radius
S	entropy
S^*	volumetric entropy
T	temperature
p	pressure
V	Voltage
v	volume
v	velocity
P_ρ	power density
x	linear dimension

ε	strain
$\in$	electrical permittivity
σ	stress

1. Introduction

FORWARD

Microelectromechanical systems will, by definition, incorporate some electro-mechanical transduction. Like large scale conventional engineering systems these must be controlled and powered. This may be hampered by their small size and as a consequence ‘conventional’ design approaches are often impractical. To overcome this, the designer may use functional materials such as shape memory alloys or piezoelectrics which avoid some of the power/control issues. These materials respond to changes in temperature and voltage respectively to exhibit automatic mechanical actuation.

Incorporation of functional materials into micro-scale devices adds a level of complexity in terms of design and manufacture. Not only does the manufacturing technique need to yield sub-millimetre feature sizes but also sub-micron tolerances.

The emergence of so-called ‘2½D’ techniques exploited by several rapid prototyping methods, has generated much interest in their application to micro scale manufacturing. The generic 2½D technique involves the following process flow:-

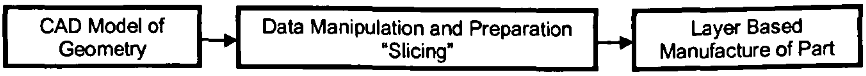

These methods allow complex nested features to be manufactured which would be impossible by other techniques.

The use of layer based manufacturing techniques to process functional materials is in its infancy and constitutes the body of research included in this thesis.

The manufacturing techniques investigated within this thesis are Selective Laser Melting (SLM) and Digital Light Processing (DLP). The former emerged in the mid 1980's and is a technique which involves scanning a laser over a powdered feed stock causing it to melt and fuse selectively with the material around it forming a solid layer. This is repeated layer-by-layer to form the desired 3D component.

DLP is also a layer based technique. However, it employs a Digital Micro-mirror Device (DMD), first produced by Texas Instruments™ in 1987, to create a dynamic mask. The controlled actuation of micro mirrors in a DMD microchip projects light into a photosensitive material causing it to selectively cure, forming a layer of the part. The process is repeated to construct the whole component layer-by-layer.

Components have been manufactured from the functional materials NiTi and $BaTiO_3$ using these methods. The manufactured parts have been subject to material analysis to evaluate the microstructure they exhibit relative to the feed stock material. These analytical techniques include Differential Scanning Calorimetry (DSC), Transmission Electron Microscopy (TEM), Scanning Electron Microscopy (SEM), X-Ray Diffraction (XRD), Surface Profiling, Raman Spectroscopy and standard mechanical testing techniques.

SCOPE OF THESIS

Chapter Two explores the state-of-the-art of layer based processes and other manufacturing methods, which are capable of fabricating functional components for various applications. It also details how functional materials are currently being incorporated into micro components. The issues raised by combining these technologies are introduced.

The advantages of layer based techniques for manufacture are clearly highlighted and the potential for using these techniques to process functional materials is presented. The functional materials employed in this research are described and their suitability for different engineering applications is examined. Also the issues of using these materials for engineering applications with layer based methodologies are discussed.

Chapter Three describes the experimental methods used within this thesis and their suitability. The analysis of the feed stock material, parameter optimisation of manufacturing techniques, and analysis of the components produced is considered. The SLM technique is described in detail, particularly with a view to processing metal and ceramic materials. Subsequently the analytical techniques used to characterise these materials are discussed.

The DLP technique is described in detail, including consideration of the experiments performed to validate the suitability of this technique to manufacture piezoelectric/acrylic composites. The experimental methodology for improving build parameters is also discussed.

Chapter Four demonstrates how SLM has been used to produce high-aspect ratio NiTi components which exhibit the well known shape memory effect. Analysis of the shape memory alloy after processing, examines the effect of the SLM treatment. Cantilever beams and helical structures made in this way have been trained and actuated to demonstrate the suitability of the process to electromechanical applications. The influence of laser dwell time and raster pitch on the density of NiTi shape memory alloy parts and their resolvable feature sizes are reported. The shape memory properties of solid parts produced by selective laser melting are compared to NiTi alloys resulting from other processes. Furthermore the application of selective laser melted NiTi components in micro-electromechanical systems is discussed. In particular these include applications which require thermal actuation, without the need for signal processing or additional power supply.

Chapter Five examines the use of the piezoelectric material barium titanate ($BaTiO_3$) in polymer composites and in combination with the SLM manufacturing technique to produce sintered parts. This process is extended to fabricate electro-ceramic thin films on silicon substrates. Methods of forming pre-positioned layers of barium titanate are investigated by spin-coating the feedstock powder mixed with a commercial polymer photoresist. The ceramic-polymer composite is then spun coated onto a silicon wafer substrate. This results in a sandwich structure of SiO_2 insulator, Ni conductor and electro-polymer/ceramic. A range of laser power processing conditions was identified in which sintered barium titanate layers could be formed. The laser power was found to be more influential in forming sintered microstructures than laser exposure time. The microstructure of barium titanate films is found to be sensitive to the laser processing conditions, with the optimum laser power densities for the processing of the $BaTiO_3$-polymer found to be in the range 85-100kW/cm^2. This chapter highlights the possibility of using 'direct write' techniques to produce piezoelectric actuators upon silicon substrates. It also details the development of $BaTiO_3$/PVDF-TRFe composite films which demonstrate predictable piezoelectric properties. The approach has advantages over conventional, single constituent, materials designed for electromechanical applications. The mixture of $BaTiO_3$ with a photopolymer matrix is also examined and the implications to optimal build parameters using the DLP process are investigated. Parts built in this way were characterised and their piezoelectric properties quantified.

Chapter Six examines the use of DLP to produce prototype structures for mass spectroscopy applications. The incorporation of piezoelectric and conductive elements produced in this way are also examined which demonstrates the suitability of this process to precision applications.

The penultimate chapter concludes by summarising the major outcomes of this work and introduces a final chapter which proposes themes for future investigations.

2. Literature Review

INTRODUCTION

In this chapter, the fundamental concepts and previously published literature supporting the research included within this thesis is presented. The rationale for manufacturing components by layer based techniques using functional materials is detailed.

The state-of-the-art in the processing of functional materials is discussed. The advantages of using these materials are examined in the context of micro-engineering applications. The functional materials used in this investigation are described and the reasons for selecting specific materials are presented.

This chapter goes on to explore current layer based manufacturing techniques and their suitability for micro manufacturing. The potential for manufacturing 3D geometries from functional materials is considered. These are divided into two principal groups namely, those most suited to the processing of metals and those most suited to processing polymeric materials. Several approaches to 'free form' fabrication are described; however, those of most significance to this work are detailed more completely.

The unique advantages of these novel manufacturing approaches are described. This line of discussion is complimented by an examination of the state-of-the-art in mass spectrometry which is used as a case study later.

Functional Materials for Micro Mechanical Applications

The Shape Memory Effect

The 'so called' shape memory effect in metals was first observed in Au-47.5at% Cd alloys [1] and later similar properties were identified in NiTi alloys [2]. The shape memory effect arises from a solid state phase transformation between a low temperature martensite phase and a high temperature complimentary austenitic phase [3, 4]. Materials with this property can be macroscopically deformed and then subsequent heating causes a microscopic phase change allowing macroscopic shape recovery. The material appears to exhibit some form of 'memory' of the original shape hence the term shape memory effect (SME).

SME materials also exhibit the unique property of superelasticity (SE) in their higher temperature micro structural phase. Materials which exhibit this effect may withstand non-linear elastic strains several times larger in the fully austenitic phase compared with the martensitic.

The special nature of SME materials has allowed their incorporation into a wide range of applications, including valves and springs which exploit them as temperature sensitive actuators. Of greater relevance to this work is the more recent incorporation of SMEs into MEMS type devices. Studies have established that NiTi alloys can be deposited in thin films onto engineering substrates such as silicon [5] while maintaining the SME. These have been adapted to form simple mechanisms such as cantilevers [6, 7] and demonstrate the potential for shape memory alloys (SMAs) to find important roles in future MEMS manufacture.

The microscopic mechanisms of the SME are similar across the family of SMAs. If a simplified situation is first considered in which the micro-structure of these materials may exist in one of two discreet states; the martensitic or the austenitic (sometimes referred to as the parent phase).

The hysteretic behaviour of the phase changes which occur can be understood as a transformation between these two states. Heating of an 'ideal' SMA which is initially in the martensitic phase may provide enough thermal energy to initiate a solid-solid phase change. This begins at the austenitic start temperature (A_S). Further input of thermal energy will result in the material existing in a 100% austenitic phase. This temperature corresponds to the austenitic finish temperature (A_F). The entire process is reversible. Upon cooling, martensite begins to form at (M_S) and further cooling results in the material returning to a 100% martensite structure at (M_F) (Figure 1).

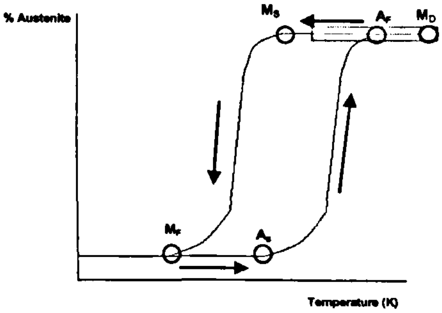

Figure 1 Hysteresis curve associated with phase changes in SMAs.

The extent of SME, SE and the transformation temperatures exhibited by a SMA are highly sensitive to composition, metallurgical treatments and impurities. This sensitivity allows materials to be tailored to give the desired properties suited to a particular application.

The transformation of austenite to martensite is a complex shear-based process. Atomic diffusion does not occur and hence the composition present in the crystallographic phases does not change. The process is athermal, that is to say, at constant temperature within the region $M_S<T<M_F$ no further martensite will be produced and the microstructure

consists of a combination of both martensite and austenite characteristic of that ambient temperature.

The thermodynamic process occurring during phase change is best considered in terms of Gibbs free energy (Figure 2).

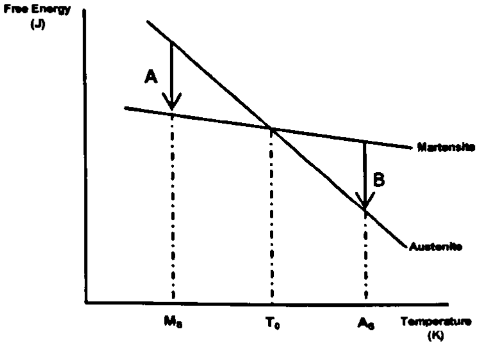

Figure 2 Free energy considerations in SMA phase changes.

In Figure 2 the lines labelled martensite and austenite represent the Gibbs free energy of each respective phase at varying temperatures. Thermodynamic systems have a predisposition to exist at their lowest energy level. Upon achieving this lower energy a corresponding phase change occurs in a SMA. Transitions A and B in Figure 2 represent the energy differences required to cause respective phase changes. This corresponds to;

$$G = U + pV - TS \tag{1.1}$$

Where G is the Gibbs free energy within the system, U is the internal energy, T is temperature and S is the associated entropy. If pressure (p) and volume (V) are assumed to remain constant, this can be simplified to;

$$G = U - TS \tag{1.2}$$

Thus the energy required to cause a phase change within the material must be given by the difference in the respective energies of each phase. This corresponds to a change in the entropy experienced within the crystal structure.

The specific (transformation) mechanism which occurs between phases varies between materials. However, the generic model usually dictates that the martensitic phase can orientate in several crystallographic habit planes whereas the austenitic can only exist in one. The variation in martensitic habit planes comes about through twinning under load. Most crystalline metals when subject to stress will experience dislocation or slip, but SMAs experience martensitic twinning. In other words the applied load causes the splitting of larger martensitic crystals to compositionally identical ones sharing a twin plane. During the process of twinning the material accumulates residual strain until the martensitic variant consistent with maximum strain is fully prevalent. Further loading causes the material to behave in a classically plastic manner. If a simple stress-strain scenario is considered this helps to illuminate the nature of macroscopic recovery in SMA geometries (Figure 3);

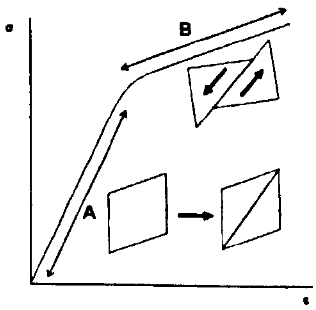

Figure 3 Modes of strain compensation in SMAs.

To experience complete recovery upon heating beyond A_F, the strain induced by mechanical deformation for an SMA must not exceed that depicted by region 'A' in Figure 3. Straining the material beyond this into region 'B' will result in deformation that cannot be recouped by the SME.

At temperatures above M_S, SMAs exhibit the super-elastic effect. This relates to the formation of stress-induced martensite. Although a SMA may be held above a temperature at which the composition should be 100% austenitic, loading at these temperatures causes the formation of martensite, through the same twinning process for sub M_F temperatures. Upon removal of the stress the twinned martensite reverts back to a fully austenitic structure under isothermal conditions. This is best described using the Clausius-Clapeyron relationship [8] which relates the mechanical deformation and the energies associated with phase changes in a SMA above M_S;

$$\frac{d\sigma}{dT} = -\frac{\Delta S^*}{\varepsilon} = -\frac{\Delta H^*}{\varepsilon T} \tag{1.3}$$

Where ε and σ refer to strain and stress inducing the formation of martensite respectively. While S^* and H^* represent volumetric entropy and enthalpy respectively.

Beyond a certain temperature, SE will no longer be observed due to the manifestation of more normal strain compensation mechanisms such as dislocation and block shear along preferential planes and grain boundaries. Therefore the SE is only observed in a temperature range above M_S but lower than the temperature at which martensitic twinning no longer occurs, usually termed 'super elasticity finish temperature'. This leads to a reconsideration of Figure 1 in which the grey region indicates the temperature range over which SE is observed. Much like the SME, these temperatures and degree of SE are dependent upon thermal treatments, mechanical processing and alloying.

It can be inferred that the crystal quality of a SMA for maximum SME and SE must be such that the preferential mode of strain compensation should be through twinning to the highest possible strains, both sub M_S and above A_F [9]. This will lead to the largest recoverable strain via the SME and the highest degree of SE respectively. This property is a valuable design consideration. Hence NiTi alloys are often selected for SME and SE applications apart from their other conventional material properties.

NiTi Alloys

The NiTi alloys stand apart from other SMAs for several reasons. Firstly, the excellent mechanical properties they exhibit.

	Nitinol SE508 Wire	Cu-Al-Ni	1018 Mild Steel
UTS (MPa)	1100-1375	780	200-400
Max Strain	10%	7%	20%

Table 1 Comparison of mechanical properties of Nitinol wire as produced by NDC™ at room temperature with mild steel and Cu-Al-Ni alloys [10].

Secondly, the corrosion resistance and bio-compatibility of NiTi alloys is widely reported [10, 11] broadening their potential applications and further marginalising competing SMAs. This is reflected by the incorporation of NiTi into a wide range of orthopaedic and dental implants. Surface treatments and further alloying [12] have bolstered the applications suitable for this material.

Furthermore the behaviour of near equiatomic alloys of NiTi is highly sensitive to processing and alloy variations giving rise to secondary phases which serve to modify the apparent SME [13-15]. Lastly the associated initiation temperatures tend to be of the order of room temperature allowing countless potential engineering applications.

These properties have served to generate significant interest in harnessing the SME of NiTi alloys to micro-electromechanical applications [5-7]. For the purposes of this introduction, it is important to further explore the SME/SE characteristics which are specific to NiTi alloys.

The effect of alloying, mechanical processing and thermal treatments have been widely examined for various NiTi alloys [16-18]. These require a more detailed understanding of the mechanisms of the phase changes which are unique to these alloys.

NiTi alloys crystallise on cooling below M_F to form a monoclinic B19' structure and follow the generic SMA model, discussed earlier, through heating to form a totally austenitic phase having a cubic B2 structure [19].

An intermediate phase is also commonly observed in equiatomic alloys that have not been fully annealed [15, 20], but is often deliberately suppressed [21]. The so called R-phase (Figure 4), forms through nucleation and growth upon cooling from B2→B19'. Therefore the more precise phase history for some NiTi alloys, including the intermediate phase, should be B2→R-Phase→B19' upon cooling [22, 23]

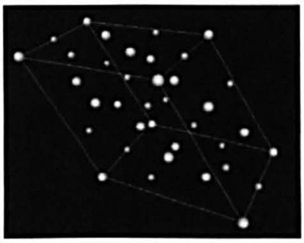

Figure 4 The intermediate trigonal phase (the R-Phase) [3].

The atomic restructuring that occurs during B2→B19'[19, 23] and also B2→R-phase upon cooling [22] has been clearly defined. From the point of view of the application and limits of these alloys, the nature of the stress induced formation of martensite through twinning both below M_F and above A_F is most interesting.

When placed under stress below M_F temperatures, the fully martensitic microstructure of these alloys compensates by twinning. The applied load causes individual martensite crystals to split preferentially along a plane which results in the formation of two identical crystals which are symmetrical about the twin boundary (midrib plane) which separates them. There are 24 habit planes associated with this process, which comes about from the number of planes over which symmetry can exist in the monoclinic phase. This crystallography gives rise to the widely observed 'fanning' type structure, which is in contrast to the solitary habit plane in the cubic austenitic phase.

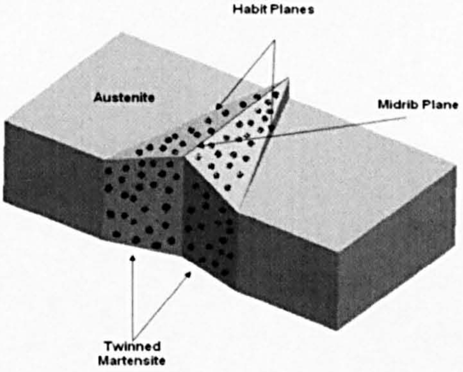

Figure 5 Formation of twinned martensite in NiTi Alloys.

This difference explains the distinct microstructures observed in the martensitic and austenitic phases and their various combinations.

Processing and Training of NiTi Alloys

NiTi alloys are often processed through conventional casting and machining routes. Their sensitivity to oxygen contamination is widely reported [24]. This issue is often ameliorated during casting with a double vacuum process, which entails induction melting the feedstock to prevent gaseous contamination. The alloy is also heat treated in this manner in preparation for the reductive machining processes which will determine the net shape of the component. They are limited in terms of smallest resolvable features by typical micromachining tolerance from processes such as computer numeric control (CNC) or computer aided manufacture (CAM).

However, forming the required component shape in NiTi and for that matter any SME material is only an initial step. To display an appreciable and mechanical response to change in temperature, the final component must undergo a training regime.

For the 'one-way' shape memory effect, the specimen must be cooled below the martensite finish temperature, M_f, at which point it is deformed. It is then heated above the austenite finish temperature A_f and permitted to adopt the form associated with this microstructure.

Two-way training can be achieved by two generic methods [9]. Shape memory effect (SME) training involves cooling the component below its martensitic formation temperature at which point it is deformed. Heating to above the final austenitic formation temperature allowing the component to deform is then undertaken. This process is repeated several times until the two-way SME is observed. The trained component will assume its deformed shape below the martensitic formation temperature and another upon heating above the austenitic formation temperature. The second method employs stress-induced martensite (SIM) training which is a variant of SME training. Initial deformation of the component is undertaken at a temperature in between the martensitic start and martensitic finish temperatures. Upon heating above the austenitic finish temperature the component returns to its original shape. This process is repeated several times until the two-way shape memory effect is observed.

The Piezoelectric Effect

Amongst the plethora of functional properties exhibited by materials perhaps the most useful for sensors and actuators is the piezoelectric effect.

Unlike the shape memory effect which is only observed in manmade materials, piezoelectricity is also observed in some naturally occurring materials. The closely related pyroelectric effect (electro-mechanical response to a change in temperature) was first observed somewhere in the annals of antiquity and as such it is impossible to attribute.

Historical documents indicate that tourmaline crystals (Ceylon magnets) were being imported into Europe from India and Sri Lanka as early as 1703 [25]. Upon heating some crystals, a charge displacement occurs within the unit cell resulting in an apparent potential difference between opposing faces. This may have been first discovered when ash was electrostatically attracted to hot crystalline materials in a fire. Of course these materials were not rigorously examined until much later when they fell under the scrutiny of Jacques and Pierre Curie in 1880. Their interest, combined with developing analytical approaches to crystallography, heralded the first correct explanations of the peculiar properties displayed by these materials.

It was proposed by Lord Kelvin in 1877 that the converse piezoelectric effect is also possible i.e. thermal energy being created as a result of an applied electric field, the electrocaloric effect [26].

The discovery of the potential difference produced as crystalline structures experience strain was paramount to the initial understanding of piezoelectricity. This can be thought of as 'the electric polarization produced by mechanical strain in crystals belonging to certain crystal classes' [25].

It is most convenient in the first instance to consider these properties in terms of the crystallographic structures a material must exhibit to be piezoelectric. Of the 32 crystal classes, only 21 share the property of non-centrosymmetricity (lacking a centre of symmetry) and twenty of these can be considered piezoelectric. Ten of these classes contain dipoles (spontaneously polarized classes) in their unit cell, without the need for poling (the process of inducing a permanent dipole) and are thus said to be polar materials. As a consequence they are also piezoelectrics. If these dipoles can be reversed upon exposing them to an opposing electric field then the material is said to be a ferroelectric.

In polycrystalline piezoelectric materials, poling is required to exploit them. Failure to do this results in zero piezoelectricity because the random orientation of the dipoles means that they serve to cancel each other out.

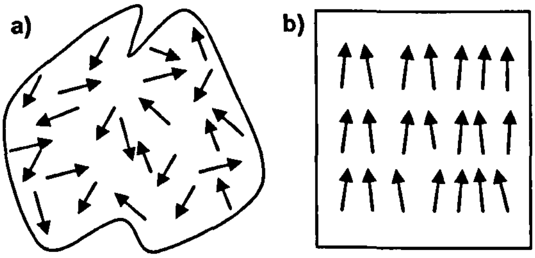

Figure 6 Orientation of dipoles in a) an unpoled material and b) a poled material.

Upon poling, the dipoles align in Weiss domains and a degree of order is achieved in alignment with the electric field. The degree of poling and the duration for which the Weiss domains remain is largely dependent upon the size of the poling field and the poling temperatures. Raising the poling temperature affords the dipoles greater freedom allowing a domain change. This also means that once poling has occurred further heating without an applied field, causes the Weiss domains to breakdown due to randomisation of the dipoles. The temperature above which random orientation is completely returned is termed the Curie temperature (T_c).

Inducing a strain within a unit cell of a poled material, changes the equilibrium separation between the dipoles. A charge displacement is therefore created and a voltage observed.

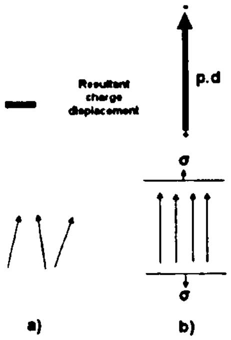

Figure 7 The effect of straining dipoles a) unstrained and b) strained.

A polycrystalline piezoelectric will be isotropic in terms of its electrical properties in the unpoled state. However, poling these materials causes anisotropy, and their electrical properties will vary according to the orientation in which they are measured.

From first principals, the piezoelectric effect can be defined by quantifying the mechanical stimulus which causes an electrical response. The strain (ε) induced in an anisotropic material with Young's modulus (E) due to a given (σ) stress (within its elastic limit) is given by:

$$\varepsilon = \frac{1}{E}\sigma \tag{1.4}$$

This can be written in terms of compliance, *c*:

$$\varepsilon = c\sigma \tag{1.5}$$

When the piezoelectric effect is observed, a charge displacement is initiated. This is reversible and unloading a piezoelectric material causes a reduction in the electrical field measured. This can be expressed as:

$$D = d\sigma \tag{1.6}$$

Where D represents the electric charge displacement (C/m^2) resulting from a stress σ. A new, material parameter, *d* is defined, the so called piezoelectric strain coefficient (C/N).

For a piezoelectric material, the application of an electric field (E)(V/m) causes a charge displacement within the unit cell resulting in a macroscopic deformation of the material (the converse piezoelectric effect) In a material of electrical permittivity ($\in$) (F/m), assuming dipole saturation is not achieved, this is given by:

$$D = \in E \qquad (1.7)$$

It is well understood that the macroscopic strain observed during the converse piezoelectric effect is the result of a finite contribution from each dipole displaced. The relationship of strain to electric field shares the same constant of proportionality as that in Equation 1.6. Therefore:

$$\varepsilon = dE \qquad (1.8)$$

If the strain induced in a piezoelectric material is due the contributions of both an applied mechanical load and electric field then equations 1.5 and 1.8 can be coupled to give:

$$\varepsilon = c\sigma + dE \qquad (1.9)$$

Likewise if the charge displacement observed in a piezoelectric material is thought to be due to the combined interaction of an applied electric field and mechanical load then equations 1.6 and 1.7 can be coupled to give:

$$D = d\sigma + \in E \qquad (1.10)$$

'Real' piezoelectric materials are not described well by an isotropic model. Charge displacement can occur in three resolvable directions, as can the application of an electric field. A simplified situation is examined to demonstrate the piezoelectric response of a cube subjected to such loads.

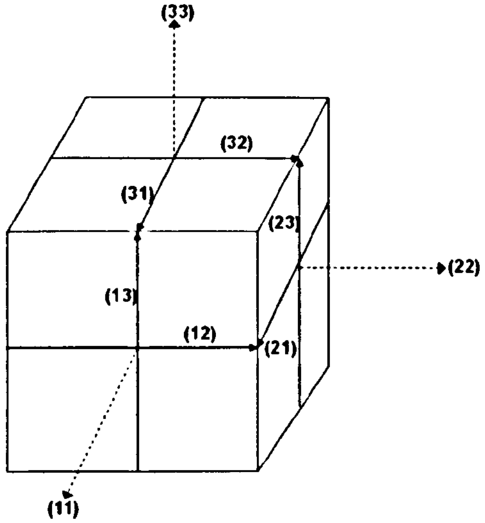

Figure 8 The principal vectors in relation to an example piezoelectric cube. (N.B vectors of shear are indicated with*)

This model allows for anisotropic behaviour to be considered. If electric field and dipole displacements are now considered as vectors

$$\underline{E} = \begin{Bmatrix} E_1 \\ E_2 \\ E_3 \end{Bmatrix} \tag{1.11}$$

$$\underline{D} = \begin{Bmatrix} D_1 \\ D_2 \\ D_3 \end{Bmatrix}. \tag{1.12}$$

They can thus be combined to fulfil Equation 1.7:

$$\begin{aligned} D_1 &= \epsilon_{11}\, E_1 + \epsilon_{12}\, E_2 + \epsilon_{13}\, E_3 \\ D_2 &= \epsilon_{21}\, E_1 + \epsilon_{22}\, E_2 + \epsilon_{23}\, E_3 \\ D_3 &= \epsilon_{31}\, E_1 + \epsilon_{32}\, E_2 + \epsilon_{33}\, E_3 \end{aligned} \tag{1.13}$$

In the interests of concise notation this can be written in the following manner

$$D_a = \in_{ab} E_b \tag{1.11}$$

in which a and b define the size of the array. Equation 1.5 can also be manipulated for the anisotropic case. If mechanical compliance is the product of two 3 x 3 matrices corresponding to stress and strain then a 9 x 9 matrix will result giving 81 compliance terms. Applying Voigt symmetry rules to the stress/strain matrices results in a 6x6 compliance matrix:

$$\begin{Bmatrix} \varepsilon_1 \\ \varepsilon_2 \\ \varepsilon_3 \\ \varepsilon_4 \\ \varepsilon_5 \\ \varepsilon_6 \end{Bmatrix} = \begin{bmatrix} c_{11} & c_{12} & c_{13} & c_{14} & c_{15} & c_{16} \\ c_{21} & c_{22} & c_{23} & c_{24} & c_{25} & c_{26} \\ c_{31} & c_{32} & c_{33} & c_{34} & c_{35} & c_{36} \\ c_{41} & c_{42} & c_{43} & c_{44} & c_{45} & c_{46} \\ c_{51} & c_{52} & c_{53} & c_{54} & c_{55} & c_{56} \\ c_{61} & c_{62} & c_{63} & c_{64} & c_{65} & c_{66} \end{bmatrix} \begin{Bmatrix} \sigma_1 \\ \sigma_2 \\ \sigma_3 \\ \sigma_4 \\ \sigma_5 \\ \sigma_6 \end{Bmatrix} \tag{1.12}$$

Similarly this can be reduced to the following terminology in which subscripts refer to the dimensions of each matrix:

$$\varepsilon_{pq} = c_{pqrs} \sigma_{rs} \tag{1.13}$$

This methodology can be repeated for equations 1.6 and 1.8 to give:

$$\varepsilon_{pq} = d_{bqn} E_b \tag{1.14}$$

and

$$D_a = d_{ars} \sigma_{rs} \tag{1.15}$$

The final stage in this derivation is to return these constitutive equations to their coupled format as in Equations 1.9 and 1.10:

$$\varepsilon_{pq} = c_{pqrs}\sigma_{rs} + d_{ars}E_b \qquad (1.16)$$

$$D_a = d_{ars}\sigma_{rs} + \in_{ab} E_b \qquad (1.17)$$

This treatment allows repeatable, accurate predictions to be made about the electromechanical performance of piezoelectric materials and reliable inclusion into engineering systems [27].

Piezoelectric materials have found a diverse range of micro-scale applications including peristaltic micro-pumps [28], thin film type sensors [29] and micro-actuators [30, 31] amongst others. The manufacture of conventionally scaled components made from these materials has become common place and is well understood. By contrast, the incorporation of these materials into MEMS type systems is an area of continuing research. Processing piezoelectric materials on the micron level, to produce thin films or true 3D geometries presents an entirely different level of complexity [32]. Manufacturing processes to be tailored to the requirements of the feedstock material (either ceramic or polymeric) and the specific properties required of the final component shape. There is often a significant trade-off between desired shape and desired performance. That is to say, producing the desired shape maybe possible, but the resultant loss of piezoelectric response renders the design pointless.

After manufacture, piezoelectric specimens must be poled to exhibit the piezoelectric effect. In practice, this involves heating the material in the presence of an electric field of the order of kV's/mm. This is an important consideration and has been the subject of considerable research to develop polymers which spontaneously exhibit the PE after manufacture [33]. Some laser-based processing techniques have also been developed with strategies for consolidation of piezoelectric ceramics [34, 35].

Barium Titanate

The perovskite structured barium titanate ($BaTiO_3$) has been extensively studied and been termed 'the model ferroelectric material' [36]. With a low Curie temperature of 123°C; zero lead (Pb) content; large piezo- and pyroelectric-coefficients; and low cost of manufacture $BaTiO_3$ has been the subject of considerable research interest [37].

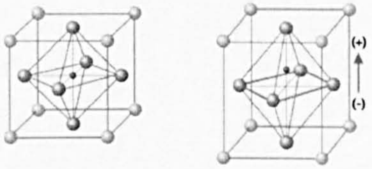

Figure 9 Strain and centrosymmetricity in a $BaTiO_3$ unit cell [38]

Figure 9 shows the charge displacement resulting from strain endured by orthorhombic $BaTiO_3$.

The conventional approach to $BaTiO_3$ synthesis is a chemo-mechanical process. Firstly $BaCO_3$ is ball milled with TiO_2. The blend is calcined at an elevated temperature at which $BaTiO_3$ forms through a slow diffusion process [39]. This reaction is well understood and results in $BaTiO_3$ with acceptable properties. However, grain sizes produced in this way are often large and hence difficult to consolidate through sintering. This is important since the ferroelectric properties of this material have been shown to relate strongly to grain size [40, 41].

The electrical properties of $BaTiO_3$ are not only sensitive to chemical composition but also material processing which dictates its microstructure [42]. There has been a drive to optimise processing techniques to improve the electrical properties. This optimisation has been achieved through a variety of laser based and conventional sintering techniques [40, 43], thin film methodologies [44-46], chemical vapour deposition (CVD) [47, 48] and sol-gel/polymerisation techniques [39, 49, 50]. Much of this research is driven by the industrial demand for dielectrics for Multilayer Ceramic Capacitors (MLCC). These normally draw upon perovskite structured materials like $BaTiO_3$ for their high dielectric constant. This is of special importance with ever reducing component sizes.

$BaTiO_3$ can assume five different crystal structures namely, hexagonal, cubic, tetragonal, orthorhombic, and rhombohedral. The hexagonal and cubic structures are paraelectric while the tetragonal, orthorhombic and the rhombohedral forms are ferroelectric.

Perovskite, $BaTiO_3$ is cubic from 123°C to 1460°C with Ba^{2+} ions at the cube corners, O^{2-} ions at the face centres, and a Ti^{4+} ion at the body centres. Below the Curie temperature of about 123°C, the cubic structure deforms slightly and the positive barium and titanium ions move relative to the negative oxygen ions along the [001] direction. This results in a tetragonal structure which spontaneously polarizes along the same direction. With further cooling below about 5°C the structure changes to orthorhombic which now polarizes along the [110] direction [51].

The ferroelectric-paraelectric transition is of utmost importance which occurs at the Curie temperature. At this temperature, paraelectric cubic $BaTiO_3$ transforms into the ferroelectric tetragonal structure by elongating along an edge, thus removing any domains created by poling

Macroscopic scale $BaTiO_3$ components for piezoelectric/pyroelectric applications are usually produced by a compaction process to consolidate grains into the desired geometry. This limits the complexity of parts that can be manufactured. The 'green', compacted parts are then placed in a furnace and sintered at approximately 1000°C for up to 5 hours [42], resulting in components with some degree of mechanical resilience. The final step in the process is the poling procedure.

The degree of polarisation in a material is quantified by measuring the charge observed at its surfaces due to the application of a given pressure. This value (C/N) describes the piezoelectric response in the direction in which it will be most apparent i.e. parallel to the direction of the poling field. The d_{33} of $BaTiO_3$ after poling is directly proportional to the applied voltage until saturation is observed at which point additional electrical tension across the specimen will cause no further polarisation [52].

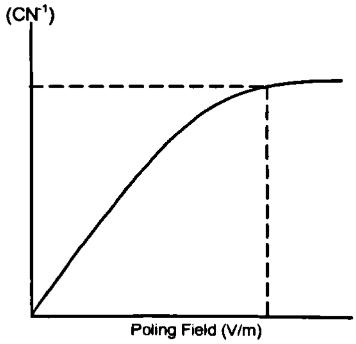

Figure 10 Linear relationship of piezoelectric response with poling voltage to saturation.

The relatively large fields required to maximise poling presents a practical problem. The electric field strength e (V/m) of a uniform field between two electrodes is

$$e = \frac{V}{x} \tag{1.18}$$

V is the applied voltage and x is the electrode spacing (m). From Figure 10 it can be seen that poling saturation for $BaTiO_3$, as for any piezoelectric material, is observed. Poling fields commonly employed are usually of the order of around 80MV/m. This dictates that maximum polarization of $BaTiO_3$ cannot take place in air which breaks down in fields of around 10MV/m. This problem is usually overcome by poling in a medium with a much lower dielectric permittivity such as oil. The voltage required is also dictated by the thickness of the sample. Therefore thin films will require smaller applied voltages.

After poling some degradation of piezoelectric properties is frequently reported [53]. This comes about as individual dipoles and whole domains adopt a more random orientation. The extent and time scale of this degradation are material, temperature and excitation cycle type dependent [54].

$BaTiO_3$ has found many common place applications such as, non intrusive sensors for fluids analysis [55]. Its ferroelectric properties have been widely exploited for micro-electronics applications such as ultrasonic transducers [56] and it has been incorporated in several piezoelectric composites which may have more favourable mechanical properties compared to single crystal or sintered $BaTiO_3$ [57, 58]

PVDF-TrFE

The discovery of the piezoelectric [59] and ferroelectric [60] properties of polyvinylidene fluoride (PVDF) and in its copolymer with trifluoroethylene (TrFE), has generated much research interest. The piezoelectric effect is no longer limited to ceramic materials but now polymers have been shown to display the effect as well.

After poling, Weiss domains are observed in crystallites of the polar β-phase [61] within PVDF. Like other piezoelectric materials, the polymer exhibits no piezoelectricity, until poled as the cumulative effect of straining unaligned dipoles nullifies any charge separation.

Stretching PVDF has been shown to transform the non-polar α-phase into the polar β phase. Increasing the β phase percentage increases the volume fraction within the polymer that can be polarized, yielding an overall higher piezoelectric coefficient. Variations of this poling regime have been extensively investigated [29, 62, 63]. The addition of TrFE to form the copolymer causes the polymer to crystallise preferentially in the polar β phase in a similar manner to the PVDF homopolymer [64]. The highest polarisation in such copolymers has been shown at the ratio PVDF 75 : TrFE 25 [65-67] and typical piezoelectric coefficient values at this composition have been shown to be 20pC/N [68].

PVDF-TrFE copolymers have also been noted for their ferroelectric 'hardness'. That is to say the degree of remnant polarisation after exposure to the poling electric field especially at room temperature [69].This feature suggests several possible applications for these materials if combined with ceramic ferroelectrics and piezoelectrics in composites.

Piezoelectric polymers have several distinct applications, in comparison to competing ceramics. The ease of forming thin or thick films and large scale shapes without the need for high energy consolidation techniques (sintering) makes them an attractive choice. Furthermore the lamination of the copolymer may yield a more tolerable artefact in comparison to particulate consolidated ceramics for biocompatibility applications [70].

PVDF-based polymers have been processed using thin film techniques [71] which has permitted combination with carbon nanotube systems (filling and embedding) [72, 73]. Several emerging markets are drawing upon these technologies such as 'active' clothing [74] (power generation from the distortion of fabrics) and 'active' structures [75]. The latter relates to piezoelectric whiskers which have been incorporated into structural bodies such as wind turbine blades [76].

Piezoelectric Composite Materials

More recently interest has developed in combining different piezoelectric materials and combining piezo and dielectric materials to form composites or 'piezoelectric hybrids' [77].

When piezoelectric materials are combined with dielectrics to form composites, they may display advantageous mechanical properties but this is coupled with a reduction of the piezoelectric modulus. This presents an interesting opportunity cost for the materials designer who must evaluate the mechanical benefits against a loss in piezoelectric properties (or any other electrical properties for that matter).

The mechanical and electrical properties of composite materials are more complicated than their single phase constituents. As discussed previously, the charge produced by mechanical deformation of a piezoelectric material is directly proportional to the strain experienced by each unit cell. However, when materials are combined to form a particulate-matrix composite, then any applied load will not be uniformly distributed between phases. Due to non-homogeneous compliances in the 'matrix' and 'filler', distinct strain values occur. Embedding the piezoelectric ceramics $BaTiO_3$ or lead zirconium titanate (PZT) in polymer matrices has been investigated extensively [78-80]. Using polymer matrices such as epoxies and acrylics, complex shapes can be formed with the ease of material processing of a polymer. However, for piezoelectric composites to perform well, the interaction between the two materials within the composite must be considered.

Figure 11 illustrates a hypothetical ceramic-polymer composite;

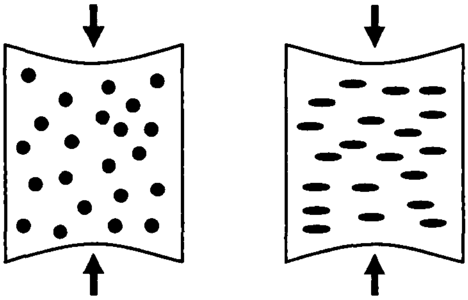

Figure 11 Strain transfer from matrix to filler in a polymer-ceramic composites. a) depicts no strain transfer from matrix to filler b) depicts a high degree of strain transfer from matrix to filler.

If the ceramic filler is a hard brittle material compared to the elastic polymer matrix, then the strain transferred to the ceramic will be much less than the strain induced in the bulk material. If a stress σ_A is experienced by such a composite then it will be distributed in the following way [81];

$$f\bar{\sigma}_p + (1-f)\bar{\sigma}_c = \sigma_A \tag{1.19}$$

Where the volume fraction of polymer is given by f while the mean stress it experiences is given by $\bar{\sigma}_p$ and the mean stress experienced by the ceramic filler, $\bar{\sigma}_c$. To maximise the bulk piezoelectric response of the material, the difference in elastic moduli should be minimised to ensure that the maximum strain is born by the piezoelectric filler.

Ideally the piezoelectric material content within the composite should be as high as possible to maximise the piezoelectric coefficient. This also presents difficulties because as f becomes small, the level of cohesive binding decreases leading to poor mechanical integrity and process-ability. Piezoelectric moduli for PZT/epoxy and $BaTiO_3$/epoxy composites of 25pC/N [82] and 230pC/N [83] respectively have been reported which is, as expected, significantly lower than for the pure piezoelectric materials [84].

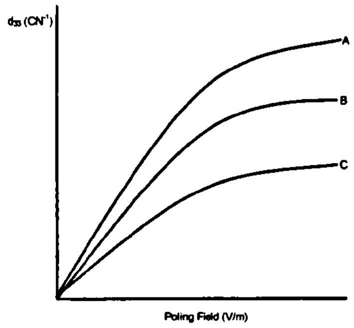

Figure 12 Variation of d_{33} with piezoelectric volume fraction ranging from 'A'the highest volume fraction to 'C' the lowest.

The development of piezoelectric polymers has resulted in superior piezoelectric properties to the piezo/dielectric composites discussed above. The piezoelectric properties of PVDF and PVDF-TrFE composites have been investigated to some extent [64, 85, 86] and significantly higher piezoelectric properties demonstrated. Poled composites of $BaTiO_3$/PVDF have been reported with d_{33} values of 13.7μC/N at relatively low poling fields [87]

Layer Based Manufacturing Techniques

Layer based manufacturing techniques (LBMT) are often described by alternative names including; solid freeform fabrication (SFF), 2½D manufacturing, rapid prototyping (RP) and rapid manufacturing (RM). The inconsistency in terminology used is most likely due to the immaturity of the industry and fragmentation of the market.

'Layer based manufacturing' will be used as the convention in this thesis, as it is more accurate than the other terms listed above. The term 'freeform' suggests that component geometries are unrestricted by the method in which they are formed. This is untrue and is only partially the case for methodologies as laser chemical vapour deposition (LCVD) in which laser radiation is used to solidify a chemical vapour. In this scenario a datum point of initiation is required. Therefore, the term SFF can be largely disregarded. The terms RP and RM have also been disregarded because LBMT may be employed to produce both prototypes and functional parts however these are often only 'rapid' when compared to the slowest of the competing conventional manufacturing processes.

LBMT are largely born out of processes originally designed to fulfil the requirements of the prototype engineer and model builder. Developments in layer based manufacturing processes have opened new applications.

The flexibility of these processes is their strongest advantage over conventional manufacturing techniques. Ideally no-hard tooling is required for LBMT and component finishes may be close to the final specification. This is the ultimate aim and often the current claim of system suppliers. However, this does not make the available processes economical for the mass production of most products due to the relatively high system, feedstock, labour and running costs.

Commercial LBMT are found in several 'flavours' which normally involve various combinations of feedstock material (polymer, metal, ceramic and hybrids of above), fusing process (laser, masked light, adhesive) and recoating mechanism (fluid levelling, mechanical wiper, sheet delivery or masking). These are complimented by emerging techniques which employ continuous material delivery such as spiral growth manufacture (SGM) [88] which result in parts with one apparent layer.

All of these processes have a common generic process flow which may be represented as follows;

Figure 13 LBMT generalised process flow.

A model of the desired component is generated within a computer design package. This represents the first model within the process. Most commercially available parametric design software packages will allow the generation of geometries and tolerances which are in excess of that which can be realised through LBMT.

The CAD is manipulated to allow 'slicing' in which each layer is defined. This usually involves the approximation of part surfaces as triangles. This approximation is best demonstrated if a perfect sphere is considered. Of course the surface of a true sphere is made up of an infinite number of points which cannot truly be recreated, even if atom by atom deposition was possible with LBMT. Therefore the surface is modelled as a series of nested triangles whose outer sides form a polygon. The greater the number of triangles used in the approximation, the greater the fidelity to the designer's model.

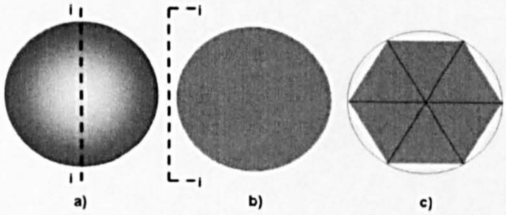

Figure 14 Triangulated approximations to curves. b) shows a slice from the sphere depicted in a). This is then triangulated to form the polygon c).

After triangulation, the first divergence from the original design is introduced. It is impossible to triangulate with an infinite number of triangles as would be required to maintain perfect fidelity, due to computational limits. However, unless the manufacturing process is undertaken in a coarse manner then perturbations like those observed in Figure 14 will not be observed in the finished geometry. In most LBMT the tolerances of the finished part are not limited by surface triangulation but by the smallest physical element producible in the build stage, which is unique to each build system.

The final step in 'build' preparation is to slice the geometry. This involves dividing the model into discrete planes perpendicular to the build direction. Ideally these slices would be of an infinitesimal thickness to give a perfect representation of the design. This is impossible in practice and the tolerances achieved within manufacture are limited by the smallest mechanical increment which can be made for each technique being used.

The slicing stage also causes a further deviation from the original design. Each slice is indexed and a corresponding two colour, 2D image is created separating the region which requires processing from that which does not.

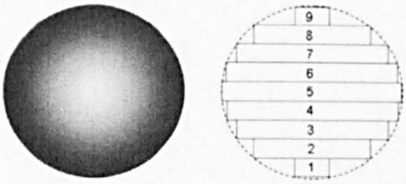

a) **b)**

Figure 15 Slicing of a sphere into discrete layers. Thinner layers reduce the 'staircase' effect.

The processed data is transferred to the tool which produces the required phase change layer by layer and thus manufactures solid geometry.

These process stages are common to most current, commercially available LBMTs. The precise process varies from manufacturer to manufacturer and will often incorporate proprietary software in order to protect intellectual property and customer base.

Two LBMT techniques have been used extensively in this thesis and are discussed at a greater length here.

Selective Laser Melting/Sintering-Methodology

Selective laser meting (SLM) or at least its parent technology selective laser sintering (SLS) first emerged in the mid 1980's in a patent secured by Carl Decker of B.F Goodrich [89].

These techniques share common functionality, in that they use a laser source to fully melt a feedstock material (SLM) or sintering (SLS). Indeed some commercial machines can perform both operations [90].

A powdered feedstock is used which is deposited on to the build area in the form of a thin layer. The so-called 'recoating' mechanism deposits a smooth layer of powder, completely covering a substrate plate onto which the component will be built. The substrate plate is selected to ensure that the following melted/sintered build layers adhere well to it. The laser is rastered over the surface of the powder layer causing the powder particles to sinter in the case of SLS or form a complete melt pool in the case of SLM. The rastering regime is specifically controlled to manage the laser-material interaction.

The morphology and the material itself, significantly effects how the feedstock material interacts with the laser radiation. Powder sizes are usually selected between 50-100μm, however, Becker et al [91] report using powder sizes of the order of 10μm. The key factors affecting powder performance include flow-ability, reflectivity/absorbance and packing density. The powdered feedstock must flow well to ensure an even layer direct from the recoating mechanism and hence reproducible build layers.

The feedstock must also absorb sufficient radiation at the appropriate wave length to partially or completely melt; however the energy threshold required for evaporation must not be exceeded. In some cases pre-treatment of powder has been reported to reduce reflectivity [89]. The packing density of a powder is governed by the morphology of the powder particles and needs to be maximised for both SLS and SLM processes. The proximity of neighbouring particles must be minimised so that melt pool formation or contact area will be promoted. This is normally achieved in metals by using particles with a high degree of spherocity which are normally produced by gas atomisation. Multi modal powder size distributions will result in more densely packed layers but may not necessarily flow easily.

The manner in which the laser is rastered over the powder bed is achieved by the control of a mirror. The laser spot dwells at a given location for a prescribed time, governing the amount of energy delivered to the material surface

If a material is exposed to a laser beam of circular cross section with radius r (mm) and power P (W), then the power density is given by P_ρ (W.m^{-2}).

$$P_\rho = \frac{P}{\pi r^2} \tag{1.18}$$

If the laser is now considered to be traversing across a surface with a velocity, v (m.s^{-1}) then an energy density E_ρ at the spot centre can be formulated as;

$$E_\rho = \frac{P}{\pi r^2} \cdot \frac{2r}{v} \tag{1.19}$$

This equation is fundamental when defining a suitable parameter set for the SLS/SLM of a particular material. An appropriate spot size, laser speed and laser power can be calculated to induce the required degree of melting in a given material.

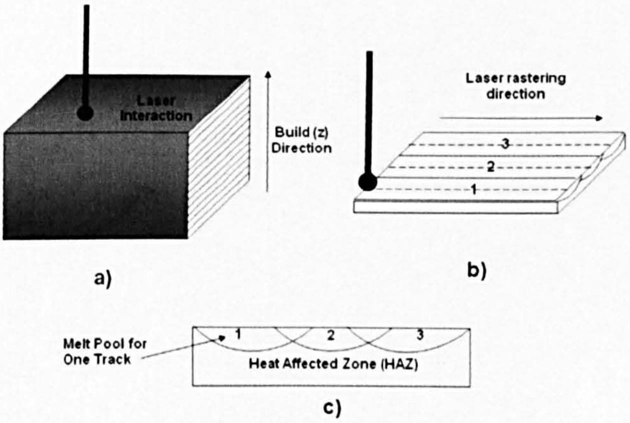

Figure 16 a) A solid block produced by SLS/SLM made of build layers b) Three tracks side by side, processing one layer Dashed lines show maximum track overlap c) Layer in cross section depicting typical melt pool profile and heat affected zone (HAZ).

The tracks of the laser beam are often overlapped which can cause re-melting in some already solidified regions within a part. This is demonstrated in Figure 16.

The degree of overlap is known as 'hatch spacing'. The hatch spacing chosen has a significant effect upon the quality of finished component, especially at the 'skin' or outer surface of the components. This effect has been the focus of considerable research due to the relatively poor surface finish of SLM/SLS type parts in comparison to those conventionally machined.

Additive manufacture and SLM are still relatively new technologies and consequently, are presently still finding new applications [92].

Properties of SLM/SLS Components

The properties of metal parts formed by SLM are largely determined by the feedstock and process parameter set. These will in turn be dictated by the application.

Parts of near 100% bulk density have been reported in a wide range of alloys including aluminium [93], stainless steel [94] and copper. [95]. The parts have been subjected to mechanical testing and found to have properties comparable and in some instances superior to other reductive manufacturing processes which have not been heat treated. Other work [96] has investigated two-stage processing in which the SLM part is subjected to hot isostatic pressing (HIP). 'Hipping' serves to consolidate SLM materials and reduce porosity.

The design freedoms granted by using SLM also allow the manufacture of unique geometries such as porous or mesh-like structures and nested features [97, 98]. Components have also been produced which incorporate functionally graded properties [99]. These are achieved by varying the incident energy over different regions of a component. This process mimics selective heat treatment, but within a single manufacturing process. Careful control of skin rastering regimes can also result in an effective casing of a component whose depth can be specifically controlled.

SLM mesh structures have been exploited in aerospace applications [100], high performance automotive and medical applications [101, 102]. Incorporating meshes is largely undertaken to produce light weight components. These structures have also been incorporated into components for their thermal properties [103].

Ceramic materials have also been processed by SLS with varying degrees of success using dry layer deposition [104] and slurry layer deposition [105]. These materials usually require modifications to the build chamber environment. For example, they may need a partial pressure of a suitable gas to ensure that species present do not disassociate themselves upon heating. This presents a significant fire hazard as most commercially available SLS/SLM systems operate under low oxygen conditions (<1%).

This approach is predominantly undertaken to limit the possibility of ignition however several commonly used SLM feed stocks, such as titanium, are known to react violently upon oxidation. This issue is compounded by the fact that the feedstock material will be in a fine powder form with a large surface area to volume ratio.

SLM has also been used to build two-phase metallic structures and materials made from dissimilar ones to that of the build substrate. This has generated new lines of investigation with regards to material selection, material treatments, material delivery and substrate preparation.

Digital Light Projection Methodology

The emergence of Texas Instrument's digital mirror devices (DMDs) represented a significant step forward in commercially available MEMs technology, enabling the development of common appliances such as the digital projector. This technology has become more common place and hence cheaper to the product developer and end user.

The increased affordability of the 'DMD chassis' (consisting of DMD chip, lens mounting, associated electronics and cooling unit) has allowed small concerns to develop new applications for this technology. One such application exploits the 'dynamic masking' capability of these systems to selectively expose photo sensitive resins causing them to polymerise layer by layer.

Lithography, from the Greek 'to write in stone with light', exploits the interaction of light with a material to remove or 'cure' material in selected areas. These techniques require a specific mask per given pattern layer. This has a significant cost in most cases, unlike the DMD masking technique which is simply reprogrammed for each layer. Conventional lithography can therefore be thought of as a two dimensional technique.

Although the operator has some control over the 'thickness' of the layer this is thought of as a 2D process. Some topography including undercuts and graduated removal can be achieved by employing etching techniques at a later stage.

The resolution of conventional lithographic techniques is fundamentally limited by the wavelength of the light source selected for the process. This is defined by the Rayleigh criterion;

$$\sin\theta = 1.22\frac{\lambda}{d} \tag{1.20}$$

In which θ refers to the maximum angle that can pass through the objective aperture, λ refers to the wavelength of the incident radiation and d refers to the diameter to which the beam can be focussed. The limiting nature of λ has fuelled research into shorter wavelength systems including X-ray and electron lithography [106].

The DMD masking technique employs a dynamic masking regime to define repeated layers of a controlled geometry layer-by-layer hence the term '$2^1/_2$D processing'. Although the resolvable feature size fundamentally limited by the wavelength of light employed (like 2D lithography) it is far more likely to be limited by the density of the mirrors mounted upon the DMD chip (currently 1920 x 1080). To appreciate this, a more detailed understanding of DMD masking or Digital Light Projection (DLP) operation is described below.

Variations of the DLP theme are commonplace, however most systems consist of the following elements: DMD chassis (plus optics), stepper motor (for z directions translation); a resin container (with transparent floor) and a removable build substrate. A typical layout can be seen in Figure 17;

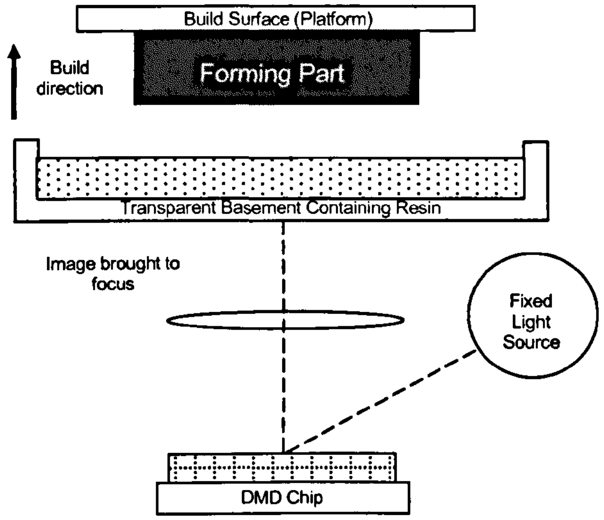

Figure 17 A DLP system after the Envisiontec Perfactory.

The pre-processing of the computer generated model for DLP is identical to the generic RP method discussed earlier, right through to the generation of two colour bitmap images corresponding to each individual build layer. These bitmap images are used to actuate individual mirrors on the DMD causing them to reflect light toward the resin container where polymerisation occurs. Photopolymers contain photo-inhibiters which segregate monomers preventing them from unwanted polymerisation. Upon exposure to light of a specific wavelength, these inhibiters are decomposed and polymerisation can occur. To allow this process to be repeated, a fresh layer of uncured polymer must flow to the transparent floor. This requires that the previously cured layer is raised by a stop corresponding to one build layer thickness. To achieve this, the stepper motor translates by a distance Δz allowing the liquid polymer to seep under the previously cured layer. Repeated exposure causes the new layer to adhere preferentially to the previously cured one. The photo reaction occurs again and the process repeated for each successive build layer.

The resolution of DLP systems, like most LBMTs, is anisotropic. This is because resolution limiting parameters are different in the coordinate axis with reference to each build layer. Components realised in this way can be thought of as consisting of a multitude of voxels (volumetric pixels). These discrete 'building blocks' have their dimensions imposed upon them by the dimensions of each mirror mounted on the DMD (after imaging, as observed at the resin floor) corresponding to the x-y resolution and in the z direction the smallest practical translation of the stepper motor.

The stepper motor limitation is a well recognised engineering problem and several manufacturers report repeatable layer thicknesses of $\approx 15\mu m$ which is comparable to tolerances achieved by CNC platforms. The degree to which light can be focused from each mirror also presents several challenges. For MEMS type applications, the greatest x-y resolution is of course required but focusing must result in a voxel array (matrix of discrete volumetric pixels) which closely resembles the activated mirror array at the DMD chip for maximum fidelity to the design. Therefore, a balance between the x-y dimensions ($x = y$ if the mirrors are square) and the fidelity of the voxel as observed at the build surface must be made.

Focusing an image (in this case from an individual mirror at the DMD chip) to the build surface causes the entire image, which consists of an array of individual focused mirrors; to become smaller but remain mathematically similar. This area is known as the build envelope and so another balance must be struck between optimum resolution and the size of a given build envelope. The size of the build envelope is a prime concern in the development of any LBMT but perhaps more important in a 'fixed time per layer' process such as DLP.

LBMTs fall into two groups using this consideration. The 'fixed time per layer' methodologies take the same time to complete any build layer even if a very small fraction of the build area is used. This is compared to 'variable time per layer' methodologies whose layer build time depends upon the fraction of the build envelope used in a given layer which is the case for SLM. Hence for maximum throughput, optimisation of the build envelope is of prime concern.

Plastic Structures and Composites

Acrylic, epoxy and wax based resins have been processed by the DLP method. Variants of these materials are available with modifications to their viscosity (achieved with fillers and heating elements in the resin bath) to make them more suited to given layer thicknesses.

Polymer-type LBMT formulations are usually protected by IP and limited to proprietary system parameters. The polymers available to users are specifically designed to cure only at the wavelength that a particular system can produce. This is done to ensure the manufacturer maintains exclusive or near exclusive material supply rights.

Consequently fundamental materials research for these resins tends to be within the realm of the polymer chemist who customises the material to suit the most significant demand in the market. These include (in order of profitability); custom prosthetics [107], investment casting blanks[108, 109] and models. The properties of many DLP compatible materials limit their functionality and thus applicability to practical prototypes. However, good tolerances/surface finish, minimal secondary processing, and quick component inter assembly yield some advantages over other LBMTs which are designed to process more robust engineering materials.

The relative immaturity of DLP as a manufacturing technique, even with respect to other LBMTs, means that its full potential has not yet been realised. This is substantiated by the considerable volume of ongoing research. This research can be divided into lines of investigation which ultimately benefit the progression of DLP but are quite distinct with respect to one another.

Micro Electro-mechanical Devices

The drive for smaller electromechanical technologies has never been greater. Fuelled by the huge worldwide markets for consumer electronics which incorporate once thought of 'space age technologies' such as mobile communication devices at affordable prices, the trend is set to continue.

Miniaturisation of commonplace electronic components such as transducers and RF aerials is widespread. However, there are many bespoke engineering components for which this has not taken place. This is due to the cost of prototyping and poor economies of scale. Rapid prototyping techniques have the potential to address this situation to some degree.

Reducing the size of electrical components is of interest because generally it leads to reduced power consumption, greater portability and faster system speeds. Layer based manufacturing techniques have the potential for imitating conventional components, but also exceed the performance of the conventionally manufactured articles.

Decreasing component sizes has also yielded significant research interest in the field of micro-fluidics. Non-linear scaling of fluid properties results in the manifestation of visco-elastic characteristics in capillaries. These properties compounded by significantly enhanced surface area/volume ratios [110] herald great potential for micro-featured reactors.

Layer based system manufacturers have not yet exploited these markets. According to the industry standard review (The Wohler's Report) [111] RP and RM apparatus are largely being utilised for research and manufacture associated with model building, aerospace and biomedical applications. This focus is largely due to the ease of penetrating these markets. However, the rapid development of machine design and feedstock materials makes new bespoke applications possible. These bespoke applications have included, but are by no means limited to ion traps [112], micro chemical reactors [113] and unmanned air vehicle (UAV) components[114]. The escalation in value added post-design and through manufacture makes the processing of such components economically viable.

Mass Spectroscopy

Mass spectroscopy is an analytical technique used to identify the atomic or molecular species of a sample. This is achieved by ionising a sample and evaluating their mass-to-charge ratio. This measurement can be done by collimating the ions with an Einzel (electrostatic) lens array and then using an electric field filtering technique which allows only ions of a characteristic mass-to-charge ratio to pass. The ions that migrate through the filter then impact upon a charge collection device and a current recorded.

Since the 1950s [115] mass spectrometry has emerged as a useful tool for fixed locations analysis. More recently an interest has been registered in more portable devices [116]. The portability of such devices is limited by three principal factors. Firstly the impractically short mean free path of ions at atmospheric pressure means that the process must take place in a vacuum. Secondly, the process of ion generation usually requires an incandescent source. This requires significant power, and finally the bulky size of the spectrometer makes portability impractical.

The design of quadrupole mass spectrometers has varied little since the 1970's. They frequently consist of thoriated filaments for incandescent ion sources, four circular profile cylinders and a Faraday cup detector. They often include a photomultiplier device.

The mass filter is a crucial element of the system. Optimisation of the field produced by the quadrupoles is essential to yield a mass spectrum with a high resolution. The profile of the electric field generated within the filter is largely determined by the profile of the electrodes. These are commonly circular in cross section and have a uniform profile and are so termed 'rods'.

It is widely accepted that for optimum field conditions, proposed by theory [117], simulation [118] and verified by experiment [119] that the superior profile is parabolic in cross section. Further theoretical studies suggest that advantages might accrue through the incorporation of none uniform geometries e.g. helical [115].

These parabolic features present fabrication difficulties if traditional manufacturing approaches are employed. Therefore, incorporation of layer based manufacturing processes which could achieve required tolerances would find significant application here.

LBMT have been used to manufacture some components for similar systems; most notable was the SLA ion trap as produced by Cooks et al [112], but by no means explores the design freedoms afforded by high resolution LBMTs.

Development of mass spectrometers has advanced rapidly in the last couple of years with a main focus on building fully integrated devices that can be made portable while maintaining good performance. To achieve this, miniaturization of mass spectrometer components has been pursued, especially in the case of mass analysers.

Commercial targets include lowering manufacturing costs because the implementation technologies that are being used offer mass production not only for discrete components, but also for complete devices.

Secondly, operation at higher pressures can be achieved due to the shorter length of ion path through the filter section. Consequently this lessens demand upon the vacuum required and therefore cheaper vacuum pumps may be used.

The mass spectrometer may consequently have lower power consumption and the possibility of operating with a smaller battery since lower electrode voltages are needed to generate the required electric fields.

These advantages may lead to in-field measurements such as instant medical diagnosis, water and environmental analysis and detection of oil, natural gas, and explosives.

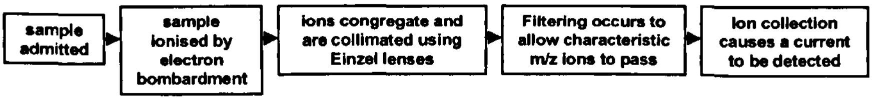

Figure 18 The typical process flow for a quadrupole mass spectrometer.

Miniaturization of mass spectrometers has been realised previously by using MEMS technology, which is mainly based on semiconductor micro-engineering with metal parts. Since complex electrode shapes, such as hyperbolae, cannot be machined at micro-scale, simpler geometries like cylindrical and planar ones are used to approximate the ideal hyperbolic field. One of the first miniature analyzers constructed using MEMS was a quadrupole mass filter (QMF) with cylindrical electrodes [120]. Other successful miniature mass analyzers include a time-of-flight mass filter [121] and several types of ion traps: cylindrical micro ion traps that can easily form arrays [116, 122, 123], a rectilinear ion trap with planar electrodes [124] and a halo ion trap [125].

Ion source miniaturization has also advanced with realization of a carbon nanotube electron impact ion source [126]. The final goal is a reliable and fully integrated mass spectrometer with all of its components built as one part. Significant progress has already been made towards building a time-of-flight mass spectrometer on a chip [121].

Conclusion

This chapter has presented the rationale and prior state-of-the-art for the research detailed in subsequent chapters.

Functional materials suitable for typical ‘smart’ applications have been identified and their key properties, modes of operation and integration identified. Issues in their manufacture and subsequent application to engineering scenarios have been discussed and a need for other process to be investigated identified.

Layer-based manufacturing techniques have been introduced. Those most suited to the processing of the smart materials have been examined in most detail. Their viability has been discussed in the context of the state-of-the-art.

Lastly, novel applications for functional materials and LBMTs have been explored. This consideration has identified possible niches for combinations of suitable processing techniques and manufacturing process. This approach may indeed lead to improved manufacture of existing components and also allow fundamental design freedoms granted by manufacturing in a layer-wise manner.

It is the hypothesis of this study that LBMT components may exceed those manufactured by conventional means in terms of cost, size, functionality and flexibility in design.

3. Experimental Methods

Selective Laser Melting Techniques (SLM)

The SLM process was introduced in Chapter 2, in the context of a survey of current manufacturing research. A more detailed consideration of the SLM process is discussed here in order for the reader to gain a better appreciation of research discussed in Chapter 4. Especially with reference to the process by which untried material feed stocks are validated through experimentation.

The SLM apparatus used for the experiments were produced by MCP™ which designates its systems in terms of build envelope size. The systems employed for this research were the SLM 250 which has a square build envelope of 250mm x 250mm and finds general purpose application. The smaller SLM 100 was also used which has a circular envelope of diameter 100mm and is normally used to manufacture dental implants. Both systems incorporate laser and optics subsystems (Realizer Corp, Germany).

Powder

The feedstock material is one of the most resolution-limiting factors currently affecting SLS and SLM technologies. The partial and full melting which takes place in both processes, will limit the smallest possible features to be of the same order as the powder itself.

Metallic powders can be produced by several methods including gas atomization, gaseous pyrolysis and mechanical comminution [127]. The ceramic materials used in this work were ground from larger powder samples to produce a suitable powder size distribution. Grinding leads to a poorer degree of spherical conformity compared to the processes employed for metal powders and poorer packing density.

Gas atomization is perhaps the best powder preparation technique for SLM. Powders produced in this way present a high degree of sphericity. This is important when maximum packing density is required. If the powder packs well, to form a dense bed pre-melting, the consolidated component will be denser and thus display greater mechanical integrity. Packing can be improved by introducing fractions of differing powder sizes. The smaller particles can fill the voids left by the larger powder particles, as shown schematically in Figure 19.

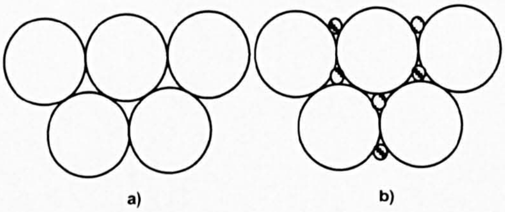

Figure 19 The inclusion of smaller powder particles to occupy voids and thus increase packing density.

The optimum theoretical packing density for mono modal spherical powders can be obtained. If closest packing is observed in a face centred cubic (FCC) arrangement;

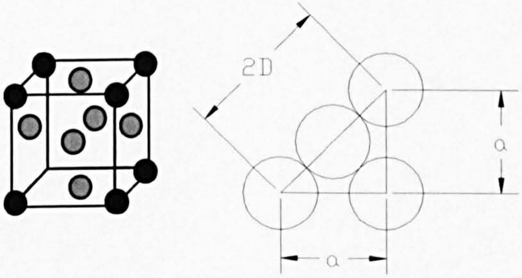

Figure 20 Packing density in face centred cubic (close pack spheres) powder arrangements.

If the unit cell has a volume of a^3 units, only a fraction of which is occupied by powder particles of diameter D then;

$$a = 2D \sin 45^\circ \tag{3.0}$$

Allowing the unit volume to be expressed in terms of particle diameter;

$$a^3 = \left(\frac{2D}{\sqrt{2}}\right)^3 \tag{3.1}$$

Within the unit cell there are four half particles at each face and four quarter particles at each corner i.e. the unit cell is populated by a volume equivalent to four whole particles. Therefore the ratio of occupied volume to unit cell volume for spheres of radius r is;

$$\frac{4\left(\frac{4}{3}\pi r^3\right)}{\left(\frac{4r}{\sqrt{2}}\right)^3} \tag{3.2}$$

$$\frac{\sqrt{2}\pi}{6} \approx 0.74048 \tag{3.3}$$

Therefore the maximum close packing density for a monomodal powder is ≈74%.

The flow-ability of the powder is also dependent upon the mean powder size. The finer the powder, the more likely agglomeration is due to electrostatic forces and adhesion due to humidity in the atmosphere. These issues have been addressed [128] in the SLM process on the micron scale in a vacuum chamber. A balance must be struck to ensure that the powder does indeed flow to an acceptable degree, yet be small enough to yield good resolution in the consolidated part.

Flow-ability of powder feed stocks was measured using a Hall flow meter. This apparatus consists of a funnel with a calibrated orifice through which the powder flows. The time taken for a known volume of powder to flow gives a comparative measure of how flowable a powder actually is.

The particle size distribution for SLM materials used in this work was analysed using a Malvern Instruments (UK) 'Mastersizer' 2000 laser diffractometer. This technique is invaluable in determining the effect of powder filtering using sieves to achieve appropriate powder size distributions. Scanning electron microscopy and X-ray diffraction were also employed to validate both the topography and composition of all the materials processed via SLM.

Laser and Optics

Currently all MCP SLM machines incorporate neodymium-doped yttrium aluminium garnet (Nd:YAG) lasers (IPG, Germany) which emit light with a wavelength of 1068-1095 nm at a power of 50-200W.

The scanning system used in this study incorporated a dual axis mirror positioning system (Cambridge Technology) and a galvanometer optical scanner, which directs the laser beam in the x and y-axis through an F-theta lens. The variable focussing optics are Sill 300 mm focal length lenses. These produce a focussed beam spot size of 60 µm diameter at 80 watts power.

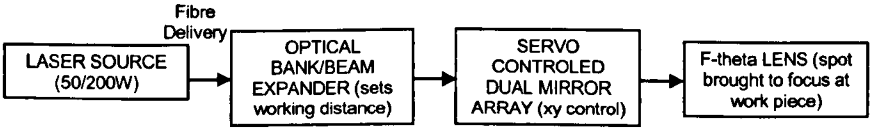

Figure 21 Optical Process Flow in MCP SLM Systems.

The MCP Realizer, is a commercial SLM workstation with a build speed of $5cm^3$ dense metal per hour on average. Since the powder is fully melted during the process, protection of the SLM-processed parts from oxidation is essential, therefore all metal powder processing occurs in an argon atmosphere with no more than 0.2 % O_2. The build is controlled using the propriety control software 'Fusco'.

Support Structures

A need arises for the support of layered structures when an 'overhang' feature exceeds a specific size. Unsupported material may collapse under its own weight. Features of this nature therefore require additional support which may be incorporated into the design or more commonly a sacrificial support can be included into the build process.

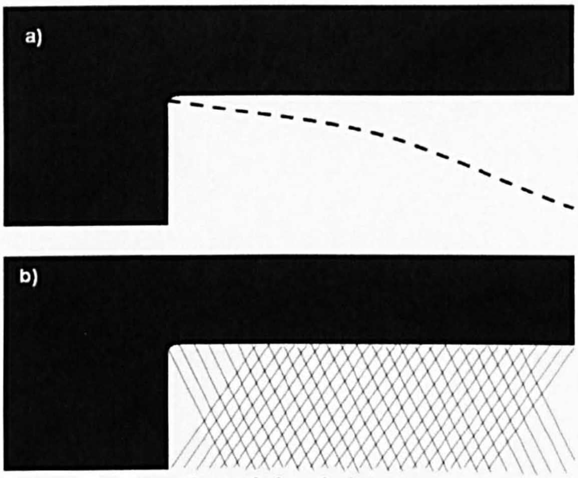

Figure 22 The effect of introducing support structures to overhanging features.

Sacrificial supports are commonly used throughout layer-based approaches. They are usually generated with the aid of custom software packages. The Magics™ X software (Materialise, Belgium) was used to generate all supports used in this study.

These supports are designed such that their contact with the desired geometry is minimal. This ensures that their removal can be achieved with little effort in secondary processing. It is also possible, via customising the build parameters for the support material, to weaken it so that it is easily removed.

'Support widening' is the process by which supports generated in custom software which have a thickness value of zero are widened to a suitable degree. This is a vital parameter which must be minimised to facilitate support removal. Support generation is further complicated when strain is induced in the build material. If the work piece is fixed to over rigorous supports, this often leads to undesirable strain compensation mechanisms namely bulk deformation of the whole part.

Large planar surfaces, parallel to the substrate are associated with 'hogging' (arcing of the part the opposite of sagging) as recrystallisation of molten material causes shrinkage in the direction away from the substrate heat sink. This is overcome by employing supports which partially constrain or alternatively building the part in another orientation.

Material Interaction

A fine balance is required at the laser/material interface to ensure enough energy is provided to the powder to cause melting but not to provide an excess which would cause excessive evaporation or spattering. This must all be achieved while maintaining fidelity to the original design from which the rastering pattern is computed. The raster is achieved using the Realizer machine control software.

The energy absorbed can be substantially reduced, if the material being processed has a high coefficient of reflectivity for the radiation wavelength used. If the material is highly reflective, then a significant fraction of the energy delivered will be reflected from the material surface and will not contribute to melting but resolution may suffer. This effect can be reduced if the powder is of a smaller mean size, which causes more localised reflection/scattering. As a result this reflected energy can still interact with surrounding powder particles and contribute to melting.

Absorbing coatings, often applied by aerosol, have been employed by manufacturers processing metal sheet with lasers. These increase laser absorption and hence reduce the power requirements of the laser source. To date this has not been used with SLM feedstock materials.

Upon melting at the surface, a plasma shroud forms. This serves to shield the work piece by absorbing and dissipating some of the incident energy. It should be noted that this is a dynamic situation, and the degree of reflectivity at the material surface varies with temperature as does the degree of absorption by the plasma shroud.

The induced melting and subsequent re-melting used to produce 'skin' tracks, results in re-crystallisation of the material upon solidification. The thermal regime under which re-crystallisation occurs will largely define the material properties. Although post build heat treatments and HIP [129] steps have been investigated, the processed parts should be as close to the finished article as possible. This is the case for both fidelity to the initial design and any required properties such as hardness and tensile strength. This strategy will ultimately reduce overall manufacturing cost and reduce the number or extent of finishing processes required.

Upon solidification the material properties will be affected by the ambient conditions. A principal concern is that undesired levels of oxygen may be absorbed, leading to embrittlement, or perhaps more catastrophically, explosive oxidation. This is especially hazardous when using a material which readily oxidises such as titanium and is compounded by the large surface area of the powdered feedstock.

Oxidation of the build material is suppressed by introducing an inert argon atmosphere to the build chamber. The O_2 content is limited to 0.2% or below. This is monitored, and subject to emergency interlock, by an oxygen detector.

During solidification, shrinkage occurs in the material that has been laser heated. If a structure is fully constrained and dense, then residual strains will be introduced to the material. This strain is often manifested as a distortion of the part. Further material deposition often worsens the situation and build failure occurs due to non-uniform powder deposition. This effect is minimised by orientating the geometry in way such that it may deform and compensate for stress 'naturally' or alternatively minimising the volume that is 100% dense. Internal features, curved edges or shells allow localised stress relief.

Parameters

The software that accompanies MCP SLM machines allows comprehensive control of build parameters. The 'bolt on' nature of the machine assembly also allows for the introduction of supplementary variables in addition to those which are software governed.

The user is able to vary oxygen levels, substrate temperature and the over-pressure caused by an argon feed. These parameters serve to modify the feedstock response to laser interaction. The heater plate is especially useful for controlling the rate of heat sinking and consequently recrystallisation. For most metal processing the user will require oxygen to be held at a minimum to limit high temperature oxidation. However, the ability exists to admit partial pressures of air for the processing of some ceramics for example.

The energy density at the build surface is the product of three variables laser power, laser spot size and raster speed (which is in turn contrived of point-to-point distance and exposure time). The laser power can be varied from 10-100% in increments of ~1%. These parameters must be balanced to ensure sufficient melting occurs but sublimation/ablation does not.

The raster strategy that enables the laser to completely expose a selected area may also be varied. The hatch spacing or distance between the centres of adjacent tracks can be adjusted. This selection is highly dependent upon the melt temperature of the feedstock as lower melt temperature materials will have wider heat affected zones, so less laser coverage will be required. Contour or skin raster lines constrain the melt pool to the inside of the part. The facility exists to adjust this skin spacing and vary its energy inputs independently of the strategy for the bulk material. This is intended to optimise surface finishes on the surfaces parallel to the build direction.

Digital Light Processing (DLP)

The apparatus used for this study was the Perfactory Mini™ custom (EnvisionTec, Germany). This system allows for the interchange of objective lenses, meaning that sizes of the build envelope and pixels, at the build surface, can be varied.

The build envelope is a matrix of pixels which can be enlarged or reduced by using appropriate optics. Enlarging the build envelope comes at a cost to resolution. This trade off occurs because the pixels will also be enlarged by the same factor as the envelope as a whole. Larger build envelopes are desirable because a larger area can be built up. This is of special importance for processes in which the build time per layer is constant.

The optics consisted of the Perfactory SXGA+ 85mm which produces a rectangular build envelope of 20.83mm x 27.77mm. The platform is mounted on a stepper actuator which is capable of linear translation accurate to +/- 6μm.

An incandescent bulb is used as the light source. This emits a spectrum which is filtered to appear blue (≈450-495nm) at the build surface. The manufacturer regards the specific wavelength to be proprietary knowledge and it is therefore not disclosed. This protects the manufacturing process to a degree and limits the use of feed stocks, from competing suppliers.

Material Interactions

The photopolymer used in this study was an acrylic resin – Pentaerythritottri/tetra-acrylate (CAS 4986-89-4) + 1,1,1 Tri-hydroxymethylpropyl - triacrylate (CAS 15625-89-5, 3524-68-3)

Photo-polymerisation is achieved via the addition of initiators to the monomer [130]. Initiators are molecules which readily decompose producing free radicals. This reaction can be exploited to produce resins that polymerise upon being exposed to radiation of a given wavelength.

Free radicals are created by the unpaired electrons that form as a result of a bond being broken. The free radicals react with carbon-carbon double bonds in monomer molecules. The monomer is then left with a surplus electron, becoming a free radical and polymerisation is observed.

This process comes to halt through the termination reaction. This may occur in two ways. In the first instance, two growing polymer chains meet end on, known as coupling. Alternatively the chain end may supersede a hydrogen-carbon bond at the mid-section of another chain which is termed disproportionation.

In some instances, an unpaired electron will be available mid-chain and as such distant from the propagating end. These may chain transfer to polymer, meaning that a new branch will be formed. The length and degree of these cross links will determine the macroscopic mechanical properties of the polymer.

Given that this process occurs in the resin basement, several criteria must be met order for the material interaction to produce desirable results.

Firstly, exposure time must be considered. This must be long enough to ensure that a significant degree of polymerisation has occurred in-litho. If this is not the case then the film will not maintain shape or adhere to previous layers. Further time, ex-litho, should be allotted to allow the polymer to reach equilibrium before agitation. Again this would serve to compromise its adherence to previous layers. Linked to exposure time, is the exposure intensity which can be adjusted with exposure time to give the desired level of cure.

Parameters

The EnvisionTec Perfactory software allows several parameters associated with build conditions to be freely adjusted. This allows for variation between feedstock batches and also entirely new material systems. They may be adjusted independently to reach a suitable parameter set.

Upon exposure the resin basement peels away from the substrate on which the part is forming. This allows uncured material to occupy the void left behind. The separation distance, waiting time for resin flow and velocity of 'peeling' can all be adjusted for variations in material viscosity.

Similarly, the exposure time and waiting time after exposure (during which additional cross linking occurs) can be varied. These must be balanced to result in a sufficient degree of curing. Under exposure results in parts that readily deform as additional layers are deposited, while over exposure produces flaking, poor adherence between each build layer and surface defects caused by shrinkage.

The Perfactory software also enables use of an enhanced resolution mode (ERM). This option causes two exposures per build layer to occur. Both images are identical but shifted by one pixel. Parts built in this manner will have a smoother finish on surfaces perpendicular to the build direction.

Other algorithms can be applied while bitmap processing, in order to minimise pixilation. Customising the degree of this smoothing for an output of given resolution is termed anti-aliasing.

All support, when required, was generated as for the SLM geometries by using the Magix X software package.

Scanning Electron Microscopy (SEM)

SEM was used to analyse of several aspects of this work. The instruments used were the Hitachi S-2460N (high vacuum), the CamScan X500 FEG SEM Crystal probe optimised for electron back scatter detection (EBSD) and the JEOL JSM 7001f FEG SEM.

When the specimen under investigation was metallic, maximum acceleration voltages (e.g. ≈ 25 keV) were used to optimise resolution. Non-conductive samples were sputter coated with gold to prevent sample charging. While imaging in these materials, lower electron acceleration voltages (e.g. ≈ 12 keV) were used at some cost to resolution but with a marked improvement to image contrast.

All the instruments used, are fitted with an energy dispersive spectrometer (EDS) which permits X-ray spectra to be acquired. This allows the operator to identify the chemical composition of the material under investigation.

Transmission Electron Microscopy (TEM)

TEM was used for the analysis of NiTi samples produced by SLM. This was all undertaken using a JEOL 2000FX which uses a maximum acceleration voltage of 200keV. This microscope was used to obtain selective area diffraction (SAD) patterns to identify the crystallographic phases present in NiTi samples.

TEM offers higher resolution than SEM, as well as electron diffraction. The operation of TEM is based upon detecting electrons which have passed through a thin section of the material under examination. This, provides information about the internal structure of a material and not just the surface region as in SEM [131].

Energy Dispersive X-ray (EDX) Analysis

Upon bombardment with electrons, matter may radiate X-rays. The emitted X-rays are characteristic of the processes whereby electrons relax within a particular atom. Therefore this property can be used to identify the source atom.

The Hitachi S-4000, JEOL JSM 7001 and CamScan microscopes were all fitted with EDX analysis apparatus. These allow point specific identification and regional identification of sample composition. All incorporate a semi-conductor detector which when exposed to X-rays causes the excitation of electrons to a conduction band and an electric pulse is recorded. The energy of this pulse is proportional with the energy of the X-ray.

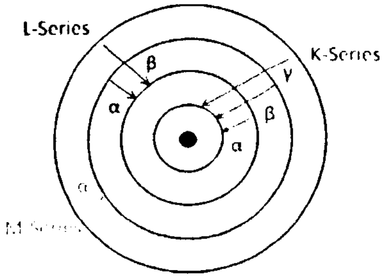

Figure 23 X-ray emission upon electron relaxation.

The detection of lighter elements is prevented with this technique due to x-ray absorption which takes place at the detector 'window'. At low X-ray energies (< 1 keV) associated with K energy shells of lighter elements, insufficient signal levels will penetrate through this beryllium window.

EDX was used to verify the elements present and to investigate contamination of NiTi samples manufactured by SLM. EDX was also used to analyse the $BaTiO_3$ samples after laser processing to discount dissemination of oxygen and verify the elemental composition.

X-ray Diffraction

A Rigaku Miniflex diffractometer was employed to record X-ray diffraction patterns of the materials used within this work. The diffractometer consists of an X-ray source which operates by accelerating electrons through a potential (40 kV) toward a copper target. The electron impact causes photoemission in the form of X-rays predominantly associated with the Cu Kα shell with a wavelength of 0.154051nm. These X-rays are guided through a filtering window to give an approximation to monochromacity. X-rays of other wavelengths will also progress to the specimen but with relatively low intensity. The interaction of X-rays with crystalline materials yields a diffraction pattern unique to each material. This is characterised by the well known Bragg equation;

$$n\lambda = 2d\sin\theta \qquad (3.4)$$

Where n refers to the order of the associated diffraction maxima (usually 1st and brightest), λ is the wavelength of the incident X-rays, d is the 'd' spacing between atomic planes and θ is the diffraction angle.

The associated proprietary software allows the post processing of diffraction data recorded in this way to remove background radiation, perform averaging operations, to compensate for non-monochromacity and to calculate integrated peak intensities.

X-ray diffraction is useful for identifying the crystalline phases present in a material. It can also be used to assess the relative quantities of phases and also measure the degree of crystallinity. This is useful when examining the effect of heat treatments under which recrystalisation has occurred.

This diffractometer is best suited to analysing powder samples. A large number of crystals in the sample will be randomly orientated and so representative diffraction patterns will be obtained. The patterns obtained from the sample are compared to reference patterns from a library or with computer generated models. For a defined unit cell, the location and relative intensities of the characteristic peaks of a sample can be computed from these references. Several internet based lattice parameter libraries are available for reference. The Cambridge Database Service (CDS) was used during this study.

Surface Profilometry

Surface profiling was undertaken to investigate the roughness of parts manufactured by DLP. The apparatus used for this purpose was a Veeco Wyko NT3310 interferometer. This apparatus exploits the path difference of light reflected from the sample compared to a reference beam, Figure 24.

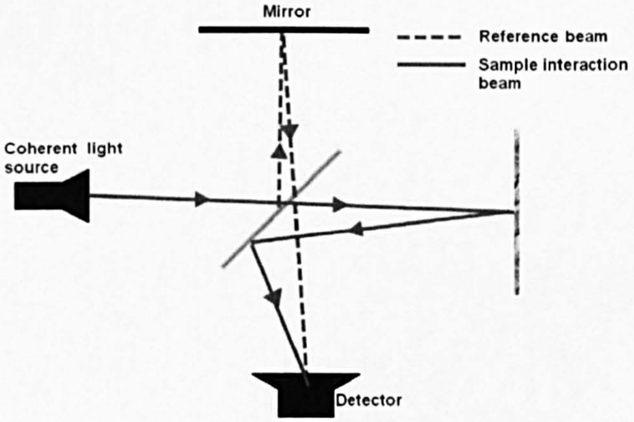

Figure 24 Simplified coherence scanning interferometer after the Wyko NT3310.

In this technique, a coherent light source illuminates a Michelson interferometer (beam splitter). A fraction of the incident light shines on the sample surface and the remainder travels directly to a detector serving as a reference. Light is reflected back from the sample and directed to the same detector. A path difference is caused by the roughness of the sample surface and the two beams shift in and out of phase. An interference pattern will be observed at the detector. Software interprets this pattern to map the surface of interest.

Apparatus, like the Wyko system used in this study, have stage mounted optics which permits a range of focal lengths to be 'scanned'.

Differential Scanning Calorimetry

This technique is used to measure the amount of energy required to raise the temperature of a specimen. This characteristic is of use when evaluating changes in state and material structure as result of heating or cooling.

Crystalline materials may experience a phase change, while amorphous samples may pass through a glass transition. The atomic or molecular restructuring associated with these changes requires a specific amount of energy (latent heat) to be provided or dissipated which is characteristic of the phase change.

The calorimeter consists of a temperature controlled vessel into which the sample is inserted. This is heated or cooled with liquid nitrogen causing the sample temperature to change. The temperature in the vessel is precisely monitored and appropriate energy supplied or withheld as the system is cycled through a range of temperatures. That is to say, a material going through an endothermic phase change, more energy has to be required to maintain the rate of temperature rise and this is measured by the power drawn by the furnace. If the material goes through an exothermic phase change the converse occurs.

The calorimeter used in this study was a Metler Toledo DSC 822 assisted by the STAR^e analytical software. Measurements were taken comparing the precursor NiTi powder to SLM parts.

Raman Spectroscopy

This technique exploits the interaction of monochromatic laser light with the phonons of the sample material. The incident light is subject to a shift in energy if inelastic collisions occur.

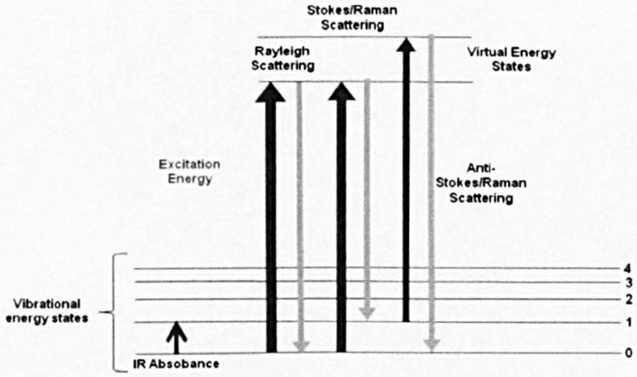

Figure 25 Vibrational modes used by Raman spectroscopy.

Rayleigh scattering is the dominant process for the incident light caused by elastic interactions. This Rayleigh component is reflected with the same wavelength as the initial light source. A notch filter is used to reject this light and only inelastically energy shifted photons arrive at a Si charge coupled device (CCD) detector. These energy shifts (Stokes/Anti-Stokes) are characteristic of the material under investigation.

Raman spectra were obtained in this study following excitation using radiation from an argon ion laser at a wavelength of 514.5 nm. The power impinging on the sample was kept at 17mW. A Jobin-Yvon LabRam spectrophotometer with subtractive pre-monochromators coupled to the third spectrograph / monochromator with a 1800 grooves mm^{-1} grating was used for recording the spectra. A Peltier-cooled charge-coupled detector (CCD at 80 K) was employed to detect the Raman signals. All of the spectra were recorded in back scattering geometry with a 50x microscope objective.

Mass Spectrometer Apparatus

A well established test rig was used to evaluate the performance of mass spectrometer components manufactured by DLP. Sufficient vacuum was obtained in the test vessel using an Edwards two-stage rotary pump. This provided a roughing vacuum taking pressure from atmospheric down to 1×10^{-1} Torr. An Edwards turbo-molecular pump was then used to reduce pressure from 1×10^{-1} Torr to approximately 5×10^{-6} Torr. The test pressure is required to ensure the mean free path of ions is large. The vacuum was monitored using a Leybold Ionivac vacuum gauge. This also provided a calibration standard to evaluate the pressure sensitivity of mass spectrometer components.

For the preliminary spectrometer design, a standard ion source was used to ionise gas samples. Varying the current supplied, adjusts electron emission and thus ion density. Ideally a large number of ions will then progress into the mass filter

A custom electronic control unit (ECU) was used to control the ion source voltages; to provide RF/DC drive voltages for the mass filter; and to measure the current in the Faraday cup detector. The ECU also sends the signal to the computer to be plotted. This unit allows for complete control over voltages between rods, extraction/focussing potentials for Einzel lenses, and bias at collector.

The manufacture of some mass spectrometer components required coating with a conductive film. All coating was done by evaporation of gold onto the required surfaces using an Edwards E306A Coating System.

4. Selective Laser Melting of NiTi Alloys

Introduction

Advances in the SLM process in terms of reliability, part quality and build size have widened the applications suitable for this technique. This potential has encouraged experimentation with several alloy groups to establish their process compatibility. The selection of these alloys has broadly been driven by their use in industries such as the aerospace and biomedical hence 316L steel and Ti 6Al4V alloys have been the first to find widespread use with SLM. However, many materials are still to be explored.

One engineering material of significance to several industries is the shape memory alloy nitinol (NiTi). Although widely used and well understood, this material has not been previously processed by SLM.

The geometry of some shape memory components, such as valves and springs, means that manufacture by conventional approaches is often labour intensive and therefore costly. By employing SLM instead it is proposed that complex-shape components which display the SME can be manufactured.

The methods for the characterisation and preparation of metal feed stocks for the SLM process are as immature as SLM itself. A standard approach to this process is yet to be formalised. The most important general concerns are; the flowability of the powder, the energy required to melt the powder and the nature of the material upon recrystallisation.

Information about these factors, combined with characterisation of the material after SLM processing can be used to formulate the optimum build parameter set or at least an approximation when parameters are discontinuous.

Once the feedstock and SLM process have been optimised to yield adequate material properties, then the resolution of the system can be evaluated. This may be achieved using test structures such as concentric circles or thin walls with ever decreasing dimensions. By observing when discrete features are no longer built in this the resolution can be obtained.

Any subsequent analysis is then tailored to the material under investigation. Measurements can be used to establish whether there has been an enhancement or degradation of key material microstructures or properties caused by the SLM processing.

In this chapter selective laser melting has been used to build high aspect ratio, three-dimensional NiTi electro-mechanical components. Cantilever beams and springs manufactured in this way have been trained and actuated demonstrating the process is suitable for electromechanical applications.

Material Preparation for SLM

The characteristics of powder shape and size are important in the SLM process. The powder must flow readily from the recoater to the build platform. Particles with smooth surfaces flow more readily within the powder bed, leading to a higher ‘loose’ density. Loose density contributes significantly to the final density of components manufactured in this way as there will be a reduced void content before melting. Reducing the void content facilitates heat transfer in the powder bed. Hence a more uniform melt pool and symmetric heat affected zone will be observed.

Particle shape is an important factor as symmetrical particles pack more densely. Consequently spherical powders are preferred. The surface and granulometry parameters of the powder are closely related to the material and its production process. The powder used in this study was supplied by Crucible Materials Corporation and the composition was $Ni_{55}Ti_{45}$ by weight. It was manufactured by gas atomisation.

Particle Size Analysis

Particle size analysis was performed on the NiTi feedstock as supplied. The powder was reduced down to a predominantly monomodal distribution as shown in Figure 26 by graded filtering. The mean powder particle size was shown to be 75μm with standard deviation of 15μm.

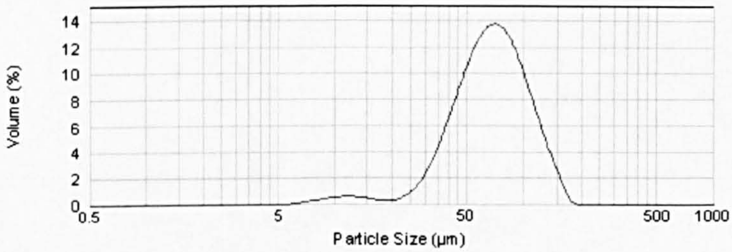

Figure 26 Particle size analysis of NiTi powder as provided by Crucible Materials.

A second mode is observed with mean diameter of 6.5μm. This is likely due to satellite particles which are separated during the filtering process or indeed during the process of particle size analysis. Some of which can be observed in Figure 29.

Powder Composition

Figure 27 shows the phase diagram for binary NiTi alloys. The equiatomic composition of this alloy was retained from the liquid melt, through cooling to the solid.

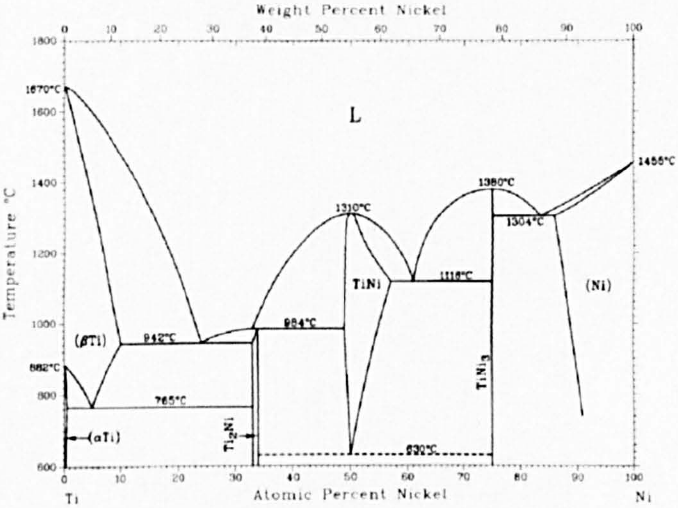

Figure 27 The NiTi phase diagram after Bastin et al [126]

It is significant for this study, that the melt temperature for $Ni_{55}Ti_{45}$ is 1310°C. The melting point places an immediate requirement upon the processing parameters. The incident laser must provide sufficient energy to raise the powder bed temperature from ambient to a localised temperature in excess of 1310°C. The specific heat capacity of NiTi is given elsewhere [132] as $\approx 850 Jkg^{-1}K^{-1}$ (phase dependent). Furthermore it must provide the required latent energy to cause complete melting. Ideally during this process Marangoni stirring effects [103] will be observed ensuring a uniform solid solution upon re-crystallisation.

Differential Scanning Calorimetry

The phase transformation temperatures of the feedstock material and the processed material were evaluated using DSC. Figure 28 clearly shows the changes in specific energy which accompany the various phase changes consistent with NiTi alloys which exhibit the SME in the feedstock powder.

If the heating section of the curve is considered first (bottom), then it can be observed that the transition from the low temperature martensitic phase to the high temperature austenitic phase begins at 53.7°C. This is commonly referred to as the austenitic start temperature, A_s. This transformation continues until complete (A_f) at 94.5°C. Upon cooling (top) the martensitic start temperature (M_s) occurs at 62.1°C and continues down to the martensitic finish (M_f) temperature of 23.3°C.

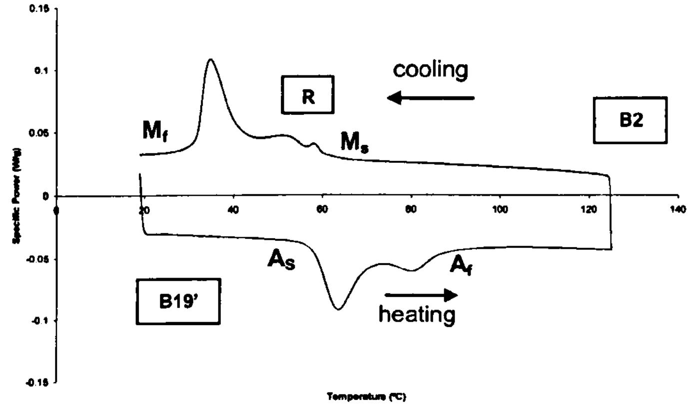

Figure 28 DSC of NiTi powder as supplied by Crucible Materials.

These transition temperatures are typical of NiTi alloys and the associated features can be attributed to appropriate phases. This data is summarised in Table 2.

The evaluation of these material properties provides a baseline from which the effect of laser processing can be measured. Without thermal in situ microscopic or x-ray analysis, it is impossible to be certain which of the phases are present at each characteristic temperature. However, these phases can safely be attributed to the corresponding regions within the DSC given certificated material composition and evaluation of the phases present at room temperature.

The four stage transition as observed in Figure 28 has been associated with nickel rich alloys of the type ($Ti_{49.3}Ni_{50.7}$ at%) subjected to thermal cycling [133, 134] and not typical of a fully annealed equiatomic alloys.

Juncture	Temperature (°C)	Associated Phase	Class	Transition
A_s	53.7	B19'	Monoclinic	Exothermic
A_f	94.5	B2	Cubic	
M_s	62.1	B2→R	Cubic→Trigonal	Endothermic
M_f	23.3	R→B19'	Trigonal→Monoclinic	

Table 2 Phase transition summary of NiTi powder as supplied by Crucible Materials.

It is proposed that the presence of the intermediate R-phase (Ti_3Ni_4 precipitates) is a result of 'coring' during recrystallisation in the gas atomisation process. Coring occurs because the cooling regime of metal powders post atomisation is by no means uniform across the metal sample or indeed within a powder particle itself. Therefore it is reasonable to conclude that unless subjected to post manufacture thermal treatments that the material will not be monophasic. That is to say, variation in cooling rate through the powder cross section is expected to lead to variation in composition, which may result in a Ni rich outer layer of the powder. It is proposed that this layer may be constituted from the Ti_3Ni_4 R-phase. This is thought to have a higher melt temperature than other phases which would solidify first at the powder particle core.

Since the R-phase is associated with thermally cycled NiTi alloys it was proposed that if the presence of the R-phase could be maintained post SLM processing then this could be advantageous. This would result in components which would be pre-aged upon manufacture.

Microscopy

To establish that the morphology of the feedstock powders is largely spherical, a powder sample was analysed by SEM. This was achieved by dusting carbon tape with the sample and manually agitating to remove poorly adhered powder particles. Figure 29 shows a typical micrograph of the powder feedstock.

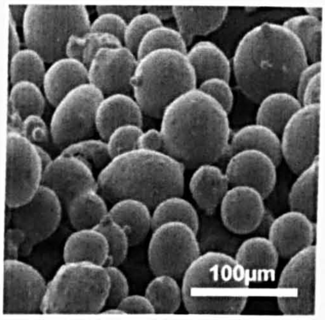

Figure 29 NiTi Powder sample subject to SEM analysis.

It was evident that the size distribution was consistent with that evaluated by particle size analysis. A high degree of spherocity is observed which is typical of powders produced by gas atomisation and thus likely to provide the near optimum loose packing density of 74%.

Satellites attached to larger particles via 'neck' type structures are commonly observed in gas atomised powders. Secondary sintering can occur in the gas stream emerging from the nozzle. Although this is not ideal, the occurrence of these features is sufficiently infrequent, and unlikely to influence the flowability of the powder significantly.

Similar features and sintered agglomerations can be observed in recycled powder samples processed by laser methods. Most importantly the powder was found to flow sufficiently enough to be compatible with the MCP SLM 250 recoater mechanism.

X-Ray Diffraction

Before SLM processing via the feedstock was investigated by X-ray diffraction analysis. This technique permits the identification of crystalline phases and permits the detection of their percentage composition. Figure 30 shows the X-ray diffraction pattern for 2θ angles of $35° < \theta < 70°$.

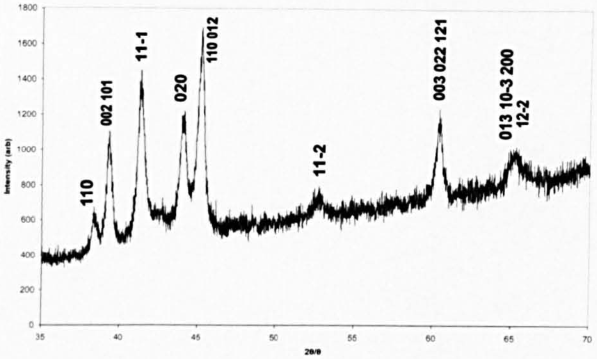

Figure 30 X-ray diffraction analysis of NiTi powder as supplied by Crucible Materials.

The peaks observed are consistent with the "low temperature" martensitic phase which is consistent with the DSC findings observed in Figure 28 being caused by the martensitic to austenitic phase changes associated with the shape memory effect. These are summarised in Table 3. The lower intensity peaks observed in Figure 31 are not labelled as they cannot be discerned from the experimental results.

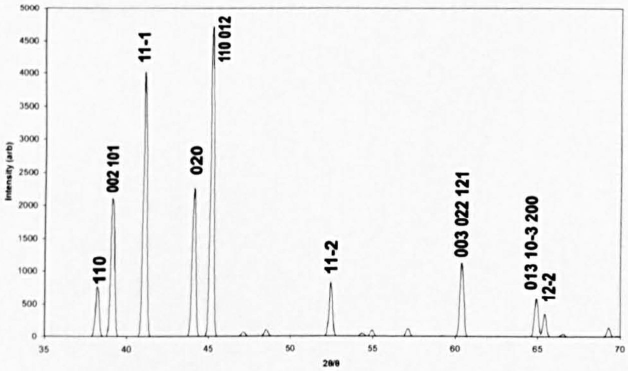

Figure 31 XRD peak summary of NiTi and reference data after Cuevas et al [129].

Contamination of NiTi alloys during heat treatment is widely reported and more specifically their sensitivity to oxygen contamination [135]. This has been shown to have a marked effect upon the observed SME. Therefore, verification of crystal structure pre and post processing is essential.

It is apparent upon inspection of Figure 30 and Figure 31 and comparison in Table 3 that the spectra are consistent with the expected martensitic NiTi phase (monoclinic) at room temperature.

θ (°)	Miller Index	d-Spacing (Å)	Error θ (°)
38.2	**110**	2.354	-0.1
38.3	110		
39.1	**002, 101**	2.300	0
39.1	002, 101		
41.2	**11-1**	2.19	+0.1
41.1	11-1		
44.1	**020**	2.061	0
44.1	020		
45.1	**110, 012**	2.010	-0.1
45.2	110, 012		
60.3	**003,022, 121**	1.534	-0.1
60.4	003,022, 121		

Table 3 Comparison of selected peaks for NiTi in the monoclinic phase showing experimental results (grey) compared to reference results (white).

Although the R and martensitic phases may coexist, no R-phase is observed in the XRD above. This further supports the hypothesis that the R-phase forms in the NiTi powder particles through a coring process.

Powder Processing

Build Parameters

The incorporation of a new material into the SLM process requires extensive experimentation to optimise build parameters. Geometrical properties such as surface finish, density and smallest resolvable feature size are all dependent upon the energy density of the impinging laser source.

Build parameters which are known to yield acceptable structures in other materials were used as a starting point. A fixed layer thickness of 125μm± ≈10μm and fixed spot size of 80μm with a fixed contour regime were used to build seven samples with the build parameters detailed in Table 4. These values were selected because they correspond to the parameter window commonly exploited to process titanium alloys. While the optimum parameter set will probably vary from that for titanium this represents a good starting point.

Sample#	Laser Power (±1.5W)	Exposure Time (ms)
1	15	300
2	16.9	350
3	18.8	400
4	22.5	450
5	24.4	500
6	26.3	550
7	28.1	600

Table 4 Build parameters used to build solid NiTi samples.

Density Analysis

SLM uses single component powders, which are fully melted by a laser beam as it rasters the build design over the powder bed. The melted material solidifies leaving a fully dense remnant structure. SLM is similar to SLS but the main difference is the partial surface melting or sintering of the powder in SLS compared with the full melting in SLM. SLS uses base metal powders coated with polymer binder components, or a combination of low and high melting point alloys, for that reason SLS processed parts are frequently not fully dense and hence have relatively low strength [136] requiring post-processing before being of any significant engineering use.

Figure 32 shows the variation of part density as a function of laser dwell time at the powder bed for a constant laser power. Relative density was calculated by measuring the mass of 10mm cubes and comparison with an ideal mass of 6.5g, the density of the NiTi alloy used in this study. It can be shown that near 100% dense NiTi parts can be obtained via SLM.

The inset SEM images are of the uppermost powder layer which had not been re-melted. These SEM's show the surface of the shortest and longest exposure times used in this study along with the corresponding R_a, which is a convenient measure of surface roughness. It is also apparent that the increased densities due to longer dwell time are correlated with a marked improvement in surface roughness.

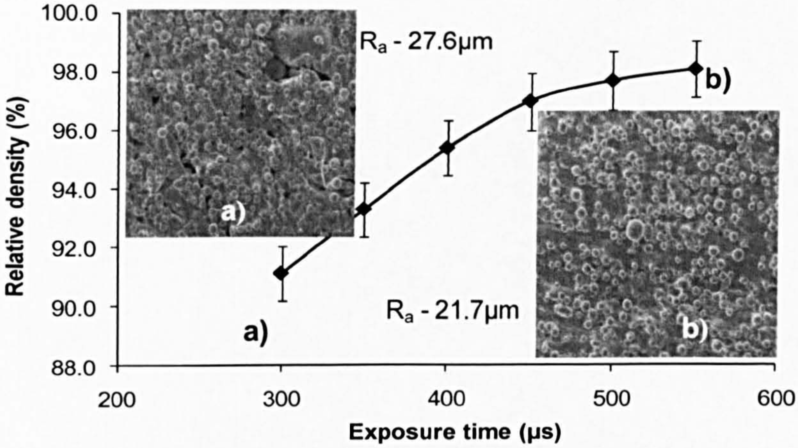

Figure 32 Increasing density of NiTi powder with exposure time.

Inset a) in Figure 32 clearly shows voids left by the use of insufficient laser energy. Inspection also indicates that there is a larger spread in the sizes of satellite particles on the component surface compared with those observed in inset b). This is more consistent with the unprocessed powder supply.

Resolution Testing

The resolution of components manufactured by LBMT is of prime concern. The pitch between the laser raster lines is a significant process parameter which contributes to maximum resolution. The raster pitch of the laser beam has to be smaller than the track build width to ensure good bonding between the melted particles and minimize porosity. However the build width is not only determined by the laser beam size but also by the laser power, exposure time and powder size. When power density increases, the track width becomes wider than that of the laser beam. This results in an overlapping of laser tracks and re-melting. Figure 33 illustrates this effect and shows a plan view of a succession of 500μm wide walls with decreasing separation from left to right. At a separation of between 100 and 200μm, the melted zones between adjacent walls begin to coalesce. Below a separation of 50μm, the build becomes semi-continuous which indicates the 'resolution' limit that can be achieved with the NiTi powder size distribution used here.

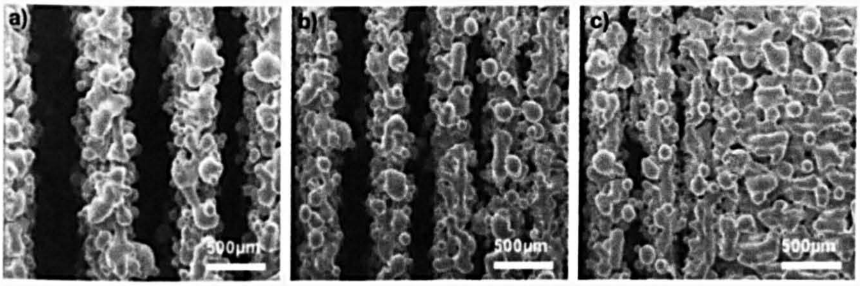

Figure 33 Resolution test on NiTi powder processed by SLM.

The top surface of the walls reveals a typical surface topography of SLM parts which have not been subjected to surface re-melting or 'skin' processing. These methods result in the re-melting of the top surface of the component and rely upon the molten metal flow to result in a smoother surface finish.

It can be seen in Figure 33 that the surface roughness of the components in the planes perpendicular and parallel to the build direction is largely caused by the adherence of semi-melted satellite particles which adhere to the main body of the part. Closer inspection of Figure 33 highlights the satellites which are much larger than powder particles depicted in Figure 29. These larger globules are an agglomeration of two or more powder particles which is indicated by necking and their overall dog bone shape.

It should be also noted that in Figure 33c) the third wall from the left has been resolved in an optical/laser interaction sense. However, due to the aspect ratio of the cavity left in between walls, un-melted powder particles have coalesced and simple part cleaning has not been sufficient to remove them. Consequently resolution is also affected by the aspect ratio of components and the ability to remove undesired remnants. This is typically observed when the design requires 'nested' features. Although such features can be resolved by the manufacturing technique post processing will be required to remove the unmelted material.

Microscopic Analysis of Build Structures

Once the near-optimal build parameters had been identified sample structures were produced and subjected to further analysis. It was proposed that porous SLM samples would not be capable of enduring the strain required to achieve two-way shape memory effect. Only samples produced using this optimal parameter set were subject to 'training'.

Post SLM processing, solid samples of NiTi were polished using standard preparation techniques, and finally etched using a $3HNO_3 + 2H_2O + 1HF$ solution after Gall et al [137]. This solution causes preferential etching along grain boundaries rendering grains visible that would otherwise be indiscernible under typical SEM examination conditions.

After etching, the samples were cleaned and force dried in a hot air blower then allowed to cool in air. This permitted the sample to recrystallise into a 100% martensitic structure for SEM inspection.

In situ heating of the specimen was performed to verify the phase transformation temperatures by observation. This allows direct comparison with results obtained by DSC.

Grain Structure of Polished and Etched Samples

Figure 34a) and b) show a grain structure typical of NiTi alloys in the martensitic phase. This is characterised by the spear-like structures emanating from rib planes.

Grains are typically 10-100μm in length and less than 5μm in width. Grain orientation appears to be entirely random and bears no relationship with the raster direction which is from top to bottom. Frick et al [138] have discussed overcoming issues pertaining to manufacture using NiTi alloys. In which the advantages of obtaining cast type grain structures in NiTi components are evaluated. Dendrites which are typical of cast grain structures are observed in Figure 34. It is proposed that by control of the substrate cooling rate the grain size can be controlled to a degree which is inherent to the shape memory effect on a macro level.

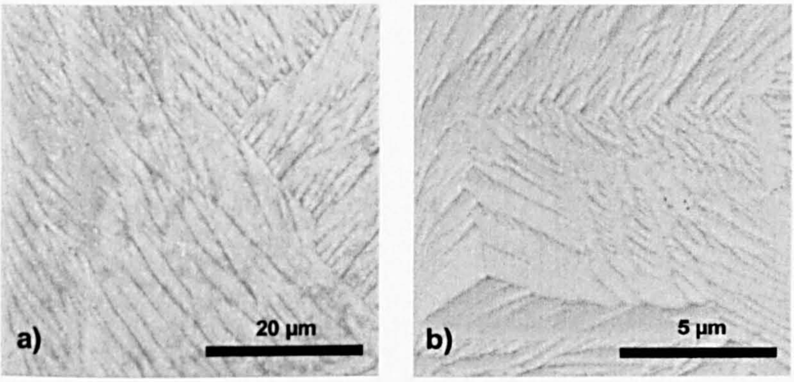

Figure 34 Secondary electron SEM images of etched NiTi build structures (Hitachi).

Figure 35b shows an exception to the typical grain structure observed in the material. In highly localised areas, a chamfering of the needle like martensite grains is observed. This is indicative of a contaminant within the build material. Secondary electron images in Figure 35 highlight this feature in more detail. Comparison of Figure 35b and Figure 35a shows the variation in structure compared with the bulk material. It is notable how this structure protrudes from the surface of the etched surface.

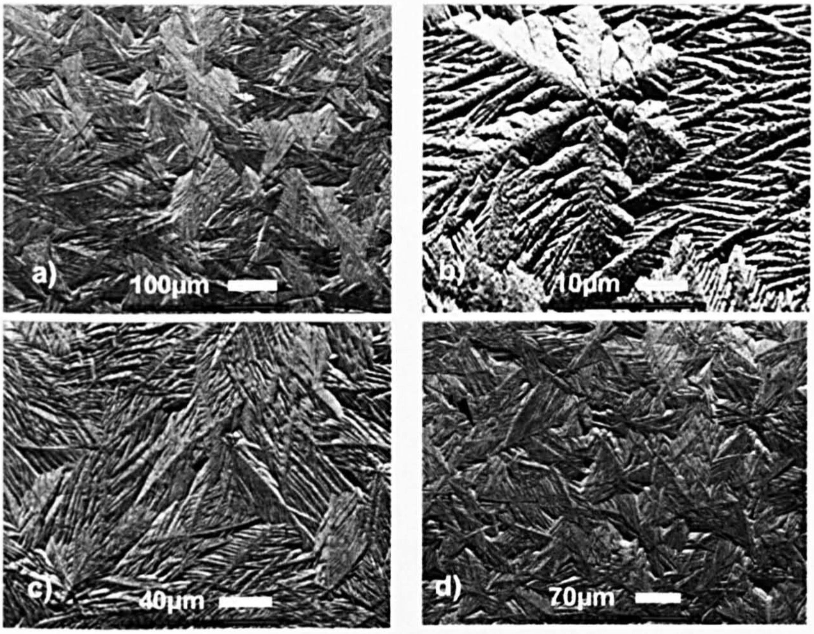

Figure 35 Back scattered electron SEM images of etched NiTi samples (Camscan).

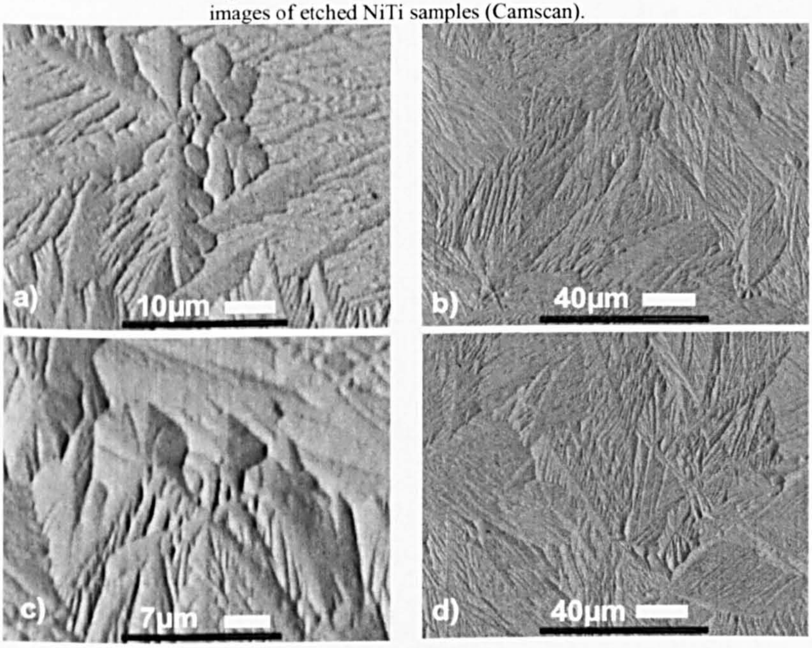

Figure 36 Secondary Electron SEM images of etched NiTi samples produced by SLM (Figure 34 b) and c) are from the same region as are Figure 34 c) and b))(Camscan).

The size of this feature, ≈ 50μm, is typical of other powder feed stocks that are commonly used with the SLM apparatus further suggesting that it may be a contaminant. For this reason a repeat analysis was performed with alternative preparation techniques.

Inspection of Figure 36c) clearly shows a different grain structure from that observed in the bulk material. Contrast observed between grains (and not grains and grain boundaries) is also indicative of a difference in atomic number.

EDX and in situ Thermal Analysis of Build Structures

To examine the shape memory effect in the build material further and to examine contaminated, regions a porous sample was selected for analysis. It was proposed that a porous sample that exhibited the SME could be used as a temperature sensitive filter. That is to say a change in temperature could result in an opening or closing of pores. To evaluate whether this was the case, a thermal stage was used in conjunction with a scanning electron microscope which permits cycling the temperature of the sample while performing in situ observations.

The sample for in situ analysis was not etched after polishing. It was also allowed to dry after cleaning at room temperature to minimise the extent of recrystallisation. This permits the observation of texture, as the phase transformation occurs. The temperature profile of the in situ analysis is shown in Figure 37, together with the arrangement of the heating elements.

Monitoring the sample temperature directly was not possible as fixing a thermocouple would obscure observations. Temperatures at the furnace and heated surface (which serves as an approximation to sample temperature) are detailed below.

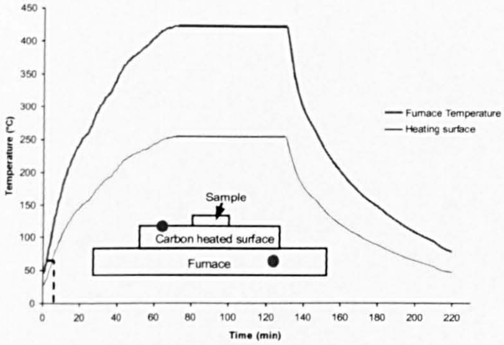

Figure 37 In situ thermal cycling of NiTi processed by SLM (dots indicate thermocouple locations).

Images were collected at 20s intervals as temperature was varied. When a marked phase change was observed (from martensitic to austenitic) this was correlated with experiment time and a transition temperature can be estimated. From in situ analysis the transition temperature was observed to occur at 55°C which is consistent with the transition temperature found from DSC. The reverse transition was not observable because of the introduction of texture in the forward phase change which is retained on cooling.

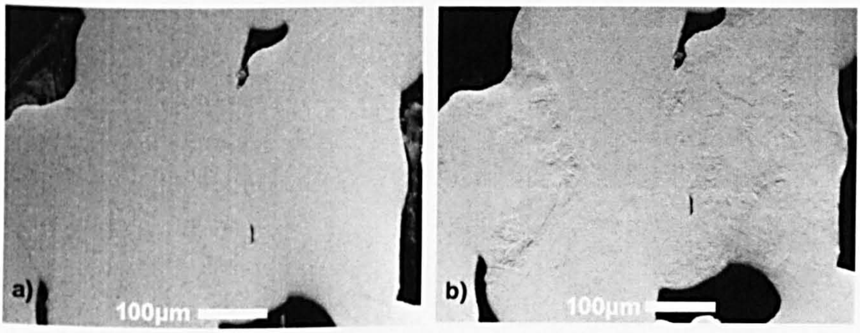

Figure 38 Porous NiTi pre (a) and post (b) thermal cycling.

The grain structure after thermal cycling is identical to that observed in Figure 35 and Figure 36 indicating that after cycling the alloy returned to its initial microstructure. A sample was cycled a number of times and in situ observations made again during which the associated microstructures did not vary greatly.

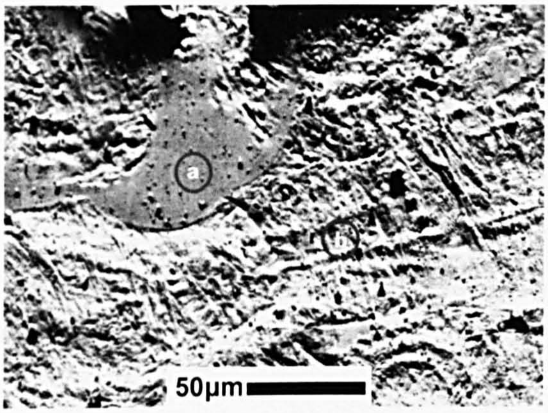

Figure 39 Selected areas of differing hardness for region specific EDX analysis.

In some regions, the porous sample appeared to be more resistant to polishing than the bulk material. This can be observed in Figure 39 in which preferential polishing can be observed.

The size of the smooth region is typical of feed stock powder sizes, which suggests the presence of contamination. To verify this, an EDX comparison of regions a) and b) was undertaken. The results of this can be seen in Figure 40 and Figure 41 respectively.

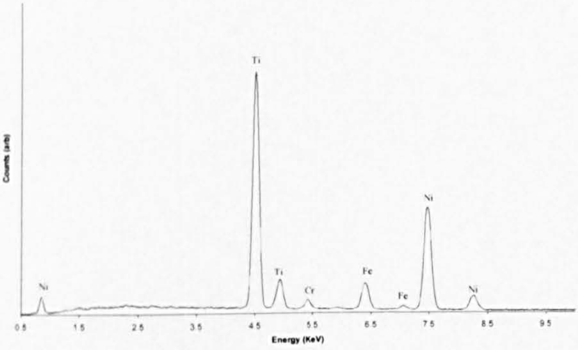

Figure 40 EDX spectra of region a) from Figure 39

Region a) is clearly heavily contaminated with Fe and Cr. The SLM is frequently used to process 316L stainless steel. Consequently the contaminant can be readily attributed to this material.

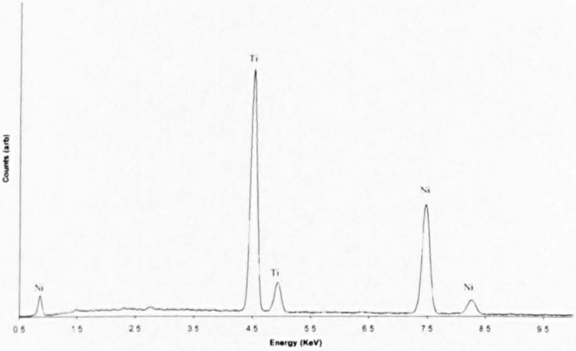

Figure 41 EDX spectra of region b) from Figure 39.

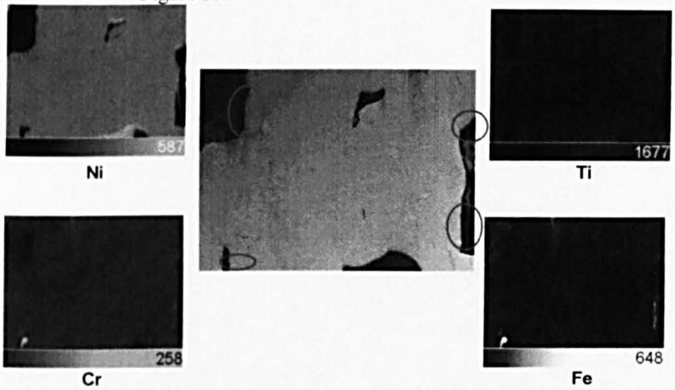

Figure 42 Elemental mapping of NiTi processed by SLM

The interface between region a) and the bulk material observed in Figure 39 is clearly defined and no diffusion is observed in this micrograph. This might be expected to occur around grain boundaries. However the texture introduced during phase transformation tends to obscure grain boundaries. The minimal diffusion and its effect on the bulk material was assessed using elemental mapping on a separate region (Figure 42). The regions rich in Fe and Cr are consistent with pore edges suggesting that segregation occurs between the bulk material and contaminant during melting. Elemental mapping also indicates that diffusion does not occur significantly.

Characterisation of Post Processed Material

DSC Analysis and comparison with feedstock

DSC of samples of the feedstock NiTi powder were compared to the solid SLM processed parts. This indicates that phase changes occur in both materials indicating the SME. Furthermore the transition temperatures fall within a similar range in both materials, Figure 43.

This observation demonstrates that NiTi material processed by the SLM process retains the phase change habit associated with the SME.

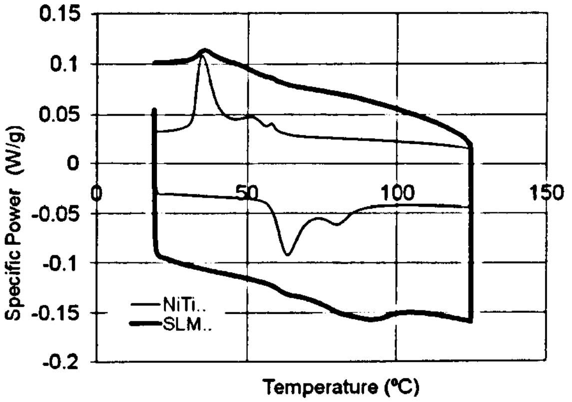

Figure 43 DSC of SLM processed material and feedstock powder.

The martensitic transition occurs between 32-58°C and the austenitic transition is observed from 90-58°C. The start and finish temperatures of both the austenitic (A_S and A_F) and martensitic (M_S and M_F) and phase changes in both powder and solid part correlate strongly. However, the phase transition in the powder is far more abrupt compared to solid part which spans a wider temperature range. This suggests that the phase transition in SLM NiTi parts is more gradual than those within conventionally processed parts. This may be due to unwanted phases introduced during SLM processing. One such possibility is an increased fraction of the R-phase. However, DSC peaks associated with this phase cannot be resolved from the martensitic transformation observed in the solid.

The R-phase is usually associated with Ni rich nitinols which have been subjected to thermal cycling in-service. Further analysis was conducted verify the presence of the R-phase.

The gradual transformation has potential advantages within the context of MEMs. An abrupt phase transition results in a similarly erratic deformation on the macroscopic form of an SMA component. This is manifested as two distinct physical forms corresponding to near 100% austenitic composition or near 100% martensitic composition unless temperature is maintained within a specific range of the phase change. Some MEMs applications, for example micro-thermal actuators for heat exchangers, may require more discrete intervals of actuation that could be possible with a SMA offering more gradual phase changes.

The gradual phase transition allows the net properties of the material to be more easily controlled. As temperature changes, the degree of each phase present can be adjusted smoothly and so can the net material properties. The extreme 100% martensitic phase is associated with ductile material properties. The extreme of 100% austenitic is associated with more brittle titanium-like qualities. The ability to control not just shape but also mechanical properties may be useful for various applications. If this property is combined with ohmic actuation, as examined later, it is possible to adjust material properties simply by adjusting the heating current.

TEM Analysis of Processed Structures

An uncontaminated section of processed material post build parameter set 4 was thinned mechanically and then ion milled to produce a suitable sample for TEM analysis.

The SAD pattern in Figure 44 was indexed and found to be consistent with the austenitic phase. As expected, the high temperature phase is observed.

Interaction with the electron beam causes a sufficient temperature rise to produce the phase change. The R-phase is not observed as expected.

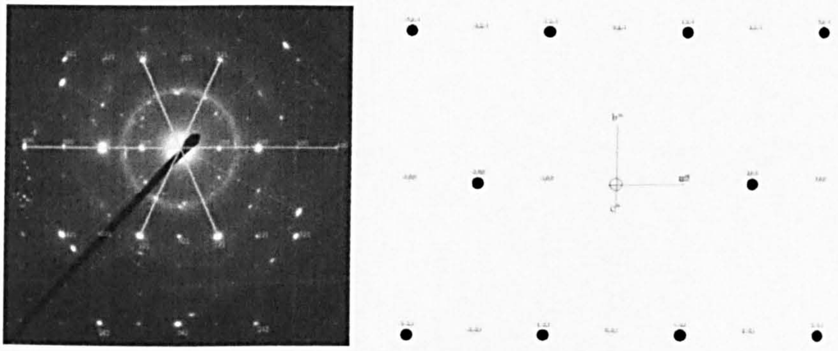

Figure 44 a) Selective area diffraction (SAD) pattern of NiTi processed by SLM b) reference pattern after Cuevas et al.

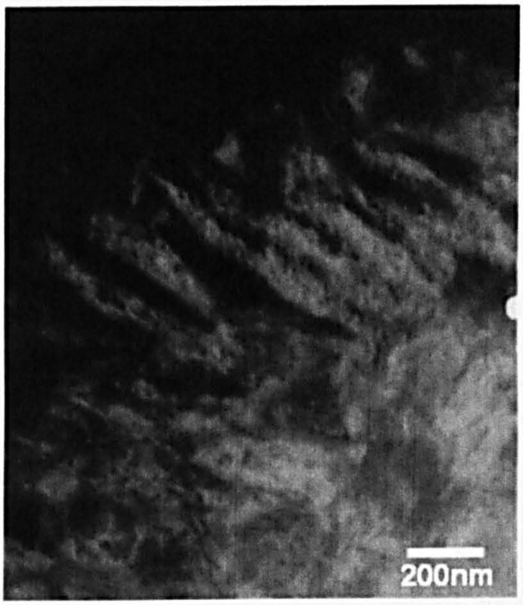

Figure 45 Dark field image corresponding to the diffraction pattern depicted in Figure 42

Kroger et al [139] have demonstrated that the martensitic and R-phase may coexist; however the austenitic and the R-phase may not. Their observations were made using cooled TEM sample holders. This facility was unavailable but presents an interesting investigation for future work to examine the extent and transition characteristics of SLM processed NiTi.

	Parameter	Reference	Experiment	Error
Angle between plane	-121/1-21	48.19°	47.92 °	-0.6%
	-121/-100	65.91°	66.35°	+0.7%
	-200/1-21	114.09°	114.48°	+0.3%
	3-21/-1-21	77.4°	76.91°	+0.6%
d-space ratio	-200:-100	0.500	0.493	-0.7%
	-300:-100	3	3.041	+1.4%
	-12-1:-200	0.816	0.809	-0.86%
	-22-1:-12-1	1.225	1.224	-0.08%

Table 5 Confirmation of NiTi lattice parameters.

The lattice parameters, as calculated by Cuevas et al [140], were used to generate a reference reciprocal lattice pattern. Selected angles between planes and d-spacing ratio measurements were made, and compared. Table 5 shows sample lattice parameters which verify this conclusion.

X-Ray Diffraction

The low transition temperatures of NiTi make them especially practical however, this property also makes evaluating their crystallography complex. Given the TEM observations above, XRD was undertaken to compare the feedstock and processed material. Figure 46 shows peaks introduced by SLM processing between 42° and 43.5°.

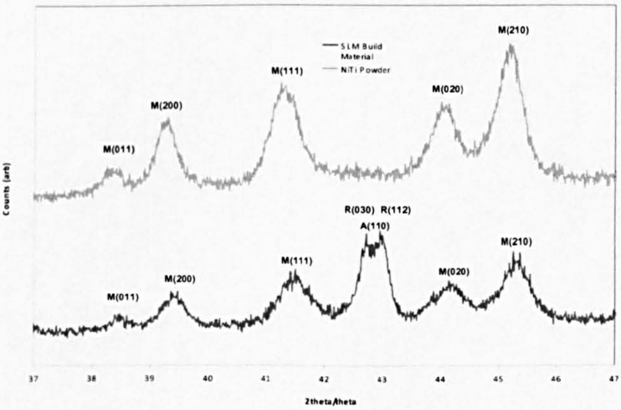

Figure 46 XRD of NiTi build material and feedstock powder

Based upon this data alone, it is impossible to unequivocally attribute these peaks to either the R-phase or the high temperature austenite. Temperature measurements made in the XRD apparatus indicate the temperature did not exceed the A_s temperature. Thus, the peak observed at 43.5° is unlikely to be austenite.

Comparing the data sets for feedstock and SLM material with reference data, (Figure 47 and Figure 48 respectively) does not clarify the matter. The peaks of interest in Figure 47 are not entirely consistent with the expected R-phase. It appears as though a doublet is due to the R(112) and the A(110). However, this is a forbidden combination [139]. It should also be noted, that the resolution of the XRD apparatus is 0.2° and so resolving each peak is difficult.

Some peak shift at low θ is also observed in Figure 48, which compares the feedstock material with the reference data.

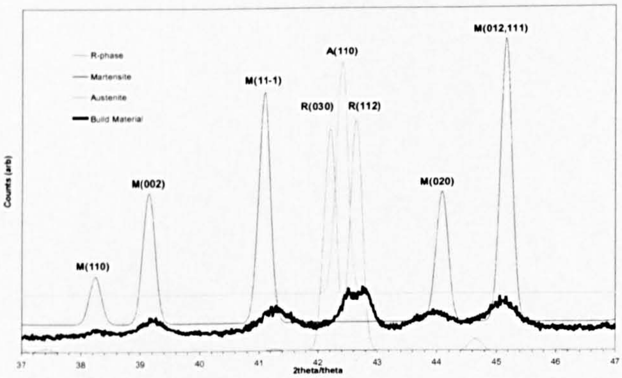

Figure 47 XRD of NiTi build material with reference peaks after Khalil-Allafi et al and Cuevas et al.

Considering the XRD patterns for all samples processed by SLM (Figure 49), then the peak/s of interest appear in all samples. However, their presence seems to be independent of the processing parameters used.

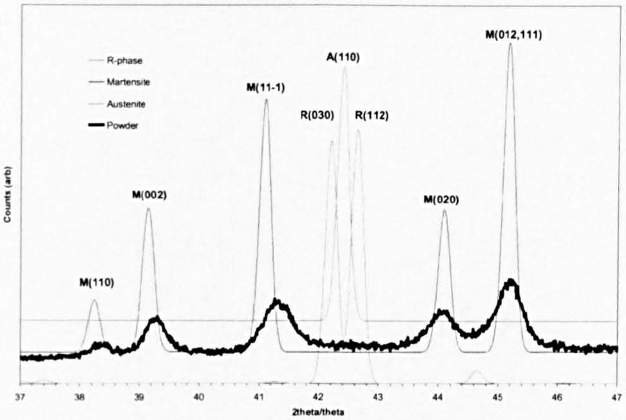

Figure 48 XRD of NiTi powder with reference peaks after Khalil-Allafi et al and Cuevas et al.

In the sample corresponding to condition 7 the doublet is most apparent, yet the peak is dominated by the R(112) however the relative intensity of the R(030) and R(112) in the library data is near equal. If the apparatus was unable to resolve the peaks then a widened peak would be expected which fell at 42.5° (bisecting both R-phase peaks).

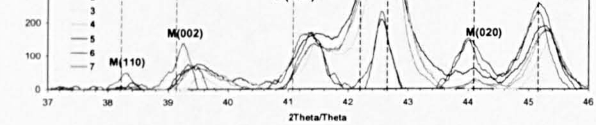

Figure 49 XRD spectra for many sample of NiTi processed by SLM

The matter is further complicated by the proximity of the R-phase peaks to the M(11-1) peak which appears adjacent to the region attributed to the R(030). It is likely that processing NiTi alloys in this way results in the introduction of the R-phase or at least maintaining this phase if it is present in the powder feedstock.

It should be noted that the cementite diffraction peak for iron falls at 42.25°. However, the contribution of any contaminant to peak intensities would likely be minimal. Assuming contamination level is insignificant.

This notion is substantiated if the relative diffraction intensities are considered. The area enclosed by the R(030) and R(112) reflections is much larger than that of the M(11-1) and M(012,111) suggesting that convolution has occurred between the R-phase peaks. It is proposed that the R-phase may be introduced as a result of the rapid heating/cooling regimes involved in laser melting and/or the subsequent heating as adjacent laser tracks are processed. If the R-phase is retained from the powdered condition this is likely due to the non-melting of the R-phase rich core discussed earlier in this chapter.

Shape Memory Training and Functionality

One-Way Training of Shape memory springs

Many reductive manufacturing techniques capable of producing micro-scale features cannot produce complex 3D geometries. To demonstrate the geometrical advantages of using LBMTs, a series of helical springs were built from the NiTi feedstock as shown in Figure 50. The springs were then one-way trained by compressing them at room temperature (Figure 50a), followed by heating with a hot air gun above the transformation temperature (Figure 50b). This process was repeated twenty to thirty times. Once trained, the springs showed between 60 to 80% extension beyond the compressed length between the austenitic starting (A_s) and finishing (A_f) temperatures of 58° and 90°C respectively.

The strain recovery of the deformed springs in this experiment can be calculated using the equation for the shear strain in a helical spring [141];

$$\gamma = \frac{d(L-L_0)}{\pi D^2 n} \tag{4.1}$$

In which, d, refers to the wire diameter, L and L_0, signify the strained and unstrained wire lengths. D is the mean diameter of the spring and, n, refers to the number of active coils.

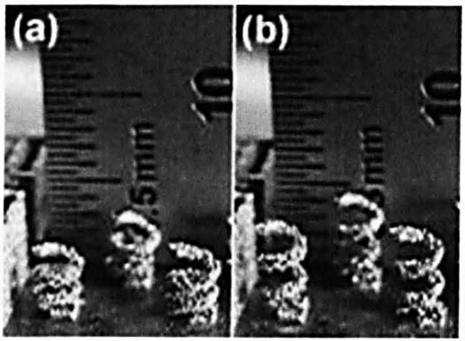

Figure 50 Shape memory springs manufactured by SLM.

Parameter	Value
d	0.5±0.1mm
Mean $L-L_0$	3±0.25mm
D	2±0.25mm
n	2.5

Table 6 Dimensions of NiTi springs processed by SLM.

Applying this equation to the geometry of the solid models used for this calculation reveals a strain of 6%. However, it should be noted that the CAD is now an approximation to the finished component. From Figure 50 it is apparent that the springs have non-uniform cross sections and a surface roughness which represents a significant fraction of the spring girth. This affects the true strain exhibited by the spring. The surface roughness of the springs will cause the onset of stress concentrations so localised strain recovery may indeed be much higher. Improvements to the build process may result in better surface finishes.

Ohmic Actuation and two-way shape memory effect

The ability to ohmically actuate NiTi components is highly desirable. Developments within SLM and 2.5D technologies will allow direct fixing of NiTi components onto engineering substrates. This will enable the design of components for new applications which may include valves, controlling micro-fluidic flow or perhaps paddles used to agitate or homogenize fluid samples.

To demonstrate this type of actuation a series of 'U' shaped or 'hairpin' cantilever beams were built as shown in Figure 51. The cantilevers were then two-way trained via the SME method using a manual jig to ensure that loading was uniform along the length of the beam. The beams were first cooled below the martensitic finish temperature to ensure that the following deformation was conducted with the cantilever in a fully martensitic state. The cantilever was then deformed again using the manual jig and heated above the martensitic finish temperature at which point the beam returned to the original form. This was repeated 20 to 30 times until the cantilever exhibited the two-way SME.

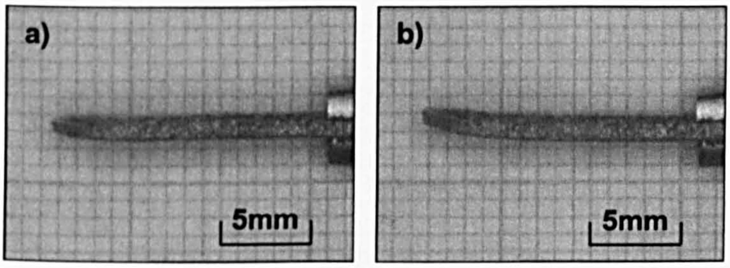

Figure 51 'U' shaped cantilevers manufactured by SLM.

The trained cantilevers were then mounted and an electrical current was passed through the structures to demonstrate current heating actuation of the two-way SME. By adjusting electrical current supplied with intermittent periods of forced convection cooling it was possible adjust the form of the cantilevers.

The resistivity of SLM processed parts can be estimated given the dimensions of the cantilever and the magnitude of the electrical signal required causing the temperature change corresponding to the completion of the austenitic phase (100°C, Figure 43). The nitinol alloy SE508 ($Ni_{55.8}Ti_{44.2}$) as supplied by NDC exhibits a resistivity in the martensitic phase of 82 x $10^{-8}\Omega$.m. The manufactured SLM components exhibit a resistivity of similar magnitude ~80 x $10^{-8}\Omega$.m. The accuracy of this measurement is influenced by two factors. Firstly, the tolerances of these parts is currently limited to ± 0.1 mm. Secondly, although these parts are near 100% dense, inclusions will contribute to increasing the resistance substantially of these components. The advent of SLM apparatus capable of smaller spot sizes will no doubt improve tolerances and reduce the minimum overall dimensions achievable. These components were not subjected to post SLM treatments (polishing, machining, hot isostatic pressing etc). Further refinement of build parameters will result in 100% dense parts. The heating currents required for these components are clearly much higher than would be required for MEM equivalent systems in which milliamps would be required for thin film actuation.

Two problems arise from the homogeneity of the component. Areas of differing densities will transform at different stages. This results in localised regions of increased SME through the two-way training process. Although, the components were indeed deformed uniformly, ensuring an even stress distribution along the beam, after two-way training the well documented super elastic effect [9] is more obvious in some regions compared to others. However, assuming strain is evenly distributed throughout the phase transition (i.e. the two-way effect is consistent throughout material) the net maximum strain endured can be determined to be 10.7%. This is consistent with conventionally produced NiTi components (SE508 datasheet) ≈ 10% and depends upon heat treatments and conditions of operation. This strain was obtained by evaluating the radius of curvature of the beam and assuming the usual strain distribution through the beam. This is an approximation because it does not account for the change in cross section at the tip of the beam and resultant change in second moment of area. This effect is negligible with respect to the length of beam and so can be disregarded for the purposes of this approximation.

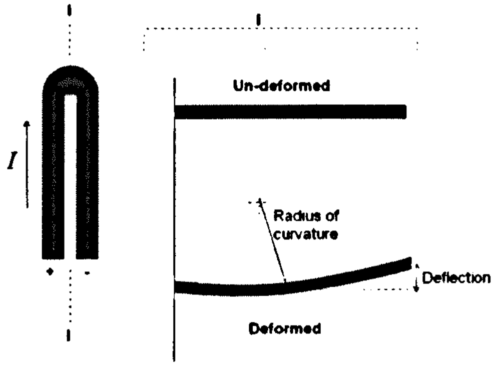

Figure 52 Evaluation of strain in NiTi 'U' shape cantilevers.

The extent of this deflection would be ample for inclusion in novel capacitance based sensor systems for example. The deflection of a NiTi plate within a capacitor in response to a temperature change can easily be measured as a variation in capacitance. The more gradual phase change response displayed by SLM processed NiTi parts makes them more suited to this application given their more graded response to temperature change.

Conclusions

The selective laser melting process has been applied to the manufacture of NiTi shape memory alloys. Increasing the laser dwell time tends to increase the density of built components. The dimensions of feature sizes are determined by the laser beam size, laser power, exposure time and powder property. The X-ray diffraction pattern of SLM processed materials suggests that the process maintains if not induces the R-phase in the alloy. R-phase may be apparent in NiTi powders due to coring effects.

The extent of the R-phase in the SLM processed material varied with laser power although not monotonically suggesting that other parameters such as the cooling rate exert some influence. The cooling rate is dependent upon the size and shape of the SLM part. Generally the R-phase content tends to increase with laser power.

The selective laser melting process has been applied to the manufacture of cantilever beams and helical springs which have been two-way trained and one-way trained respectively. The dimensions of feature sizes and build quality are determined by the laser beam size, laser power, exposure time and powder properties.

NiTi cantilever beams produced by this method have been successfully two-way trained. It is therefore for possible to produce NiTi components in this way which will exploit the design freedoms of LBMTs however maintain the shape memory effect.

5. Processing of Piezoelectric Materials

Introduction

Engineering applications which exploit piezoelectric materials are ever broadening. These applications may include complex components which must be integrated with a wide variety of substrate materials. Some applications require non-planar substrates such as conformal sensors. It is proposed that layer based manufacturing techniques are well suited to this purpose.

Based on preliminary investigations two routes to layer based manufacture of piezoelectric materials were selected. This chapter describes the processing of the ceramic material $BaTiO_3$ with selective laser sintering and secondly the manufacture of $BaTiO_3$-polymer composites using the digital light processing technique. To yield piezoelectric properties, these materials must be subjected to a poling procedure. This may be deemed to be a significant disadvantage compared to some materials which display spontaneous piezoelectric properties.

Consequently further research was undertaken to assess the use of alternative material systems e.g. PVDF-TrFE. Unlike the ceramic materials the co-polymer can be spontaneously piezoelectric and enhanced poling can be induced by mechanical straining the material.

It is shown in this chapter that by processing these materials using layer based manufacturing techniques selective deposition can be achieved and material properties conserved. Deposition is also undertaken on silicon with the aim of demonstrating the flexibilities of this approach.

Characterisation of Feedstock Materials

Particle Size Analysis

$BaTiO_3$ was supplied in powder form from Strem Chemicals, (99%; m.p. 1620°C; density 5.58 g/cm^3). Particle size analysis was undertaken to evaluate the maximum potential packing density and examine flowability.

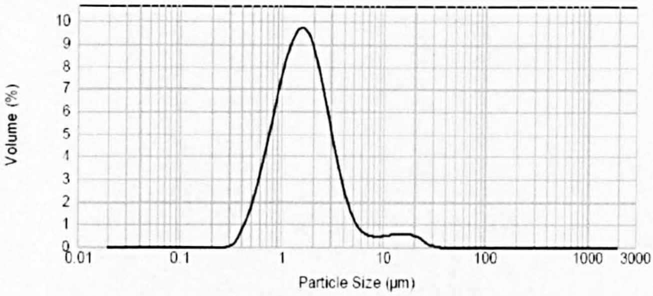

Figure 53 $BaTiO_3$ feedstock particle size analysis.

Figure 53 reveals that the powder has a mean particle size of 1.75μm and standard deviation of 0.65μm. This is far finer than powders which are typically used in SLM/SLS. At this scale electrostatic forces become dominant and agglomeration can occur. Agglomeration prevents the powder from flowing to form an even powder bed. This hampered direct use of the powder using the recoater mechanism in the SLM apparatus. However, alternative modes of deposition and processing have been investigated.

Sintering $BaTiO_3$ on silicon substrates was of significant interest due to the possible incorporation into 'lab-on-a-chip' technologies. It was proposed that this could be achieved by spin coating the ceramic in a conventional photo resist before patterning. Forming a powder bed in this way would allow for selective consolidation with precision laser sintering. Effectively this would be a single layer process resulting in piezoelectric pads bonded to a silicon wafer.

Piezoelectric composites were also investigated which combined $BaTiO_3$ and the piezoelectric polymer matrix PVDF-TrFE. Another composite was prepared with a photosensitive acrylate for use with DLP apparatus. The combination and poling of $BaTiO_3$ with similar matrices [142] has been achieved elsewhere however they have not been processed by layer based techniques with photo-curing polymers.

$BaTiO_3$ Powder XRD

Figure 54 confirms that the $BaTiO_3$ as supplied by Strem Chemicals is consistent with the piezoelectric tetragonal phase.

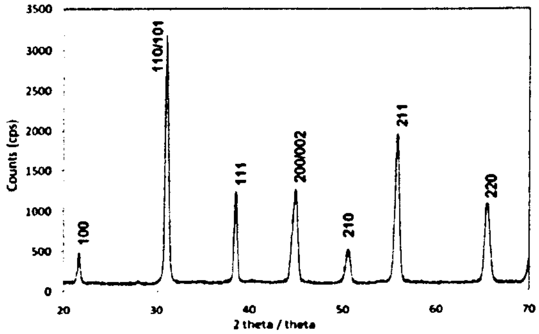

Figure 54 XRD of $BaTiO_3$ powder indexed to the cubic lattice.

Matrix Materials

Initial experiments were undertaken using both the piezoelectric co-polymer PVDF-TrFE supplied by Piezotech (France) and a photosensitive PMMA 'R5' supplied by EnvisionTec for use with their DLP apparatus.

The first polymer was of initial interest as reports indicate [87] that a piezoelectric matrix combined with piezoelectric filler would yield a higher d_{33} value. Consequently, samples were prepared which consisted of varying proportions of $BaTiO_3$ and PVDF-TrFE according to Table 7.

These samples were prepared by dissolving the PVDF-TrFE in the solvent dimethylfluro-ethylene (DMF) before homogenisation with $BaTiO_3$

powder. The slurry was then readily mouldable as shown in Figure 55a) and Figure 55b).

Sample #	PVDF-TrFE (%)	$BaTiO_3$ (%)	Ratio of $BaTiO_3$:PVDF-TrFE	Thickness (mm)	d_{33} (±0.05pC/N)	Capacitance (±0.05pF)
1	15.75	64.25	4.079	0.144	0.31	18.4
2	18.89	56.11	3.446	0.157	0.184	11.95
3	23.44	39.06	1.666	0.126	0.1	11.19
4	23.72	24.98	1.053	0.215	0.165	12.42

Table 7 $BaTiO_3$/PVDF-TrFE preliminary samples

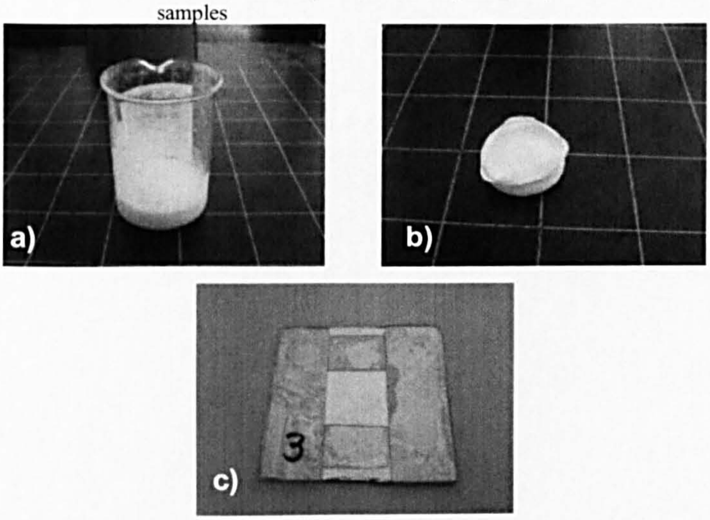

Figure 55 $BaTiO_3$/PVDF-TrFE preliminary samples.

Thick film samples of each mixture were caste on glass slides. These were allowed to solidify and then subjected to electrical measurements including d_{33} as shown in Table 7.

For these compositions the most significant d_{33} contribution in the unpoled samples will be made by the PVDF-TrFE fraction. This is due to localised β phase regions emerging as the mixture solidified. The $BaTiO_3$ makes no significant contribution in the unpoled condition. This can clearly be seen in Figure 55.

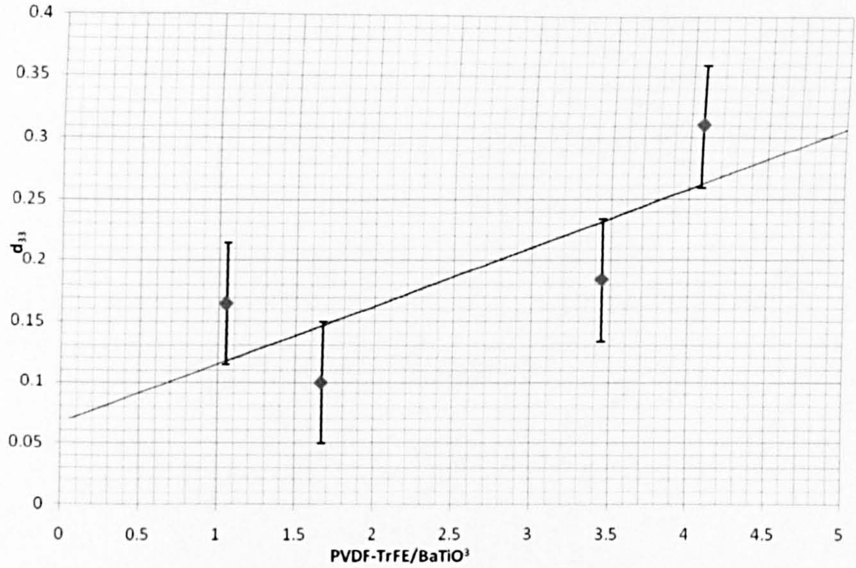

Figure 56 A mulivariant linear regression indicating the dominant contribution to d_{33} of PVDF-TrFE in unpoled polymer/ceramics.

No attempt to pole these samples was made. Obtaining a 3D shape was considered of primary importance as piezoelectric functionality could be guaranteed by conventional manufacturing techniques. Clearly by creating moulds and filling with the liquid slurry does not present a significant manufacturing development.

An alternative matrix material was selected which was compatible with the DLP process. R5, a PMMA, was also blended with the $BaTiO_3$ powder and experiments were undertaken to identify suitable build parameters which resulted in high aspect ratio solid geometries. These parameters relate to exposure time and peeling rate to ensure a successful build.

Based on preliminary investigations two routes to layer based manufacture of piezoelectric materials were selected and are detailed below.

Laser Processing

Ceramic Consolidation

Sintering is regularly performed to consolidate ceramic piezoelectric materials. However, this process involves compaction in the 'green' stage which limits the shapes that can be achieved.

The laser power output of most SLM platforms provides more than sufficient thermal energy to cause sintering in $BaTiO_3$. Unfortunately the flowability of the fine ceramic powder was poor which meant that powder beds of this material were not uniform and layer by layer deposition could not be investigated.

One solution to this problem is to prepare a powder bed before sintering. This involves depositing a thin layer of powder (0.1-1mm) in a metal tray and rastering the laser over the bed. This method is often used when evaluating a parameter window for new materials in SLM/SLS apparatus, but it does not allow for layer-based manufacture.

$BaTiO_3$ has been spin coated and patterned as part of other processes elsewhere [45]. This was suggested as a possible hybrid approach to result in selective sintering.

To evaluate this, the following experiment was made. $BaTiO_3$ was blended with a conventional photolithography photo-resist (Shipley, no. 1828). These were then ultrasonically homogenised and then spin coated on wafers of 100mm diameter. Spin coating at varying speeds was investigated to result in a uniform deposition which was later to be patterned. Figure 57 shows the result of spinning the photo resist with $BaTiO_3$. From this figure it is apparent the thickness, and hence maximum incorporation of ceramic powder in the spin coated ceramic-polymer is at a maximum when the formula is 75% (by weight) $BaTiO_3$ to photo-resist.

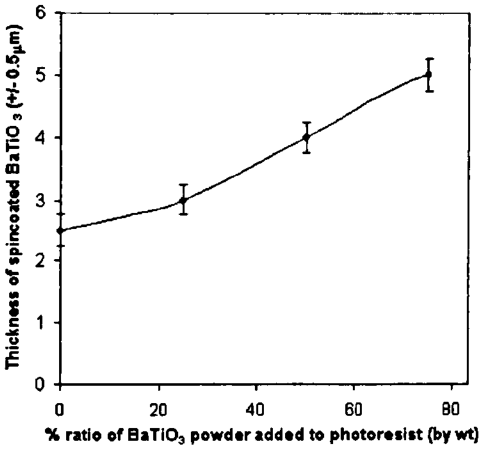

Figure 57 Spin coating of BaTiO$_3$/polymer composites.

Films with a relative weight content higher than 75% lacked homogeneity in the spin coated layer. Radial streaks in the resist, aggregation of powder clumps on the wafer surface and uneven thickness became more apparent as the relative weight of the powder increased. The optimum speed of the spin cycle was determined to be around 4000 rpm for the 75% ratio of BaTiO$_3$ to photo-resist, slower spin speeds in the range 2000-3000 rpm produced uneven, less homogeneous spin coated layers. Spin speeds higher than 4000 rpm were not feasible using the spin coating unit available for this experiment. The maximum loading was required to ensure that sintered layers would exhibit a high d_{33}.

Simple patterning was then carried out to investigate if the ceramic could be removed and the resolution of a lithographic technique maintained. The standard stereo lithographic process (soft bake, exposure time and hard bake times) for the photo-resist was completed as per the manufacturer's specification.

Samples of the spin coated and patterned composite were then investigated using SEM to compare the relative efficacy of the deposition technique with neat polymer. Figure 58 clearly shows that the composite has been cleanly removed in a similar manner as the neat photo-resist.

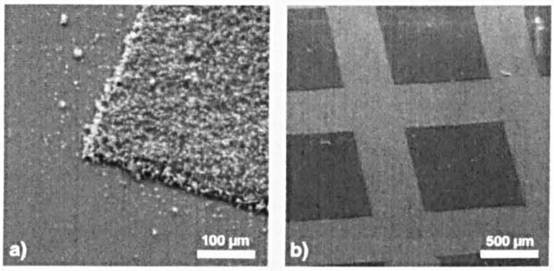

Figure 58 a) stereo lithography of $BaTiO_3$/photo-resist composite and b) neat photo-resist (Hitachi).

This method represents a suitable pre-process after which consolidation can follow. It was proposed that a patterned wafer could be consolidated / sintered by the SLM/SLS process.

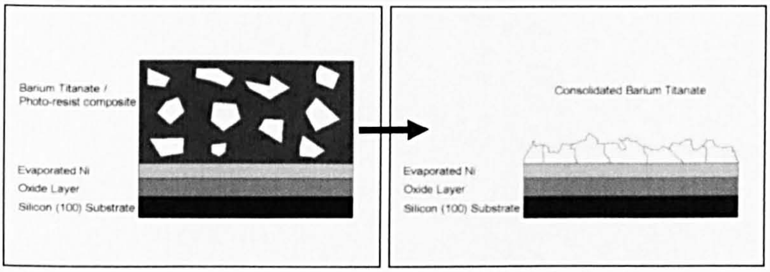

Figure 59 Laser processing of $BaTiO_3$/Photo-resist composites on silicon.

Whilst sufficient energy must be provided to the $BaTiO_3$ to cause sintering and simultaneous ablation of the polymer resist, the laser interaction should not cause damage to layers below. This is a prime concern if this approach is to be feasible.

Silicon Wafer Preparation

A silicon wafer 'platform' was processed using conventional clean room photolithography techniques, namely: Si(100) wafers with a thermally grown SiO_2 insulating layer were metallised with a thin film of Ni evaporated under vacuum to form a bottom electrode. This approach is typical for silicon components for 'lab-on-a-chip' technologies. The added advantage of metallisation is that it provides an added thermal reflection layer so reducing the risk of thermal gradients causing cracking in the layers below.

The wafers were spin-coated using a ramped process consisting of 30s at 2000rpm followed by 90s at 4000rpm. The feed rate used was by flooding the wafer with 10ml of slurry before spinning. The wafers were then 'soft baked' at 120°C for 90s, and patterned onto the Si (100) wafer with a 20 second UV (λ = 293nm) lithographic exposure and developed. The protected Ni film was then patterned using a 7:3 HNO_3/H_2O wet etch. The ceramic-polymer thin film was then hard baked at 140°C for 5 minutes. The resulting uniform thickness of the $BaTiO_3$-polymer was measured by SEM cross section micro-analysis and characterised by EDX and XRD analysis.

Evolution of Build Parameters

Laser processing of the spin coated $BaTiO_3$ thin films was performed using SLS. The sintering process was performed in an argon ambient with less than 0.2% O_2, considered a safe operating condition. The presence of O_2 during sintering has been shown to reduce elemental dissemination elsewhere[143].

The processed wafers were then located precisely in the build chamber of the SLM apparatus and a datum was obtained from a cleaved edge. This permitted accurate alignment so the laser would raster over the correct region of the composite layer. The control software was programmed to "write" small discs with a diameter of 5mm in patterned regions of the $BaTiO_3$ composite film to demonstrate alignment. Laser powers ranging from 75kW/cm^2 to 160kW/cm^2 were used, while the laser dwell time and spot size were kept constant at 600 μs and 80μm respectively. In a preliminary test varying the dwell time had an insignificant effect on the laser sintering of a powder bed over the range of laser powers used, indicating that the required threshold energy densities to cause sintering were not achieved.

Samples were selected and cleaved to reveal a brittle fracture cross section. These were then analysed using SEM and EDX.

Larger consolidated discs were also prepared for XRD analysis. This technique was only applied to the upper most surface of the discs. It is expected that compositional variation occurred both parallel and perpendicular to the 'build' direction.

Figure 60 shows a series of SEM cross sectional images through all layers of the samples showing the influence of laser power. It can be seen that laser power densities below 75kW/cm^2 have little effect in sintering of the $BaTiO_3$ particles or ablation of the photo-resist. Although some densification of $BaTiO_3$ particles is observed in the upper layer it is incomplete. This may be caused by some melting and subsequent shrinkage in the composite matrix

Laser power densities in the region of 85-100kW/cm^2 yielded the most homogeneous sintered microstructures with some large spherical clumps, but no apparent degradation to the thin nickel bottom electrode (Figure 60b). These clumps are indicative that some sintering had occurred as they are larger in diameter than the feedstock powder.

Laser powers of 150kW/cm^2 or above tended to damage or ablate large regions of the spin coated ceramic powder from the surface of the Ni, which is clearly seen in Figure 60d. This observation demonstrates that the required energy density has been exceeded and degradation of the substrate has occurred. The high temperatures required to sinter $BaTiO_3$ and the relatively low thermal tolerance of the other materials present requires a balance. This results in a narrow operating window which consolidates but also produces the uniform layer desired.

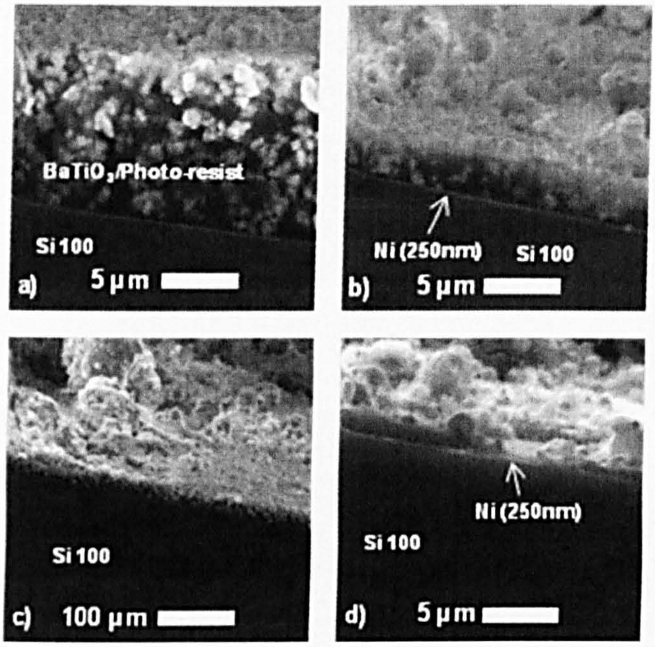

Figure 60 Varying laser power consolidation of $BaTiO_3$/Photo-resist composites a) 75kW/cm^2, b/c) 94kW/cm^2 and d) 156kW/cm^2 (Hitachi).

The sintered pads were not mechanically tested, however the ceramic layer conserved mechanical integrity throughout analysis and material loss was not apparent during this phase. A high degree of adherence to the substrate is essential as some mechanical actuation would be required in typical applications for this material.

To evaluate whether the laser processing had caused any significant compositional changes EDX measurements were made on the most promising of the cross sections (Figure 61).

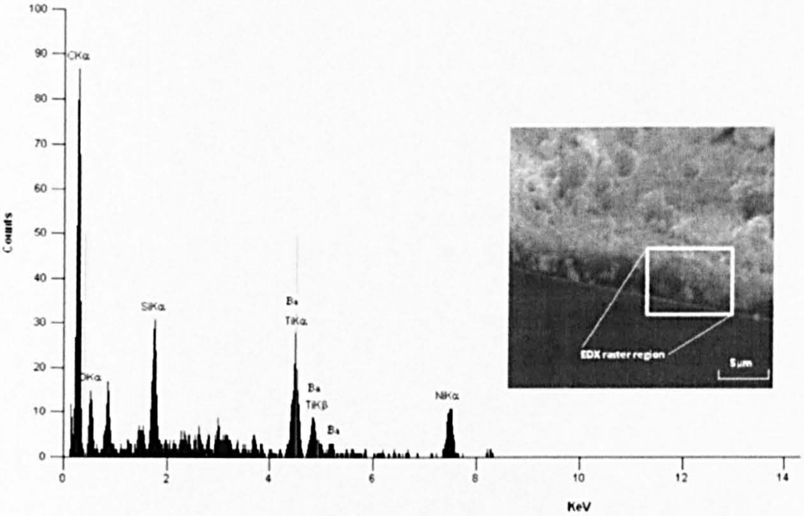

Figure 61 EDX analysis of composite laser processed at $88kW/cm^2$ (Hitachi).

An analysis of a cross-sectional region of the SLS processed $BaTiO_3$ spin coated powder beds revealed no significant variation from the composition expected. Ba, Ti and O constituents are clearly apparent. This would suggest any undesirable SLS laser induced modifications of the spin coated piezoelectric ceramic material are low at the laser powers used in this study. X-ray peaks were observed for the Si(100) substrate at 1.8keV and for the Ni metallization layer (7.5KeV). The Ba and Ti peaks at 4.465keV and 4.508 keV cannot be distinguished individually due to the inherent limited energy resolution of the EDX technique. These two close peaks would be separated by use of higher resolution techniques such as Wavelength Dispersive X-ray microanalysis (WDX).

This observation suggests that the process is suitable for processing $BaTiO_3$ as chemical composition is maintained. However, of equal importance is the crystal structure after consolidation.

Raman and XRD

After SLS processing the resulting films showed visible signs of discolouration suggesting some compositional degradation of the original white feedstock material. Although not unequivocal, this is most likely the result of the ablation of the photo-resist leaving residual carbon. However, the X-ray diffraction data shown in Figure 62 indicates that the sinter processing does not significantly degrade the bulk composition or phase of the spin coated ceramic material. The diffraction pattern of the sintered material shows the characteristic (100), (110), (111), (200), (210) and (211) features of $BaTiO_3$ powder.

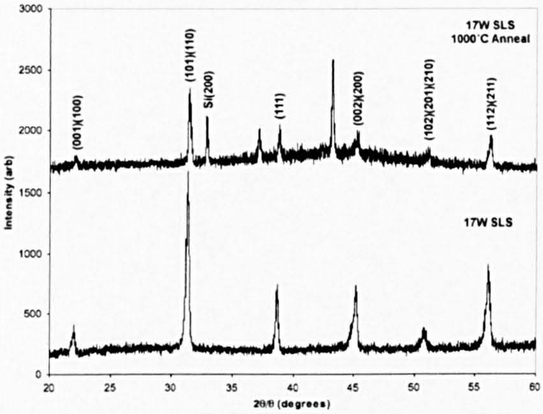

Figure 62 XRD analysis of composite layer pre and post annealing at a power density of 75 kW/cm^2 (17W).

Subsequent annealing of the ceramic films at 1000^{o}C for 1 hour in air restored the white colour of the films but the XRD θ -2θ features from the barium titanate showed no change. The appearance of the peaks at 2θ of 37^o and 43^o are related to the presence of NiO in the annealed films which indicates an undesirable oxidation of the bottom electrode contact. These observations appear to indicate that the discolouration arises from some surface reduction or degradation of the powder particles and that post annealing can reverse the process.

Annealing was repeated for three samples from the most promising laser power range, Figure 62. All three annealing processes returned the $BaTiO_3$ to its initial white colour. Annealing is not geometry limiting, but ideally it would be avoided. Any poling regime to which the material was subjected would likely require an elevation in temperature in excess of 130°C. The formation of NiO only occurred in regions not covered by the ceramic pads and as such may not present a problem. This issue may be overcome if further etches had been done to remove the Ni in unwanted areas. The substrate is unlikely to be effected by this process as SiO_2 is thermally stable at 1000°C.

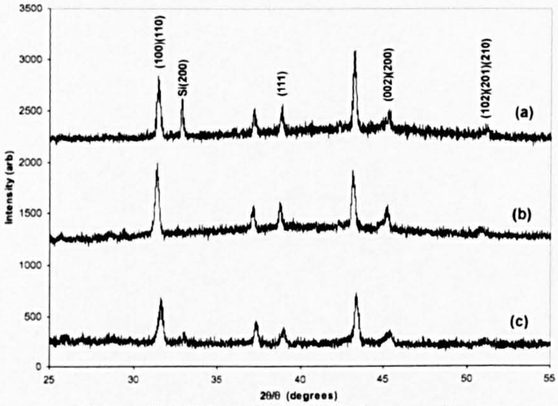

Figure 63 XRD analysis of SLS composites later annealed at 1000°C for 1 hour. Post laser powers of a)75kW/cm^2, b)88kW/cm^2 and c)114kW/cm^2.

The apparent Si peaks observed in Figure 62 are due to the cleaved edges exposed to the X-ray beam. There may also be regions exposed to the X-rays through the build layer as Figure 60d confirms that the layer is not uniform. This is likely to be due to local regions in the spin coating which are thin and heating causes them to become detached. Also the application of thermal energy by laser allows specific regions to be sintered however there will be variation through the laser cross section in terms of energy intensity. This effect causes a difference in the amount of heating which takes place as observed at the 'track' on the substrate. This may cause local overheating and reheating where tracks overlap.

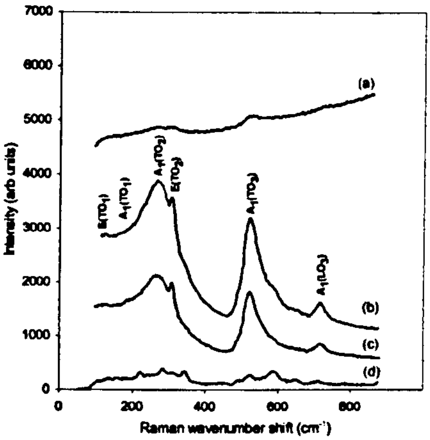

Figure 64 Raman spectra showing (a) the as-spun composite and the annealed $BaTiO_3$ pads post laser powers of (b) 75kW/cm^2; (c) 88kW/cm^2; and (d) 114kW/cm^2.

Figure 64 shows the Raman spectra of the $BaTiO_3$/resist composites in the as-spun film (a) which exhibits a large fluorescent background arising from the polymer matrix and weak peak intensities which can be attributed to the A_1 and E modes of the room temperature P4mm phase [144]. After selective laser sintering of the spun film and subsequent annealing at 1000°C the polymer matrix is effectively burnt out leaving the crystalline $BaTiO_3$ layer. The $A_1(TO_2)$, $E(TO_2)$, $A_1(TO_3)$ and $A_1(LO_3)$ modes were observed at 270, 308, 525 and 725 cm^{-1} respectively. The asymmetric $A_1(TO_3)$ mode couples weakly with the $A_1(TO_2)$ mode and the phonon wave vector directions are randomly distributed with respect to the crystallographic axes in ceramics. This allows mode mixing and quasi-phonon modes in the spectrum. The influence of increasing the sintering laser power combined with post - annealing appears to be a reduction in the grain size.

The resulting confinement of phonons in small grain materials leads to the breakdown of long-range order, activating phonons away from the centre of the Brillouin zone (k ~ 0) and resulting in broadening and wave number shifts of the Raman modes. At laser power densities of 114kW/cm^2 and above, the resulting films loose most of the characteristics of the feedstock $BaTiO_3$ powder and show some interactions with the underlying oxidized nickel have resulted. These observations indicate that only a limited range of laser powers is feasible for the formation of sintered barium titanate films from pre-positioned spin coated barium titanate-polymer composite films.

These preliminary results suggest the potential for applying selective laser sintering in the manufacture of electro-ceramic films on silicon substrates. As SLS is a 'direct-write' process it has the capability of rapid-prototyping of complex structures without the need for lithographic masks and techniques.

Process Limitations

The tests conducted on $BaTiO_3$/Photo-resist composite films suggest that this process is a viable approach to deposit piezoelectric ceramics and more broadly ceramic materials to silicon substrates.

Poling and piezoelectric characterisation was not made using these samples; however it could be undertaken by depositing a further metallic layer to the top surface of the pads. This would provide spaced, parallel conductive plates over which an electric field could be applied to cause dipole alignment.

Poling of similar $BaTiO_3$ films manufactured by the sol gel process has been reported elsewhere [39]. However, direct deposition by spin coating and laser consolidation to a pre-defined pattern has been achieved here for the first time.

It is proposed that other polymer matrix/ceramics could be processed in a similar manner which may have wider processing windows. Substrates other than Ni coated silicon may also be selected which exhibit a more uniform interface between structural and functional layers.

A high loading of ceramic powder is required. This ensures that powder particles may be touching and more likely to adhere. However, this limits the flowability of the slurry and hence the layer quality when spun onto the substrate.

DLP Processing of Barium Titanate

Evolution of Build Parameters

Compatible material systems are limited for the DLP process. Unlike SLA which is a more mature technology, vendors are not the exclusive material providers for their machines. Material development is driven by the demands of the RP market which are usually for tougher, higher temperature resistant and cheaper materials.

There are currently no piezoelectric materials available to users of DLP or SLA apparatus. This would present a significant development as 'freeform' components with piezoelectric properties would be highly desirable.

Development of an entirely polymeric system would require the development of a resin that not only contained photo inhibitors/initiators but would cure to give a piezoelectric polymer.

Recently, some materials have been released for use with EnvisionTec systems which do contain nano ceramic fillers. Known as 'Nanocure' these materials are more tactile and present better thermal properties [145] than other materials available. This provides a precedent for the inclusion of piezoelectric ceramics in materials compatible with the DLP process. This would allow the manufacture of bulk polymer/piezoelectric composites with the advantage of free form design.

Mixing a ceramic material with the photo-polymer presents several difficulties with respect to processing approved feed stocks. Firstly the filler material has distinct optical properties with respect to the resin. This will cause 'shading' (Figure 65) if the filler material is not entirely transparent to the curing radiation. In reality the filler material will scatter, absorb and transmit the incident radiation. Thus less light will penetrate to the bottom of each build layer potentially causing under exposure and poor interlayer adhesion.

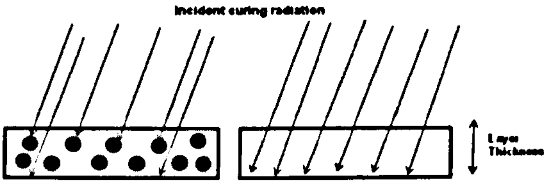

Figure 65 'Shading' caused by particulates within photo-curable resins.

The reduced transmission of light through a build may be mitigated by increasing the intensity of the incident light, increasing exposure time or reducing layer thickness. Increasing the exposure of the matrix material is undesirable as the upper most regions will overexpose causing embrittlement and flakiness. Processing parameters are usually designed to minimise the exposure differential through a layer and with previous layers optimising the adherence between consecutive build layers.

Secondly the nature of the DLP process requires that the filler material remains in suspension throughout the duration of the build procedure. If the filler is excessively dense then it may sink to the bottom of the basement and the composition of the resulting composite will vary through the height of the build. For the purposes of this work a homogeneous composition would be desirable throughout the build height.

Thirdly the loading of piezoelectric material must be maximised to increase the possibility of connectivity between adjacent ceramic particles.

Based on the material properties of the matrix and filler, the piezoelectric response of the bulk material can be estimated. This requires assumptions to be made but never the less will give an indication of how such materials should perform.

Predicted Piezoelectric Response

Chan et al propose a simple model to predict the performance of 1-3 polymer/ceramic composites [146]. In this model, the piezoelectric constituent is geometrically aligned in one direction and surrounded on all sides by a non piezoelectric matrix. This model can be used to predict the performance of the composites used in this study.

To apply this model the following assumptions must be made; the strain experienced by the polymer is equal to that experienced by the ceramic, electric fields produced by the filler particles are all aligned, post processing results in ideal poling and the stress induced in the composite can be averaged according to equation 5.1.

$$\bar{\sigma} = f\sigma_c + (1-f)\sigma_p \tag{5.1}$$

Where σ_c, and σ_p refer to the stress on ceramic and polymer elements of the composite and f refers to the volume fraction of ceramic. These assumptions are bold given the disparity between Young's moduli and hence compliance between resin and particles.

The mean piezoelectric modulus of the composite, d_{33}, can be calculated from the following formula [142], in which subscripts refer to the directions indicated in Table 8;

$$\bar{d}_{33} = \frac{f c_{11}^{p} d_{33}^{c}}{c(v)} \tag{5.2}$$

Where S(*f*), the compliance of the composite is defined as;

$$c(f) = fc_{11}^{p} + (1-f)c_{33}^{c} \tag{5.3}$$

When values listed in Table 8 are substituted into equations 5.2 and 5.3 the performance of piezoelectric polymers manufactured by DLP as a function of ceramic content can be predicted, Figure 66.

Property	$BaTiO_3$	R5-Photopolymer
Piezoelectric constant (d_{33})	85pC/N	0pC/N
Compliance c_{33},c_{11})	$15.7 \times 10^{-12} m^2/N$	$662.2 \times 10^{-12} m^2/N$

Table 8 Material properties used in piezoelectric response model based upon Etech tests (chap 6).

This model shows that for a relatively low volume fraction of ceramic composite mean d_{33} values are comparable to bulk $BaTiO_3$. This is largely due to the low modulus (high compliance) of the R5 material. But this situation makes no allowance for stress variations about the ceramic filler particles.

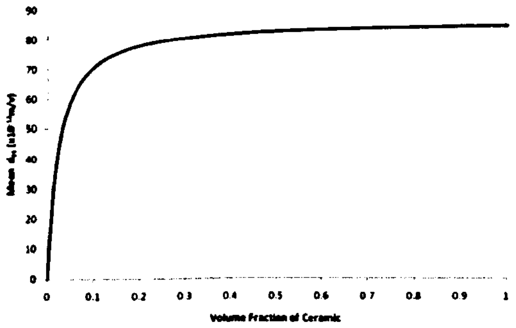

Figure 66 Predicted d_{33} response of DLP $BaTiO_3$/polymer composites.

The accuracy of this model is limited. However, Chan et al report errors in comparison to experimentally obtained data of less than 10%. The araldite/PZT composite they used is more conducive to the model because the difference between moduli is smaller. That is to say the strain transfer in this situation will be much poorer and actual composite performance would reveal much lower d_{33} values.

From equation 5.2 it is apparent that S(ν) must be minimised to result in an increased d_{33} for the overall composite. This presents an interesting issue for polymer selection. Currently there are only a few resins available for DLP but if possible for piezoelectric composite applications the compliance should be minimised so that it approximates more closely the compliance of the more rigid ceramic filler.

The trend observed in Figure 66 can be subjected to a reduction factor based on a typical strain transfer ratio for ceramic/polymer composites. Bowen et al [147] have presented a model which deals with 3-3 piezoelectric composites in which orientation of the filler may vary. This assumes that there is linkage between particles in the field direction but not necessarily transverse to this. This gives rise to a more 'unit cell' like approach to which finite element analysis can be applied.

If a cross section through a sample is assumed to be typical and $BaTiO_3$ particles are assumed to be circular with a diameter of 1.75μm (Figure 53) then a ratio can obtained between compliance and thus the fraction of load endured by each constituent can be found;

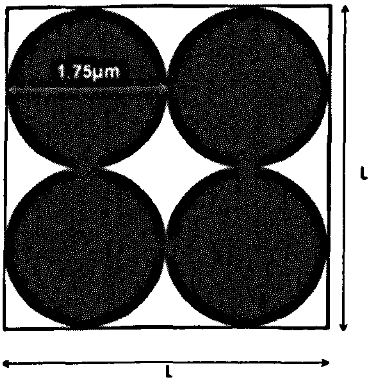

Figure 67 An 'ideal' slice through a piezo/polymer composite.

If the total number of piezoelectric particles in the cross section is taken to be, n, then the area of piezoelectric (A_P) and matrix (A_M) material can be given as follows;

$$A_P = 0.766n\pi \times 10^{-12} \tag{5.4}$$

$$A_M = L^2 - (0.766n\pi \times 10^{-12}) \tag{5.5}$$

Thus a more accurate mean d_{33} can be obtained by using the above to estimate the fraction of the load on the composite bourn by the piezoelectric constituent.

$$\bar{d}_{33} = d_{33}^{BaTiO_3} \cdot \left(\frac{\dfrac{0.766n\pi \times 10^{-12}}{c_{33}^{BaTiO_3}}}{\dfrac{L^2 - (0.766n\pi \times 10^{-12})}{c_{33}^{Matrix}} + \dfrac{0.766n\pi \times 10^{-12}}{c_{33}^{BaTiO_3}}} \right) \tag{5.6}$$

This is applied to give Figure 68. It is clear that the greater the $BaTiO_3$ content the higher the mean d_{33} of the composite. In reality these composites may not display perfect linkage between ceramic particles in the field direction. This will serve to further diminish the mean d_{33}. This effect will decrease as v increases as probability of linkage will also increase. This model is used to predict performance of composite cross sections detailed later.

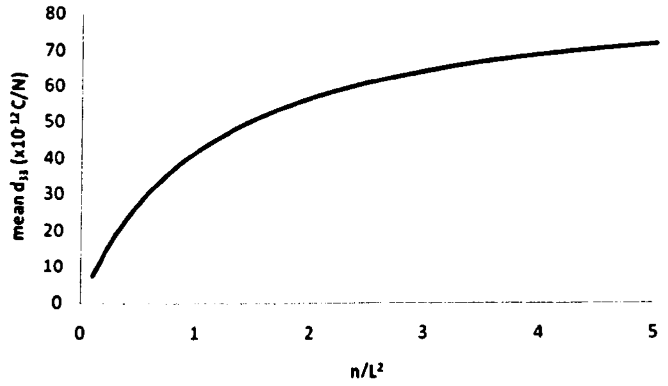

Figure 68 Predicted piezoelectric response based upon ceramic particulates in composite cross section.

Compositional Variation

Given the predicted performance of the R5/$BaTiO_3$ composites, build tests with DLP apparatus were undertaken. Varying compositions were tested, by adding specific amounts of $BaTiO_3$ to photo polymer before mixing. Each composition required customised build parameters to achieve acceptable parts i.e. cured cuboids (1x10x10mm) that could survive cleaning and secondary curing. Cleaning was achieved by ultrasonically bathing the components in isopropanol at room temperature.

Similarly to the on silicon scenario the content of $BaTiO_3$ was maximised. However, the limiting factor in this case was the observed viscosity of the mixture. Over loading the resin resulted in an overly viscous material that was shown to cure on exposure to daylight but would not flow sufficiently to finish a build process.

These composites were then subjected to brittle fracture perpendicular to the build direction, the results of which can be seen in Figure 69. Starting with the lowest $BaTiO_3$ content, a), the ceramic content is low and powder dispersion is poor. $BaTiO_3$ is clearly observed as the bright areas where charge is accumulating despite gold coating. Striations are observed in all samples as a product of brittle fracture and indicate steps in individual build layers. This is typical of DLP polymer failure modes which will be examined further in Chapter 6.

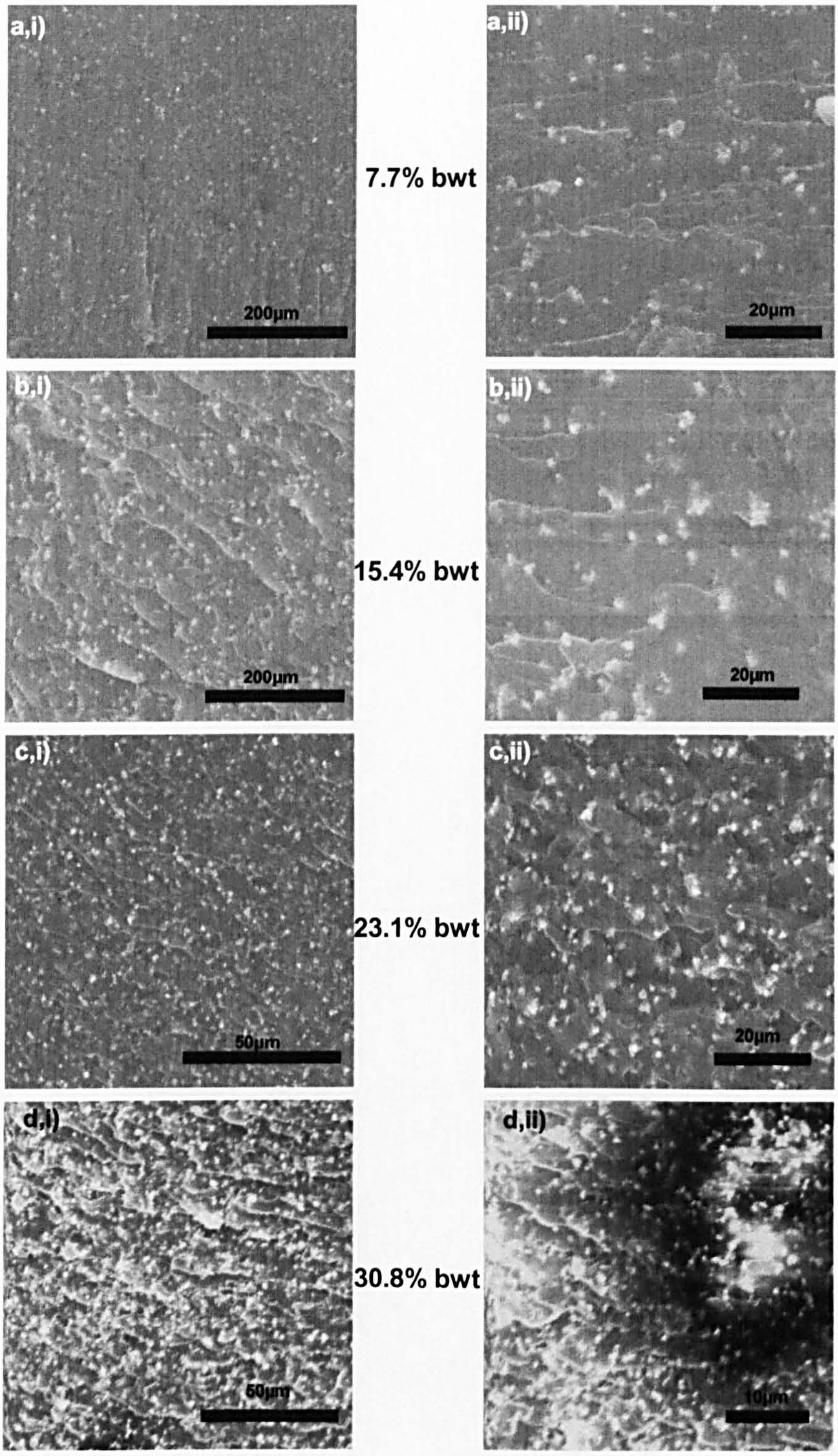

Figure 69 SEM of varying compositions of R5/$BaTiO_3$ composites (Hitachi).

Based on the distribution of powder particles in Figure 69, the Bowen model can be used to predict the associated d_{33} value assuming perfect linkage between cross sections. The predicted values are given in Table 9.

Ceramic by Weight (%)	Ceramic by Volume (%)	Mean Particles/100μm^2	Mean d_{33} (pC/N)
7.7	1.7	0.7	34.3
15.4	3.7	1.5	50.8
23.1	6	2.5	61
30.8	9	3.75	67.9

Table 9 Predicted piezoelectric response based on the particle distribution observed in Figure 69

Sample d) shows a $BaTiO_3$ content that would be more likely to yield predictable piezoelectric properties as linkage is more prevalent. However, it is expected that the strength of the material is likely to be significantly affected by higher filler content.

To completely pole these composites an electric field should be applied at a temperature in excess of 130°C, the Curie temperature of $BaTiO_3$. This places a further demand upon the polymer matrix, which must be able to maintain dimensional integrity at this temperature. Furthermore such field strengths are in excess of that required to cause breakdown in air at s.t.p. To prevent breakdown poling is normally conducted under oil which has a significantly higher permittivity than air.

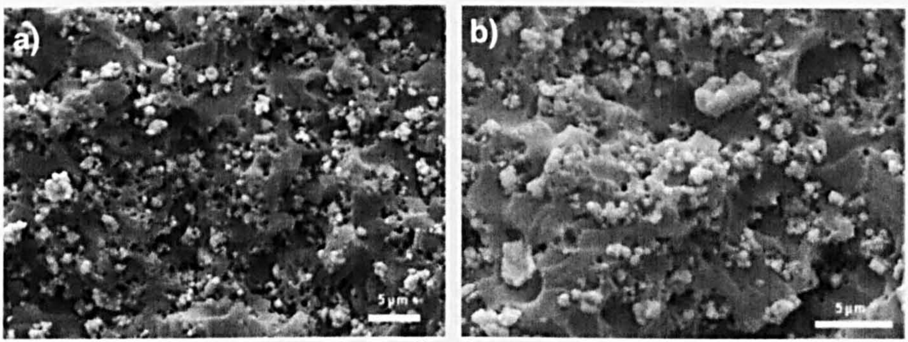

Figure 70 Tensile fracture surface of $BaTiO_3$/R5 composite (Jeol).

Should a maximum poling condition be achievable the theory in the previous section predicts that an R5/$BaTiO_3$ composite containing 30.8% by weight $BaTiO_3$ might produce a d_{33} of 67.9pC/N.

Further fracture surface analysis of sample d) from Figure 69 was undertaken to investigate the adherence between matrix and ceramic filler. These are shown in Figure 70.

From the protruding filler particles and the craters left from 'pull out', it is evident that the filler adheres to the resin. This can be clearly seen in Figure 70b) in which filler particles and similar sized craters are in close proximity. Had the cohesion not been good then the ceramic particles would not populate the fracture surface.

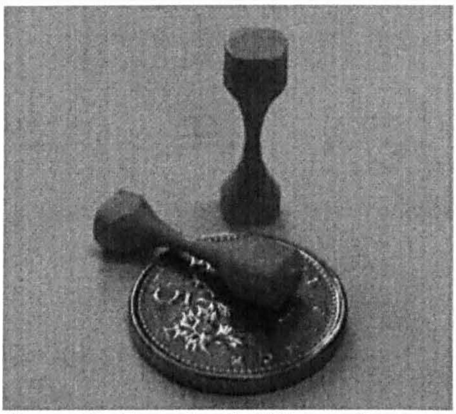

Figure 71 Exemplar $BaTiO_3$ tensile test specimens.

To measure the mechanical properties of these composites, small tensile test specimens were constructed. The design of the tensile test samples can be seen in Figure 71. This also demonstrates that such composites processes by DLP will display good fidelity to the design intent.

Process Limitations

High aspect ratio specimen parts have been built using the DLP methodology however; they have not been functionalised by poling.

The design and manufacture process flow has been demonstrated to be appropriate but advancements to the manufacturing process must be made to result in functional piezoelectric components.

Poling in a layer-wise manner is one way in which this may be achieved. For this to be made possible significant changes must be made to the DLP apparatus to include a poling step.

It is also apparent that while DLP processed the composite successfully the part finish was lacking with respect to purpose made resin feedstocks. It is expected that finer grained $BaTiO_3$ filler particles may improve this effect. Such finer particles would be more likely to remain in suspension during the build process. However this was not an issue in this case.

Conclusions

The selective laser sintering process has been investigated as a method for the fabrication of electroceramic thin films on silicon substrates. Methods of forming pre-positioned layers of barium titanate have been investigated by spin-coating the feedstock powder mixed with a commercial polymer photo-resist.

Attempts were made to develop a piezoelectric ceramic / piezoelectric polymer layer based material. The material shown to exhibit the piezoelectric effect but was incompatible with the manufacturing apparatus available. Although standalone it presents no advantage with regard to LBMTs, it is possible to provide custom moulds manufactured by LBMTs which could be used to mould such composites.

The ceramic-photoresist composite was deposited directly onto a silicon substrate pre-oxidised to form an electrically insulating layer. A nickel film was deposited before deposition of the ceramic - polymer layer which served to promote adhesion and uniformity during the spin-coating process. A range of laser power processing conditions were identified in which barium titanate layers could be consolidated. The microstructure of barium titanate films is sensitive to the SLS laser processing conditions, with the optimum laser powers for the processing of the $BaTiO_3$-polymer found to be around 85-100kW/cm^2. Selective laser sintering powers above 150kW/cm^2 tended to ablate areas of the film resulting in undesirable cracks and holes. Although these materials were not tested directly for piezoelectric properties, materials analysis indicates that the correct phases are present for the material to exhibit piezoelectric response.

Mixtures of the DLP photopolymer R5 have been blended with $BaTiO_3$ and their performance as piezoelectric composites predicted. Polymer matrix piezoelectric materials present advantages over their neat ceramic counterparts in that they present a higher likelihood for biocompatibility.

6. Digital Light Processing

Introduction

DLP has the potential to deliver custom engineering components to a high tolerance. Structural components are unlikely to be realised with DLP due to the poor mechanical properties of the currently available materials. However, it is proposed that components for some electrical devices can be manufactured with this technique. The use of DLP presents a cost effective way of realising parts that would be costly and often impossible to produce through conventional CAD/CAM routes.

One such electrical application which requires bespoke components is quadrupole mass spectrometry. These spectrometers use electrical fields to produce, filter, and collect ions allowing mass analysis. Ion paths in these devices are governed by the precise electrical fields which are determined by the physical geometry of the electrodes. Thus the performance of such devices is highly dependent upon electrode geometries and precision assembly.

The polymer materials available for use with DLP are not conductive and must be coated to operate as electrodes. This chapter firstly investigates the material properties, failure mechanics and resolution of the DLP process. The DLP process has been applied to a prototype mass spectrometer application to produce various components and their viability is examined.

Of particular interest is the mass filter section which requires custom spacing, profiles and lengths which are easily modified using this design and manufacture approach.

Properties of Components Built by DLP

Mechanical Properties

Tensile tests were conducted on 'dog bone' test parts manufactured by DLP in orientations perpendicular to the build direction (Figure 72). Tests were also conducted on samples built parallel to the build direction; however failure was almost always recorded away from the required zone in tensile test pieces.

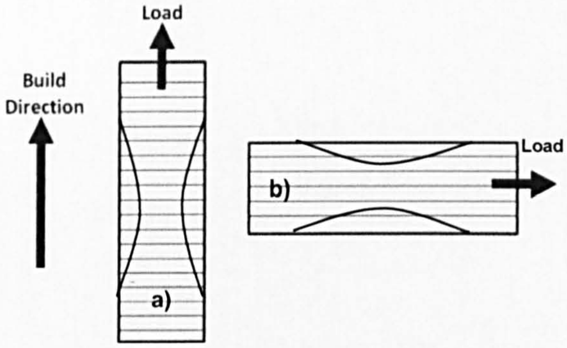

Figure 72 Build orientation of tensile test specimens with respect to layers. a) parallel b) perpendicular

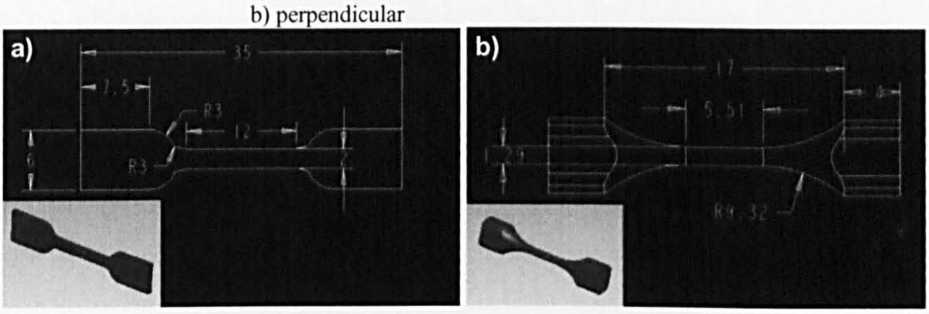

Figure 73 The development of tensile test specimens for small envelope DLP parts a) modified after BS EN ISO 527-2 [148] b) a customised design.

The limited size of the build envelope (20.03 x 27.77mm) meant that tensile test structure based on standards for tensile testing for polymers could not be satisfied. Therefore a design which was effectively a miniaturised version of BS EN ISO 527-2 was initially used. This test regularly failed at the shoulder and not in the desired middle gauge section. This was counteracted by increasing the chamfer at the shoulder in a customised design.

Tensile tests conducted on R5 resin processed by DLP are compared with those properties listed by the manufacturer in Table 11. For these tests the recommended parameter set was used for R5 as 25µm layer thickness. The manufacturer does not account for variation in build orientation when applied to the DLP manufacturing process nor is pre test treatment such as secondary curing taken into account. It is expected that a significant loss of mechanical properties will occur as the R5 ages in sunlight. This is not addressed in ASTM 638M as quoted in [88].

Parameter	25µm Layers	50µm Layers	100µm Layers
Burn in range exposure time (ms)	7000	10000	12500
Standard range exposure time (ms)	3000	4500	6500
Projector Brightness (mW/dm^2)	530-580	530-580	530-580

Table 10 Typical build parameters for processing the R5 feedstock. The parameters used in this study are labelled in red.

The parameters detailed in Table 10 have been used to plot a linear relationship between layer thickness and exposure time. This allows a semi continuous parameter set forming the basis of 'adaptive slicing'. This permits the development of varying layer thicknesses through part height.

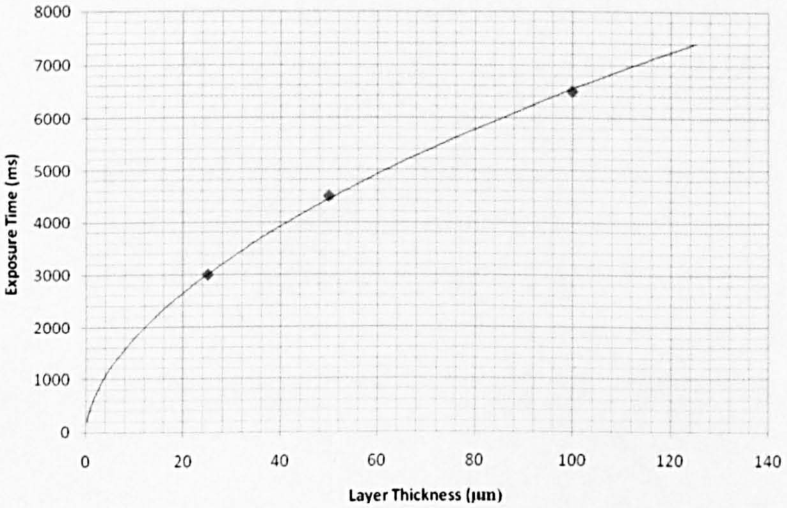

Figure 74 The linear relationship between exposure time and build layer thickness.

Investigations based on processed R5 showed a significant difference in tensile strength between build orientations. However, a greater concern is the variation within the same sample type. The small size of the test specimens is likely to contribute to this variation. This also indicates that random errors may be responsible for failure and that mechanical performance cannot be accurately predicted. Causes of these random errors may include faults within build layers or foreign bodies which cause stress concentrations and premature failure.

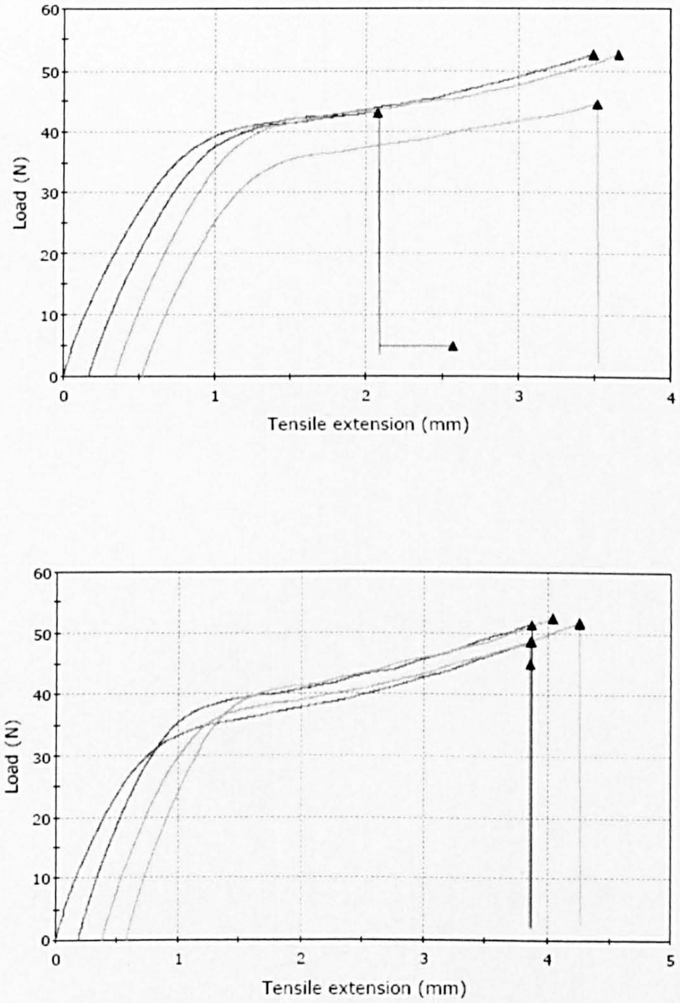

Figure 75 Typical load-extension curves for R5 tensile test samples according to ISO 527-2. Summarised in Table 11.

Test Method	Description	Result (mean)
ASTM 638M	Tensile Strength	31-39 MPa
ISO 527-2		27 MPa
Custom		36.2 MPa
ASTM 638M	Elongation at Break	11-25 %
ISO 527-2		17%
Custom		40 %
ASTM 638M	Elongation at Yield	16 %
ISO 527-2		5%
Custom		8%
ASTM 638M	Modulus of Elasticity	1,245-1,510 MPa
ISO 527-2		347 MPa
Custom		404 MPa

Table 11 Tensile test results performed on DLP specimens. ASTM tests as performed by Envisiontec [145]

This is typical with parts manufactured by LBMTs. Variation in material properties are also widely reported in SLS/SLM. This may arise from several factors including location on substrate (in all directions within the same build) and variation between builds. If these processes are to gain wide spread acceptance, the reliability of parts manufactured by these techniques must be improved significantly.

Failure Mechanics

Selected, failed tensile test specimens were gold coated and later subjected to microscopic analysis. These fracture surfaces can be observed in Figure 76.

Figure 76a shows a DLP rod (built at 25µm layer thickness, ERM mode off) which has failed across an individual build layer interface. The groove between two build layers acts like a notch and results in a stress concentration. It is also likely that cross linking within build layers will be greater than cross linking between layers making the 'join' weaker. On exposure of an individual build layer the degree of cross linkage can be thought of as uniform through the layer cross section. This weakness cannot be compensated for during the build process as further exposure will cause embrittlement and poorer adhesion between build layers.

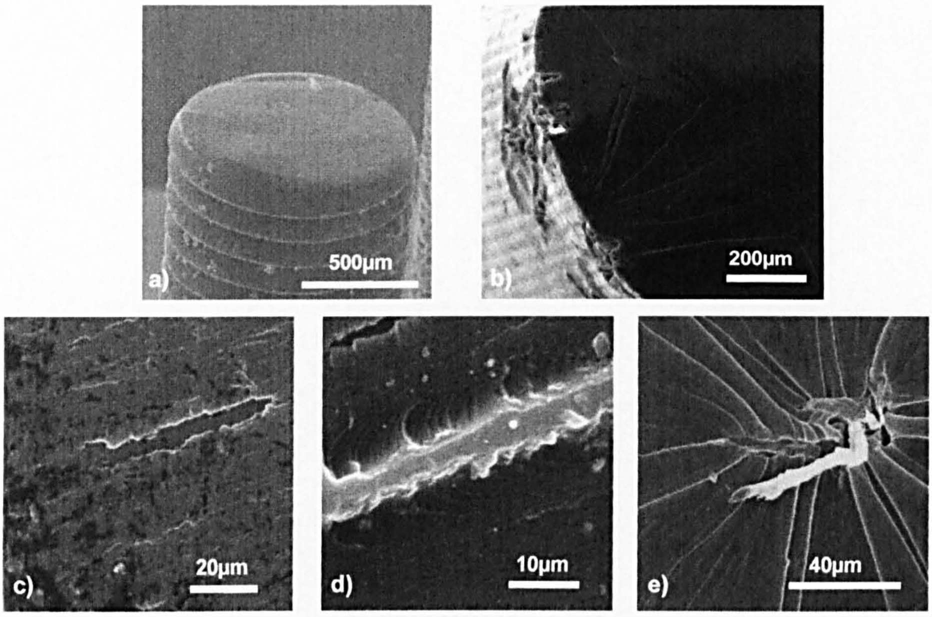

Figure 76 Assorted images of failure observed in DLP tensile test pieces (Hitachi).

Figure 76b shows failure perpendicular to the build direction in a tensile test specimen of 50µm layer thickness with ERM mode on. The chevron features observed here indicate the point of initiation of the failure. The staircase effect can be clearly observed around circumference of the specimen. It is frequently observed in specimens with greater layer thicknesses that failure is not limited to individual build layers but some peeling occurs between layers. The striations observed in this figure are boundaries between exposed layers. The failure appears to emanate from a surface defect. This may have been introduced in the cleaning stage post build.

Figure 76c and d show the failure between two layers in more detail. 'Islands' of the uppermost layer remain bonded to the layer below while the rest of the layer has been removed. This is likely due to localised regions in which cross linking between adjacent layers has been especially high.

Figure 76e shows a detail of a fracture propagation point within the centre of a tensile test piece. This is undoubtedly a foreign body (possible a remnant from a previous build) which has become lodged within the build during exposure and become partially free during the tensile test. Crack/tear lines are clearly seen to emanate from the point which would exhibit the highest stress concentrations.

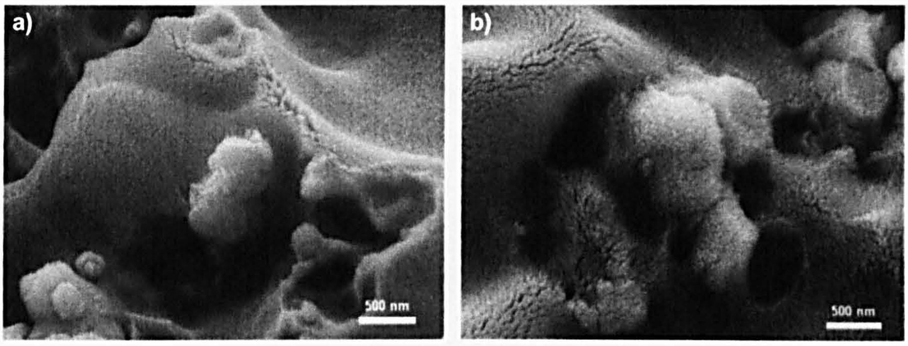

Figure 77 Fibril formation in R5 fracture surfaces (Jeol).

Fracture surfaces underwent further analysis Figure 77. At this magnification the formation of fibrils can be clearly observed. These are bunches of polymer chains which have been stretched before finally failing and remain as fibre like structures upon the fracture surface.

Such surfaces are commonly observed in bulk PMMA tensile test failures and are also responsible for crazing. Crazing is observed in polymers which are not tested to failure. It occurs when the so-called fibrils are stretched and a plastic strain is induced.

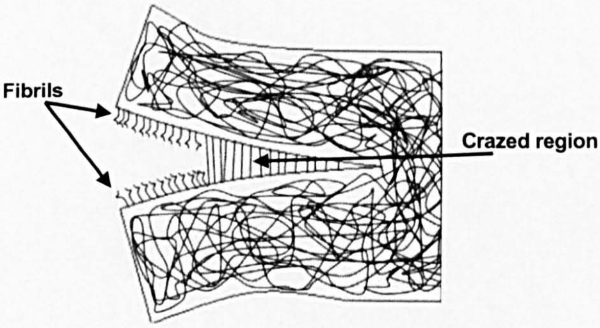

Figure 78 Crazing and fibril formation in PMMA polymers [81]

This strain can be observed in transparent polymers as a hazing. The hazing effect is caused by variations in refractive index as the fibrils vary in density in the strained region Figure 78.

Surface Roughness Analysis

The surface roughness of parts manufactured by LBMTs varies depending on how the surface is orientated relative to the build direction. In DLP the top and bottom surfaces are defined by the surface roughness of the base (at the bottom) and the glass substrate at the top, Figure 17. These are smoother than the side faces which will suffer from the ‘staircase’ effect.

Surface roughness is an important parameter to evaluate for DLP components which will be used in mass filter/electrode applications as the electric field from electrodes will be better if surface roughness is minimised, Figure 79.

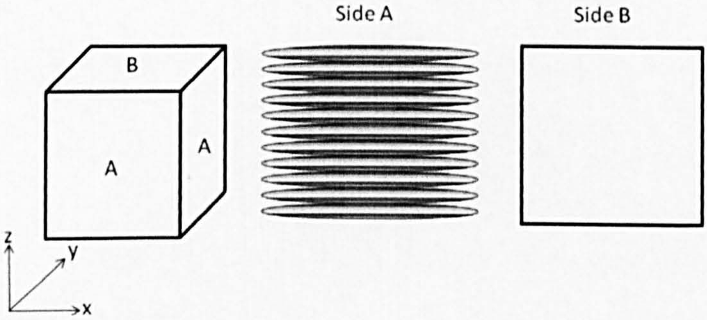

Figure 79 Variation in surface roughness for a simple cube by LBMTs (side A in z-x plane, side b in x-y plane).

White light interferometry was used to evaluate the surface roughness of DLP parts. Some scope exists within the DLP parameter set to adjust the build layer thickness and also to employ the enhanced resolution mode (ERM). The ERM causes two exposures per build layer to occur. Software splits the exposure time in half. The images for each exposure are dithered by one voxels width. This should result in a better approximation to the design intent and thus a smoother surface (*see* page 56).

Specimen Type	Measurement	Mean value	Standard Deviation
50µm (ERM on)	R_a	577nm	
	R_q	703nm	
	R_z	3.35µm	
	R_t	3.48µm	
50µm (ERM off)	R_a	716nm	
	R_q	891.66nm	
	R_z	6.16µm	
	R_t	7.23µm	
25µm (ERM on)	R_a	434nm	
	R_q	541nm	
	R_z	4.2µm	
	R_t	4.4µm	
25µm (ERM off)	R_a	749nm	
	R_q	895nm	
	R_z	3.97µm	
	R_t	4.18µm	

Table 12 Surface roughness of DLP planar faces.

To verify this effect and to evaluate surface roughness, four specimens were prepared according to, Table 12. The roughness values have their usual designation (R_a=arithmetic average, R_q=root mean squared, R_z=mean peak to valley and R_t=maximum peak to valley).

In order to understand the effect of the ERM, 3D maps from the corresponding samples were prepared, Figure 80. The difference between the two settings is evident.

In Figure 80a) and b) the apparent 'troughs' between consecutive voxel blocks is significantly lower than for when ERM mode is switched off (Figure 80c and d). Clearly a different texture is observed in the first two images. This is likely to be caused by changes in the polymerisation process as the second exposure occurs. Individual voxels are still discernable but their adhesion at the surface appears to be much better. It is likely from this evidence that specimens prepared in this way would display a higher tensile strength due to fewer crack propagation points, other factors remaining constant.

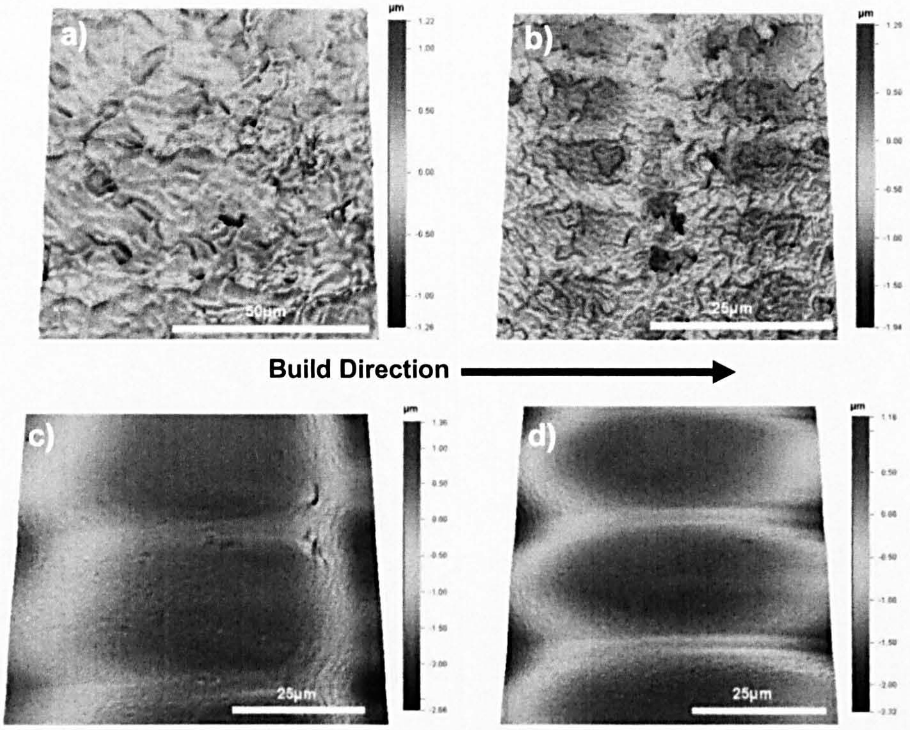

Figure 80 Surface profiles of DLP planar surfaces a)50µm (ERM on) b)25µm (ERM on) c)25µm (ERM off) d)50µm (ERM off).(Wyko)

Figure 80c) and d) show clearly the dimple shapes of individual voxels. The size of these dimples is consistent with the layer thickness selected to build them. This analysis also permits an approximation for the size of voxels using this apparatus. From measurements over an array of voxels in this plane there dimensions are given as 15µm x 15µm x 50µm and 15µm x 15µm x 25µm for each corresponding layer thickness. The activation of ERM mode comes with a time penalty which occurs because twice as many layer exposures must be completed. Builds with ERM mode activated will usually take around 30% longer.

DLP Resolution Testing

Evaluation of the smallest feature size that could be built using the DLP apparatus was made. All tests were conducted at the manufacturers advised parameter set at 25µm layer thickness with ERM on. Figure 81 shows the result of reducing wall thickness. All of the walls display a thickness error of ±7.5μm (the half width of a voxel). At approximately 50μm, the walls are no longer intact and begin to fail. This trend increases until little or no wall survives at around 25μm.

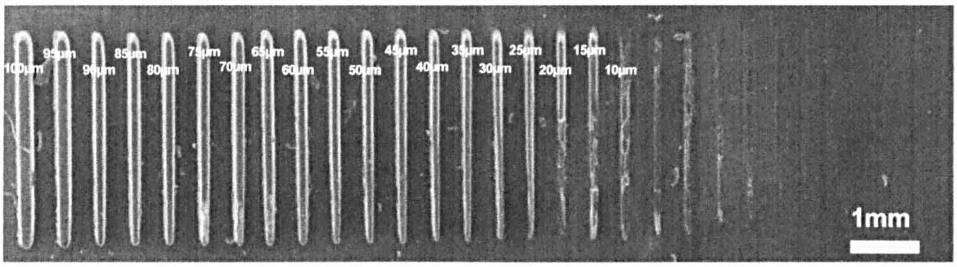

Figure 81 Failure in DLP progressively thinning walls (Hitachi).

Failed walls can no longer be considered to display fidelity to the design intent as they are of the order of one voxel width based on the measurements made in Figure 80. This suggests that there is a good correlation between the optical resolution and the resolution limited by material integrity during the build process.

A significant error is apparent in the thickness of these walls even when thickness is distant from the integer number of voxels used in the exposure. For example, if the design intent is a wall of width 60μm then this is clearly very close to 4 voxel widths. However, in the case of the 40 or 35μm the error is more significant. The image generation software should select the nearest integer number of voxels so for the 35μm a wall a minimum error of 14.3% based solely the errors introduced by voxel number alone.

This study defines a limitation of the capabilities of the apparatus. Although features can be built which are at the optical and mechanical resolution of the machine the percentage errors introduced by this method make it inappropriate for some applications. This may be acceptable in circumstances in which arrays of features are required in which some variation is permitted such as surface texturing.

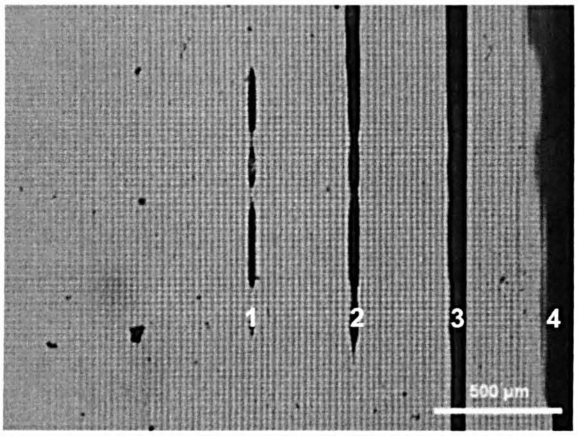

Figure 82 Voxel size and failure of thin walls.

The failure of walls through 'pull away' can also be seen in Figure 82. This optical micrograph also reveals the voxel geometry as the voxel edges are subject to a greater degree of polymerisation (through light spillage) during the build process. It is apparent that the walls fail because they are not wide enough to endure the repeated tensile load in the semi-cured state which is invoked by the peeling stage in the build. Walls 3 and 4 have survived the build process; however they have folded during cleaning or post-build curing. This is likely due to shrinkage when further cross linking causes consolidation of the material.

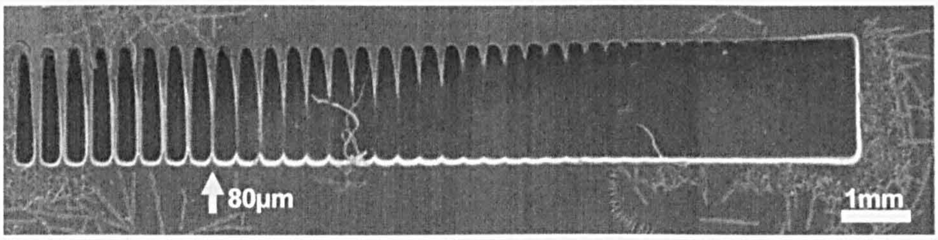

Figure 83 Failure in progressively thinning spaces between walls (Hitachi).

Further analysis was undertaken to evaluate the limits with regard to spacing between features within a build. This was achieved by maintaining a constant wall thickness and varying the space between consecutive walls (Figure 83). When the gap between walls reaches 80µm then the walls cease to be resolvable.

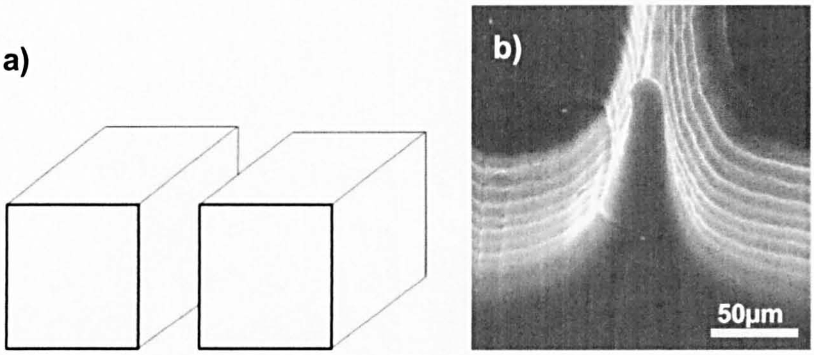

Figure 84 Blockage of thin walls through non clearance of resin a) the design intent and b) 'wall merging' (Hitachi)

An enlarged image of this failure can be seen in Figure 84. The separate walls can be identified but a meniscus feature is observed between walls indicating a retreat of uncured resin. This presents a further limit to resolution; namely resin removal in constricted spaces. This effect becomes a dominant factor when large aspect ratios are required. Walls depicted in Figure 82d) also display this failure.

Figure 85c) shows a slender extrusion of the text 'Test'. This demonstrates a typical fault (which is also observed to some degree in the thin walls) when building features with a large aspect ratio in the build direction. The repeated influence of curing shrinkage and stretching (caused by the peeling stage) has deformed the text and a constriction has occurred. This is contrast to the design intent which was for a uniform cross section throughout the height of the text.

The degree of chamfering appears to vary through the height of the thin walls. It can be attributed to the degree of polymerisation varying through the height of the wall. At the lower build layers (at the foot of the wall) more exposures will we experienced to those which follow.

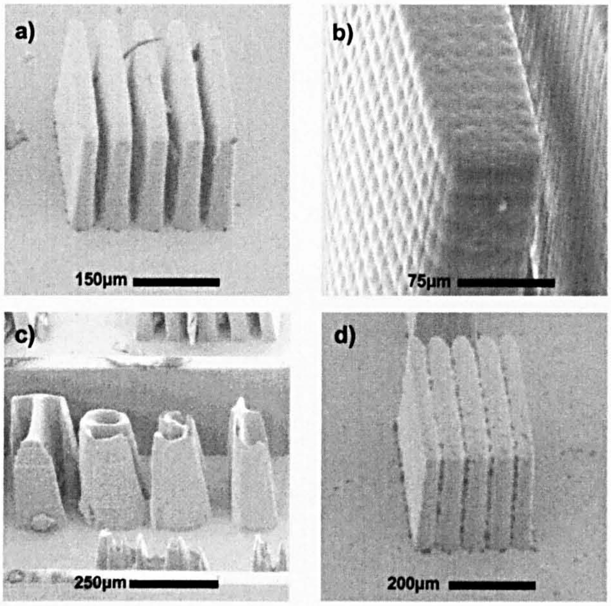

Figure 85 Assorted micrographs of DLP features (Hitachi).

From previous it can be observed that the thinnest resolvable thin wall is close to the theoretical limit of the optical resolution of the apparatus i.e. voxel size. However, 'real' life applications which may call upon such fine features are likely to be more complex and so limited by resin clearance.

One such example which would be subject to the resin clearance effect is the manufacture of capillaries. If the design intent is for a circular tube of inside diameter 100µm then this is clearly possible from an optical resolution stance. If the aspect ratio of the capillary is significant (length/cross section>50) then cleaning uncured resin from the void proves to be impossible despite mechanical agitation, ultrasonic agitation and forced purging. This is attributed to visco-elastic effects displayed by the resin within the capillary. This occurs as liquids are confined in capillaries they display both viscosity and eleasticity.

Therefore the cleaning of fine and enclosed features must be of concern at the point of design.

DLP for Mass Spectrometry

The flexibility of DLP as a manufacturing process for prototype electrical devices is now examined, particularly with regard to the tolerances obtainable and the ability to apply a conductive coating to the R5 material.

Quadrupole mass spectrometers (QMS) consist of three main sub assemblies; an ion source, mass filter and ion detection all mounted in a high vacuum vessel. Optimisation of a QMS system may require the geometry of electrodes to be adjusted. This is often a costly process requiring custom machining techniques. Modifications will be made more difficult by the fine features and complex surfaces which constitute the ideal design.

The use of LBMTs deals simultaneously with the cost of manufacturing prototypes and also allows for the manufacture of geometries which have been widely reported as ideal [149]. DLP components do not require custom tooling or custom machining strategies. Therefore they will be significantly cheaper than conventionally manufactured components for prototype mass spectrometers.

Digital manufacture also facilitates the integration of new/replacement components into existing assemblies. Geometrical data can be incorporated from several sources. For example the design software allows importing of data points from spreadsheet packages or metrology sources. These can be converted directly into code for LBMTs.

Ion Source

When a sample is admitted to a mass spectrometer ionisation is commonly achieved using an Electron Impact Ion Source (EIIS). These use incandescent filaments to emit electrons and ionise atoms or molecules present. The filament is commonly located in close proximity to a cylindrical mesh cage held at positive potential where ions are accelerated (Figure 86a).

A prototype EIIS was manufactured using DLP. This was first designed using a CAD package and built in four main components (Figure 86c). These were intended to mimic the performance of the conventional EIIS exactly. The elements consisted of: one extracting lens attached to the cage; two focusing lenses at negative dc voltages to focus ions towards the QMF and one decelerating lens held at 0V to reduce the ion energies before they enter the QMF. All components were evaporation gold coated to ensure the surfaces were conductive.

A good aperture alignment and hole precision is required for ion extraction and focusing. The EIIS pictured in Figure 86b) has exit aperture and Einzel lenses of diameter 400μm. These were aligned using DLP manufactured pins which can also be seen in Figure 86b). The mechanical tolerances upon assembly achieved were of sufficient standard to attempt testing.

In initial tests, without a mass filter, zero ion current was detected exiting the assembly and it was deduced that the EIIS was not acting as a source of ions. The reason for this was apparent upon removal of the lenses and cage (Figure 86b). Due to the proximity of the cage to the incandescent filaments the cage and the gold coating was significantly degraded due to a deformation of the underlying polymer.

The filaments must be located close to the EIIS cage to ensure that the emitted electrons have a high probability of impacting with a sample atom and thus cause ionisation. This suggests that the DLP process (or at least DLP in combination R5 is not a suitable process for building electron impact ion sources.

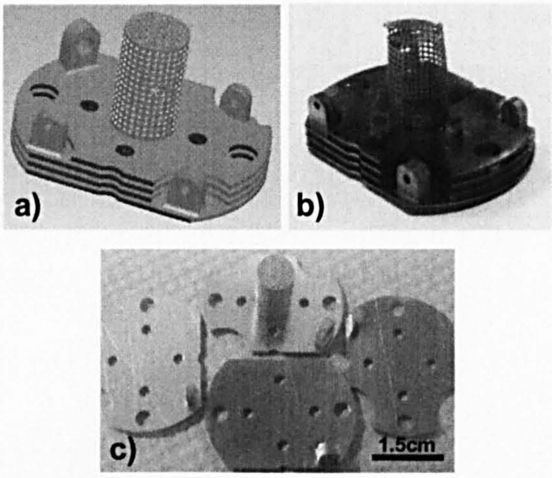

Figure 86 Prototype DLP ion source for use with mass spectrometers a) CAD model b) assembly after testing c) Cage plate with three Einzel lenses.

In light of the results obtained from the EIIS. An alternative spark gap ion source (SGIS) was proposed. This was intended to use the spark developed when electrical breakdown is observed, to ionise the atoms of the sample gas. Although high electrical fields are required to cause breakdown this would occur at relatively low currents so power consumption would be low and temperatures reduced.

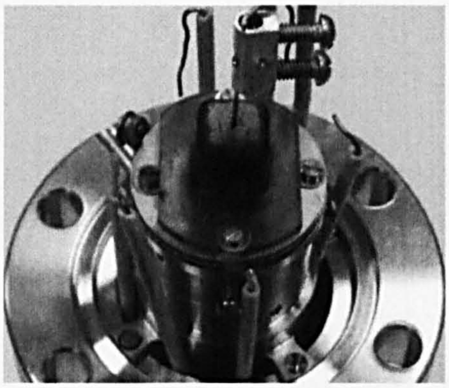

Figure 87 Prototype DLP spark gap ion source.

A prototype SGIS with 1mm exit aperture diameter and 500μm spark gap was manufactured as a demonstrator (Figure 87) which incorporated a DLP mounting to precisely locate and electrically isolate a probe pin.

Tests to evaluate the voltage required to cause breakdown were made at various pressures and were found to obey the Paschen curve (Figure 88a). Ideally the SGIS would operate at as high a pressure as possible so that power consumption of the entire unit would be minimised (i.e. lower vacuum required and spark potential minimised). However, if the unit is operated at a higher pressure, the mean free path of ions is significantly reduced and the signal detected will be degraded.

Figure 88a) shows the current obtained at various pressures. This test was performed using a conventional focussing rig without a mass filter and is intended only to demonstrate ion emission. In this case the ion source did emit but further experimentation will be required to increase ion emission current so that low noise mass spectra may be acquired.

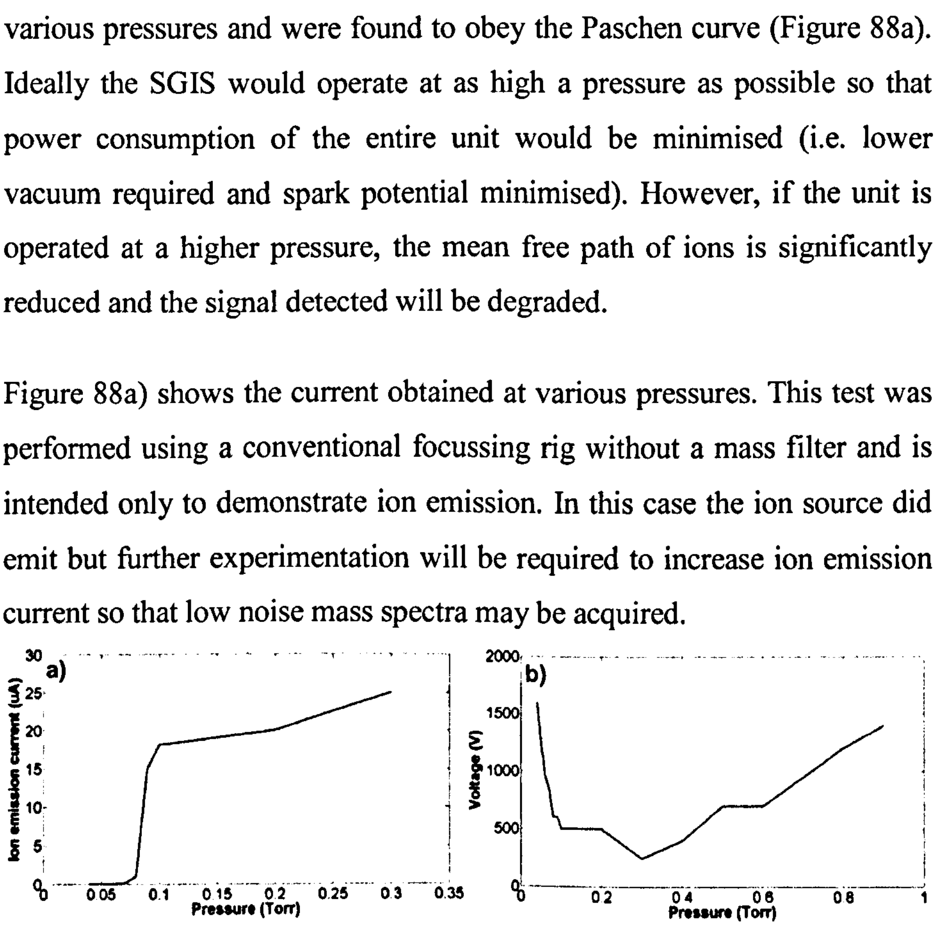

Figure 88 a) Ion emission current using the DLP SGIS b) voltage required to cause spark discharge for prototype DLP ion source.

One method of achieving a larger ion emission and hence greater detector signal would be to use a series of probe pins mounted in an annular pattern around the exit aperture. By increasing the potential at each of these at controlled intervals with a signal generator a multiple of sparks could be generated simultaneously causing a higher degree of ionisation and therefore higher emission current.

Modelling Using BEM

Boundary element modelling (BEM) was performed to aid in the design of DLP components. A numerical model was used to simulate individual mass peaks and complete mass spectra based upon parts to be manufactured by DLP.

This provided a means by which solid models produced in CAD can be subject to analysis before actually being built. This allows for design iterations without the investment of resource in an actual experiment.

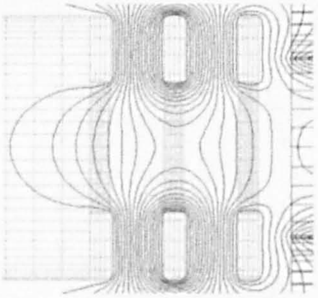

Figure 89 Typical predicted equipotentials from an ion source through Einzel lenses.

Modelling is achieved by coupling the CPO3D program [150] with Liverpool QMS-2 program [151]. The former calculates key values along the ion path which are used by the latter to give sample spectra. This approach allows the electrostatic analysis of any profile rod or lens aperture. Results obtained from this technique are presented alongside experimental results for mass filters.

This method can be iterated after experimentation if the filter or lens array is non ideal to investigate the implications for mass spectra obtained.

Mass Filter Design and Manufacture

The sub assembly presenting most potential for manufacture by DLP in this type of spectrometer is the mass filter. These components do not have to experience high temperatures and can be tailored when catering for custom needs such as mass range and resolution.

A prototype assembly was proposed (Figure 90a) which consists of a housing into which electrodes slide. The housing is designed to push fit directly into the existing experimental rig. This permits filters to be quickly interchanged.

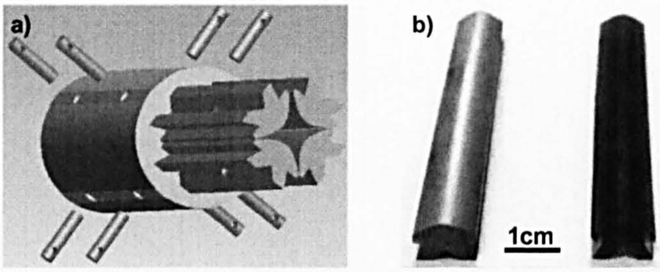

Figure 90 a) Prototype DLP mass filter b) coated and uncoated rods.

Electrical potentials are communicated to the rods via coated polymer pins inserted from the outside which serve to further locate the rods. A comparison of coated and uncoated rods can be seen in Figure 90b. Regions that are gold in colour (Figure 90a) are regions which have been selectively gold coated using a masked evaporation technique. Masking was undertaken using blanks also manufactured by DLP. This demonstrates the first use of 'rapid masking'.

The end-to-end resistance of the rods when gold coated was typically 40Ω. By improving the gold coating (or using an intermediate layer) the resistance can be further reduced, which will give more uniform driving voltages. This is especially important for miniature mass analyzers where localised deformations create patches of higher potentials which can increase ion bombardment heating if electrodes are not smooth enough, and cause the distortion of ion motion [152].

This assembly (Figure 90a) is further unique in that the rods have a hyperbolic profile. This is the 'ideal' theoretical geometry to create the optimum electric field between such rods [115]. In turn this means that lower voltages will be required to operate the filter causing it to be less power hungry permitting a larger mass range (Eq 6.1).

The design was created in CAD by importing a coordinate system from a spreadsheet package. This profile was the optimum for rods of this length and r_0 (Figure 93), 50mm and 2mm respectively in this case.

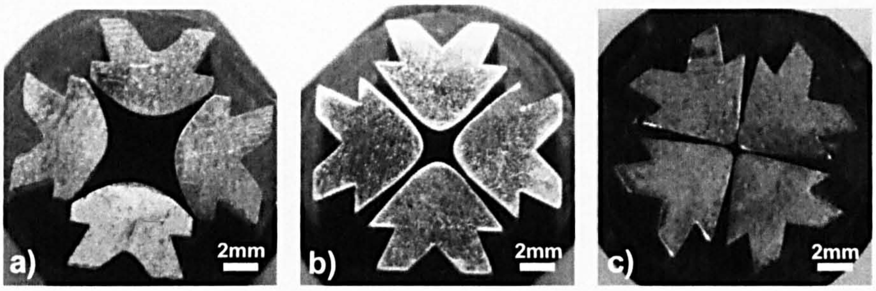

Figure 91 Prototype mass filters a) r_0=2mm b) r_0=0.9mm c) r_0=0.4mm.

Figure 91 shows the profiles of three mass filter assemblies produced by DLP and containing gold coated rods. The largest filter was selected for testing as it represented the closest model to existing filters for which the electronic requirements were already available.

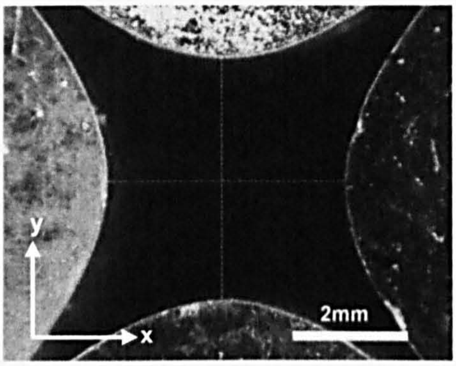

Figure 92 Fidelity to design intent of r_0.

The aperture size of the filter was considered to measure fidelity to the design intent. Ideally the finished article would be a perfect representation of the CAD model. It is characteristic of any manufacturing technique for this to be impossible. Resolution tests undertaken previously in this chapter indicate the accuracy of features made within the same build. Clearly the process of assembly in this case will also affect the tolerance between components. Figure 92 shows an optical microscopy image of the rod profile to evaluate rod alignment (Figure 93a) and r_0 separation (Figure 93b).

This is especially important for quadrupole mass filters where small displacements of the electrodes can severely reduce the performance of the instrument [153]. Measurements indicate that the spacing between rod peaks in the x direction was 4.06mm±0.025mm and 4.14mm±0.025mm in the y direction. This corresponds to an r_0 average error of 1.5%±0.625% and 3.5%±0.625% respectively. Circular rod-based filters with r_0>3mm manufactured by conventional means regularly surpass 1% r_0 error.

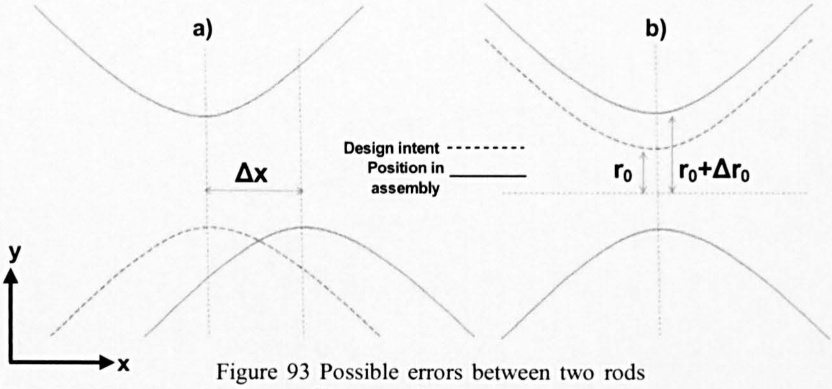

Figure 93 Possible errors between two rods in a mass filter assembly.

The example given in Figure 93 shows two possible sources of error resulting from shifts in both x and y directions. It is feasible to expect some rotation about the coordinate axis. Variation in these errors may also be observed along the rod length. In this situation the filter will continue to function assuming that Δx is not so large that adjacent rods come into contact. The error introduced corresponding to Δx in this assembled filter is negligible compared to the r_0 error Figure 94.

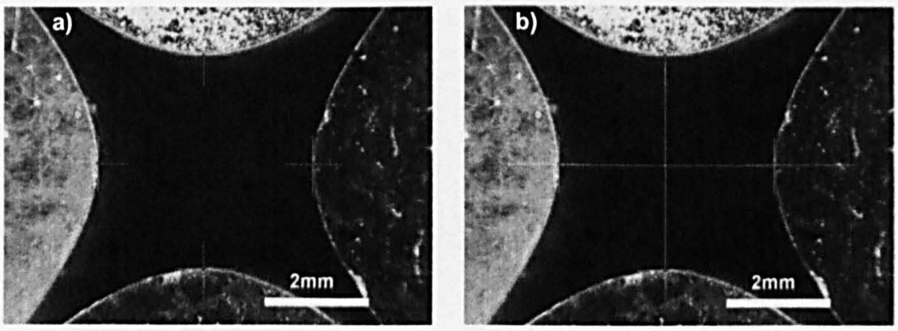

Figure 94 a) Location of hyperbola maxima b) maxima alignment.

Although these errors are deemed acceptable for the r_0=2mm filter, the proportional error ($\Delta r_0/r_0$) exhibited in the r_0=0.9mm would be much more significant. Thus if the maximum absolute $2r_0$ error (±0.165mm) observed in the r_0=2mm filter is transferred to that of the r_0=0.9mm mass filter then this corresponds to a percentage r_0 error of ±9.2% which is unsatisfactory. This may be reduced by building the entire filter as one part and selectively coating regions where required. This will avoid errors caused by assembly.

The surface roughness at the face of the rods is also of concern. By building these components at the minimum layer thickness currently available with this DLP apparatus (25μm) the observed staircase effect is minimised. Figure 95 shows the face of a gold coated rod. It can be seen that the surface roughness it consistent with that recorded on planar samples demonstrated earlier.

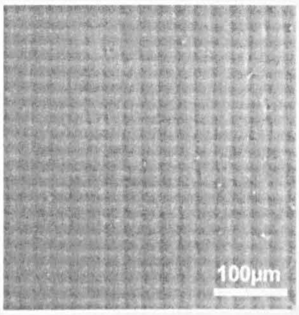

Figure 95 Active surface of prototype DLP electrodes (Hitachi).

Based on the measurements obtained on this section, it was decided to test the r_0=2mm mass filter in a standard mass spectrometer rig to evaluate its performance.

Mass Filter Testing

A commercial EIIS with one focusing lens was used to provide ions for filter testing. The ion cage has cylindrical shape with diameter of 6mm and length of 10mm (similar to the DLP version in Figure 86). Three lenses were used to direct the ion into the filter each of 0.3mm thickness and 0.8mm separation between them. The last was a decelerating lens which was separated from the top surface of the filter by 0.5mm. For testing the experimental 2mm mass filter and lenses with exit aperture radius (r_e) of 1.5mm were used.

During testing, the DLP mass filter (r_0=2mm) was driven at frequency of 3.686MHz. The ion source cage and the extracting lens were held at 4V, the focusing lens was held at -40V and the decelerating lens at 0V. The electron emission current for ionisation was 0.8mA and operating pressure was 1.2×10^{-4} Torr.

Simulations were carried out for the r_0=2mm and EIIS with specified driving parameters to obtain the mass peak for $^4He^+$ ions. This data was used to estimate the resolution that could be expected of the experimental filter. This is achieved by defining ratios between the dc and rf voltages that the electronic control unit generates for the simulation.

Optimum resolution ($M_m/\Delta M$) for peaks in mass spectra can then be assessed according to;

$$\frac{M_m}{\Delta M} = \frac{L^2 V_m}{570 V_z r_0^2} \tag{6.1}$$

as described in[115]. In which M_m is the maximum ion mass, ΔM is the width of the peak at mass M_m at 10% of its height, L is the length of the filter rod, V_m is the amplitude of the rf voltage applied across the rod and V_z is the extraction potential as ions enter the mass filter. This allows for a comparison of experimentally observed resolution with that predicted by modelling (Figure 96).

In an ideal scenario, the ion current should be maximised to yield the greatest signal. However, in doing so the extraction voltage must also be increased which increases ion energies and so reduce the filter's resolution, Figure 96.

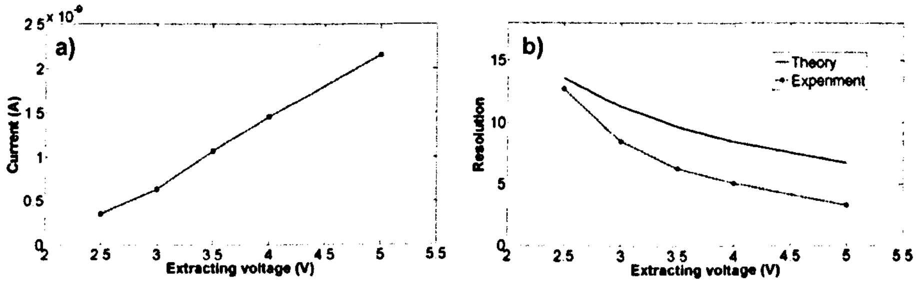

Figure 96 a) Variation of ion current for $^4He^+$ ions using the DLP QMF b) Comparison of resolution for the DLP QMF r_0=2mm and model results.

The ion motion within the ion source was modelled in a commercial software package with $^4He^+$ ions starting their oscillation within the cage at energy of 0.01eV. The effects of space charge upon the ions in the ion source and the fringing fields when ions reach the mass filter were also included. The trajectories of the $^4He^+$ ions which were successfully extracted from EIIS (position coordinates, velocity components and ion energies) were then loaded into the software package developed at the University of Liverpool, QMS-2 v8. Figure 97 shows a simulated $^4He^+$ peak obtained from the QMS-2 program for an ideal hyperbolic r_0=2mm mass filter operating in the zone 1 stability region.

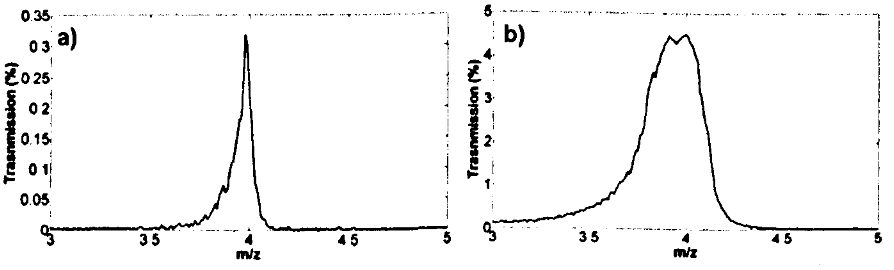

Figure 97 Simulated mass peak for $^4He^+$ ions oscillating within the hyperbolic DLP QMF (CPO and Liverpool QMS-2 programs) a) optimised b) un-optimised.

This predicts a resolution of 5.71 at 10% of the peak height for mass 4. Optimised data is also included to detail the influence of data processing. This peak shows a much higher resolution of 16.67.

Experiments using the DLP mass filter showed that it was fit for purpose. The experimentally obtained peak corresponding to the model above can be seen in Figure 98. The predicted resolution is consistent with this peak which has a resolution of 5.13, a deviation of -10.2% compared to the model. Testing was continued to investigate mass spectra as well as individual mass peaks.

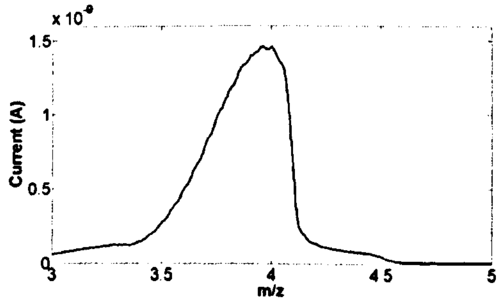

Figure 98 Experimental mass peaks for $^4He^+$ ions.

The data above is not an experimentally optimised resolution for this spectral peak but rather a resolution that has been repeatedly obtained.

Commercial Mass Filter

To investigate the performance of the r_0=2mm DLP mass filter a test spectrum was obtained for comparison with a commercially available filter.

The MKS Instruments mass filter has an r_0 = 3.175mm and electrode length of 100mm i.e. double that used for the DLP filter. Lens and extraction potentials were set according to manufacturer prescribed settings. This experiment was intended to demonstrate the benefits of the hyperbolic geometry employed in the DLP mass filter compared to that in the cylindrical MKS system.

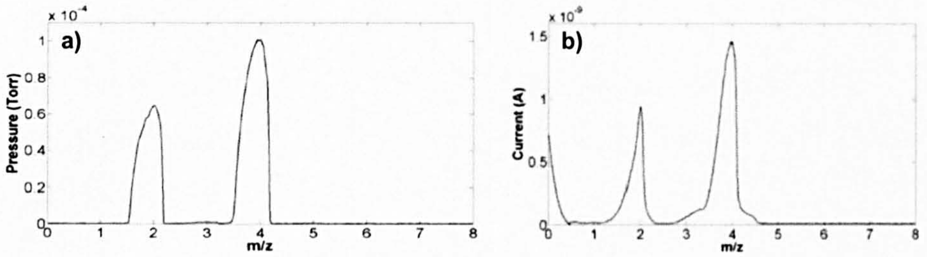

Figure 99 Spectra for $H_2/D_2/He$ mixture a) Commercial MKS mass filter with circular rods r_0=3.175mm b) DLP hyperbolic mass filter r_0=2mm.

Figure 99a shows the experimental mass spectrum for the $H_2/D_2/He$ equal concentration gas mixture measured using a commercial QMS with circular electrodes having both pre-filter and post-filter (ordinate is given as pressure as standard with MKS software). Deuterium and helium cannot be resolved. This is also the case for the DLP filter Figure 99b.

Species	MKS (Circular rods)	DLP (Hyperbolic rods)	Relative performance
H_2^+	3.17	3.03	-4.4%
D_2^+	5.88	5.13	-12.8%
He^+	5.88	5.13	-12.8%

Table 13 Summary of peak resolutions (at 10% peak height) for a DLP mass filter and a conventional alternative

The commercial mass filter produces slightly higher resolutions. This is largely due to its increased length relative to the hyperbolic filter and also the pre and post filters. A good correlation between the ratios of peaks heights (MKS-1:1.59, DLP-1:1.53) can also be observed in Figure 99. This provides further evidence that the DLP manufacturing technique is well suited to manufacture mass filter prototypes.

Conclusions

The performance of components manufactured by DLP has been characterised. These have been shown to vary significantly from the bulk material properties quoted by the supplier.

A series of hyperbolic quadrupole mass filters have been fabricated using DLP and proven to work as mass spectrometers. The technique was found to be particularly suitable for prototyping mass filters that provide ideal hyperbolic field or for any other devices with complex geometries.

Compared to other rapid prototyping techniques digital light processing offers significantly smaller feature sizes, which allows a higher degree of accuracy both in manufacture and assembly. It also has the potential to produce a fully integrated mass spectrometer with a single mass analyzer or with array of analyzers at sub-millimetre and micro scale.

7. Conclusions

This thesis describes the outcomes of a body of research in which layer-based manufacturing techniques have been used to process a range of functional materials.

Novel techniques have been used to manufacture demonstrators/prototypes which have the potential to be utilised in engineering applications. Within the processes of refining material, parameter set and design several conclusions can be made which represent the core outcomes of this work.

A commercial NiTi powder has been processed for the first time via the SLM technique to produce near 100% dense parts which exploit design freedoms granted by LBMTs.

These NiTi components have been shown to display the shape memory effect and have been trained and later actuated to exhibit the shape memory effect. Furthermore they have been actuated by ohmic heating.

The process of melting by laser and further reheating appears to induce the presence of the so-called R-phase which is normally consistent with aged Ni rich alloys. Processing NiTi powders in this way may serve to produce components which imitate those that have been aged. The presence of contaminants, however, cannot be ruled out as an austenite stabiliser.

Piezoelectric-ceramic/polymer composites have been manufactured and been selectively sintered to silicon substrates demonstrating lithographic deposition techniques combined with laser interaction are capable of selective deposition.

Selectively sintered regions have been consolidated by laser treatment. This causes partial sintering and adherence to the substrate. The processed regions are typical of components which might be employed by 'lab on a chip' devices.

Piezoelectric-ceramic/polymer composites have been fabricated with the DLP technique and used to build freeform components. Microscopic analysis and calculation has predicted that piezoelectric properties could be of the same order as materials processed by conventional methods.

Material properties and resolution tests have been performed on samples built by the DLP process. These have been shown to display a high degree of variance. There is also significant deviation with respect to the manufacturer's bulk material quotations.

DLP has been used to manufacture components for quadrupole mass spectrometry. DLP has been shown to be especially effective for mass filter manufacture more specifically the manufacture of complex profile electrodes. Metallisation of the plastic components which meet with specification have been shown to outperform conventional filters in terms of both cost and functionality.

8. Future Work

The outcomes of this thesis present several opportunities for further work. These relate to further investigations into the effect of manufacturing parameters upon material properties and the incorporation of prototypes/demonstrators into new applications.

1. Surface finish, build reliability and tolerances across SLM platforms are widely reported problems. Processing NiTi was typical of the process with respect to those factors. To minimise post processing and hence cost, addressing these limitations would form an excellent topic of research. This is likely to rely heavily upon laser/material interaction modeling to optimise the build approximation to the design intent.

2. Although the SME has been demonstrated for SLM processed NiTi alloys the degree of SME with respect to manufacturing parameter set has not been investigated in this work. This presents significant challenges to prepare a range of material samples to be subjected to a range of training regimes and later analytical techniques. This will allow the enhancement of components manufactured in this way for product applications. Porous materials and meshes can easily be manufactured by SLM. Shape memory materials in this form would find several possible application including 'self healing' crash structures or perhaps temperature sensitive filters.

3. The extent of the R-phase present in SLM processed NiTi alloys requires further investigation. One approach to this would be TEM and XRD analysis under thermally controlled conditions.

4. Piezoelectric / pyroelectric pads deposited on silicon substrates can be employed for sensory and actuation applications. Research into poling these pads and incorporating similar structures into MEM type components may be possible. The viability of this is dependent upon the mechanical integrity and adherence of the piezoelectric material.

5. Poling of $BaTiO_3$/R5 composites is a subject of ongoing research as is the implication of ceramic content on the resolution of the DLP process. Demonstrator builds performed in this study are of a limited height and the distribution of ceramic content through build height was not observed to vary greatly. This might not be the case in scaled up builds.

6. Resolution and material tests were performed on a single machine/material combination in this study. There are several competing platforms (SLA, 3DP etc) and material feedstocks available for each. Thus a true evaluation of machine/material performance would require manufacturer collaboration. To date manufacturers of LBMT apparatus are reluctant to issue standardised results. This is currently under review with the formation of an ASTM working group [154]. The development of accepted standards is fundamental to the proliferation of LBMTs.

7. Coated DLP components have been demonstrated to be highly effective in mass filters for spectrometry applications. There are various similar components such as ion traps and more complicated filters which could be manufactured in this way. Youssef et al [155] predicted an ideal quadrupole mass filter would not only be hyperbolic in profile but also helical (twisted) in trajectory. This was proposed in 1971 but has to date not been successfully realised.

9. References

1. Chang, L.C. and T.A. Read, *Experimental Evidence of Relaxation During Diffusionless Phase Changes of Single Crystal Beta-Au-Cd Alloys Contianing 47.5 Atomic Percent Cd.* Physical Review, 1951. **82**(5): p. 770-770.
2. Buehler, W.J., J.V. Gilfrich and R.C. Wiley, *Effect of Low-Temperature Phase Changes on the Mechanical Properties of Alloys near Composition TiNi.* Journal of Applied Physics, 1963. **34**(5): p. 1475-1477.
3. Otsuka K, W.C.M., *Shape Memory Materials.* 1 ed. 1998: Cambridge University Press.
4. Brick R.M, G.R.B., Phillips A, *Structure and Propeties of Alloys.* 3 ed. 1965: Mcgraw-Hill Book Company.
5. Tsuchiya, K. and S.T. Davies, *Fabrication of TiNi shape memory alloy microactuators by ion beam sputter deposition.* Nanotechnology, 1998. **9**(2): p. 67-71.
6. Huang, W.M., Q.Y. Liu, L.M. He and J.H. Yeo, *Micro NiTi-Si cantilever with three stable positions.* Sensors and Actuators a-Physical, 2004. **114**(1): p. 118-122.
7. Fu, Y.Q., H.J. Du, W.M. Huang, S. Zhang and M. Hu, *TiNi-based thin films in MEMS applications: a review.* Sensors and Actuators a-Physical, 2004. **112**(2-3): p. 395-408.

8. Wollants, P., J.R. Roos and K. Otsuka, *Ont the Thermodynamic-Equilibrium of Stress-Induced Martensite Transformations.* Zeitschrift Fur Metallkunde, 1991. **82**(3): p. 182-185.

9. Mihalcz, I., *Fundamental characteristics and design method for nickel-titanium shape memory alloy.* Mechanical Engineering, 2001. **45**(1): p. 75-86.

10. Karpagavalli, R., A.H. Zhou, P. Chellamuthu and K. Nguyen, *Corrosion behavior and biocompatibility of nanostructured TiO2 film on Ti6Al4V.* Journal of Biomedical Materials Research Part A, 2007. **83A**(4): p. 1087-1095.

11. Schrooten, J., M. Assad, J. Van Humbeeck and M.A. Leroux, *In vitro corrosion resistance of porous NiTi intervertebral fusion devices.* Smart Materials & Structures, 2007. **16**(1): p. S145-S154.

12. Man, H.C., K.L. Ho and Z.D. Cui, *Laser surface alloying of NiTi shape memory alloy with Mo for hardness improvement and reduction of Ni2+ ion release.* Surface & Coatings Technology, 2006. **200**(14-15): p. 4612-4618.

13. Lopez, H.F., A. SalinasRodriguez and J.L. RodriguezGalicia, *Microstructural aspects of precipitation and martensitic transformation in a Ti-rich Ni-Ti alloy.* Scripta Materialia, 1996. **34**(4): p. 659-664.

14. Hebda, D.A. and S.R. White, *Effect of training conditions and extended thermal cycling on nitinol two-way shape memory behavior.* Smart Materials & Structures, 1995. **4**(4): p. 298-304.

15. Khalil-Allafi, J., W.W. Schmahl and D.M. Toebbens, *Space group and crystal structure of the R-phase in binary NiTi shape memory alloys.* Acta Materialia, 2006. **54**(12): p. 3171-3175.

16. Luo, H.Y., E. Abel, J. Hewit, M. Pridham, B. Steele, Z. Wang and A. Slade, *Issues concerning the measurement of transformation temperatures in NiTi alloys*, in *Smart Materials Ii*, A.R. Wilson and V.V. Varadan, Editors. 2002. p. 226-233.

17. Malukhin, K. and K. Ehmann, *Material characterization of NiTi based memory alloys fabricated by the laser direct metal deposition process.* Journal of Manufacturing Science and Engineering-Transactions of the Asme, 2006. **128**(3): p. 691-696.

18. Mentz, J., M. Bram, H.P. Buchkremer and D. Stover, *Improvement of mechanical properties of powder metallurgical NiTi shape memory alloys.* Advanced Engineering Materials, 2006. **8**(4): p. 247-252.

19. Bihlmayer, A.G., A.R. Eibler and A.A. Neckel, *Electronic structure of the martensitic phases B19'-NiTi and B19-PdTi.* Journal of Physics: Condensed Matter, 1993. **29**(5083).

20. Khalil-Allafi, J., W.W. Schmahl and T. Reinecke, *Order parameter evolution and Landau free energy coefficients for the B2 <-> R-*

phase transition in a NiTi shape memory alloy. Smart Materials & Structures, 2005. **14**(5): p. S192-S196.

21. Miyazaki, S. and M. Kohl, *Recent development in TiNi-based shape memory alloys*, in *Smart Structures and Materials 1998: Smart Materials Technologies*, M. Wuttig, Editor. 1998. p. 2-13.
22. Hane, K.F. and T.W. Shield, *Microstructure in the cubic to trigonal transition.* Materials Science and Engineering A, 2000. **291**(1-2): p. 147-159.
23. Hane, K.F. and T.W. Shield, *Microstructure in the cubic to monoclinic transition in titanium-nickel shape memory alloys.* Acta Materialia, 1999. **47**(9): p. 2603-2617.
24. Tan, L., G. Shaw, K. Sridharan and W.C. Crone, *Effects of oxygen ion implantation on wear behavior of NiTi shape memory alloy.* Mechanics of Materials, 2005. **37**(10): p. 1059-1068.
25. Cady, W.G., *Piezoelectricity.* Vol. 1. 1964: Dover Publications.
26. Smith, C., Wise M. N *Energy and Empire: A Biographical Study of Lord Kelvin.* 1989: Cambridge University Press.
27. Leo, D.J., *Engineering Analysis of SMART Material Systems.* 1 ed. 2007: John Wiley & Sons.
28. Jang, L.S. and Y.C. Yu, *Peristaltic micropump system with piezoelectric actuators.* Microsystem Technologies-Micro-and Nanosystems-Information Storage and Processing Systems, 2008. **14**(2): p. 241-248.

29. Bharti, V. and R. Nath, *Piezo-, pyro- and ferroelectric properties of simultaneously stretched and corona poled extruded poly(vinyl chloride) films.* Journal of Physics D-Applied Physics, 2001. **34**(5): p. 667-672.

30. Kanno, I., Y. Tazawa, T. Suzuki and H. Kotera, *Piezoelectric unimorph miroactuators with X-shaped structure composed of PZT thin films.* Microsystem Technologies-Micro-and Nanosystems-Information Storage and Processing Systems, 2007. **13**(8-10): p. 825-829.

31. Liu, M.W., T.H. Cui, W.J. Dong, Y. Cui, J. Wang, L.Q. Du and L.D. Wang, *Piezoelectric microcantilevers with two PZT thin-film elements for microsensors and microactuators*, in *2006 1st Ieee International Conference on Nano/Micro Engineered and Molecular Systems, Vols 1-3.* 2006. p. 775-778.

32. Fu, Y., E.C. Harvey, M.K. Ghantasala and G.M. Spinks, *Design, fabrication and testing of piezoelectric polymer PVDF microactuators.* Smart Materials & Structures, 2006. **15**(1): p. S141-S146.

33. Kumar, A. and M.M. Perlman, *Simultaneous Stretching and Corona Poling of PVDF and P(VDF-TRIFE) Films .2.* Journal of Physics D-Applied Physics, 1993. **26**(3): p. 469-473.

34. Gottmann, J., B. Vosseler and E.W. Kreutz, *Laser crystallisation during pulsed laser deposition of barium titanate thin films at low temperatures.* Applied Surface Science, 2002. **197**: p. 831-838.

35. Kasai, T., Y. Ozaki, H. Noda, K. Kawasaki and K. Tanemoto, *Laser-Sintered Barium-Titanate.* Journal of the American Ceramic Society, 1989. **72**(9): p. 1716-1718.

36. Belushkin, A.V., D.P. Kozlenko, N.O. Golosova, P. Zetterstrom and B.N. Savenko, *A study of disorder effects at ferroelectric phase transition in BaTiO3.* Physica B-Condensed Matter, 2006. **385**: p. 85-87.

37. Chaisan, W., R. Yimnirun and S. Ananta, *Two-stage sintering of barium titanate ceramic and resulting characteristics.* Ferroelectrics, 2007. **346**: p. 84-92.

38. (PI), P.I. *Piezo-University.* 1996-2009 [cited 22/4/2009]; Available from: http://www.physikinstrumente.com.

39. Deshpande, S.B., P.D. Godbole, Y.B. Khollam and H.S. Potdar, *Characterization of barium titanate: BaTiO3 (BT) ceramics prepared from sol-gel derived BT powders.* Journal of Electroceramics, 2005. **15**(2): p. 103-108.

40. Kwon, S.W. and D.H. Yoon, *Effects of heat treatment and particle size on the tetragonality of nano-sized barium titanate powder.* Ceramics International, 2007. **33**(7): p. 1357-1362.

41. Wada, S., H. Yasuno, T. Hoshina, S.M. Nam, H. Kakemoto and T. Tsurumi, *Preparation of nm-sized barium titanate fine particles and their powder dielectric properties.* Japanese Journal of Applied Physics Part 1-Regular Papers Short Notes & Review Papers, 2003. **42**(9B): p. 6188-6195.

42. Buscaglia, V., M.T. Buscaglia, M. Viviani, L. Mitoseriu, P. Nanni, V. Trefiletti, P. Piaggio, I. Gregora, T. Ostapchuk, J. Pokorny and J. Petzelt, *Grain size and grain boundary-related effects on the properties of nanocrystalline barium titanate ceramics.* Journal of the European Ceramic Society, 2006. **26**(14): p. 2889-2898.

43. Polotai, A., K. Breece, E. Dickey, C. Randall and A. Ragulya, *A novel approach to sintering nanocrystalline barium titanate ceramics.* Journal of the American Ceramic Society, 2005. **88**(11): p. 3008-3012.

44. Baldus, O. and R. Waser, *Experimental and numerical investigations of heat transport and crystallization kinetics in laser-induced modification of barium strontium titanate thin films.* Applied Physics a-Materials Science & Processing, 2005. **80**(7): p. 1553-1562.

45. Ibrahim, A., M. Yahaya and M.M. Salleh, *BaTiO3 nanocomposite thin film as pyroelectric sensor*, in *2004 Ieee International Conference on Semiconductor Electronics, Proceedings*, B.Y. Majlis and S. Shaari, Editors. 2004. p. 415-418.

46. Ihlefeld, J.F., W.J. Borland and J.P. Maria, *Enhanced dielectric and crystalline properties in ferroelectric barium titanate thin films.* Advanced Functional Materials, 2007. **17**(7): p. 1199-1203.

47. Kaiser, D.L., M.D. Vaudin, G. Gillen, C.S. Hwang, L.H. Robins and L.D. Rotter, *Growth and Characterization of Barium-Titanate Thin-Films Prepared by Metalorganic Chemical-Vapor-Deposition.* Journal of Crystal Growth, 1994. **137**(1-2): p. 136-140.

48. Suzuki, K. and K. Kijima, *Preparation and dielectric properties of polycrystalline films with dense nano-structured BaTiO3 by chemical vapor deposition using inductively coupled plasma.* Vacuum, 2006. **80**(6): p. 519-529.

49. Ohno, T., D. Suzuki, K. Ishikawa, M. Horiuchi, T. Matsuda and H. Suzuki, *Size effect for Ba(ZrxTi1-x)O-3 (x=0.05) nano-particles.* Ferroelectrics, 2006. **337**: p. 1197-1204.

50. Pithan, C., Y. Shiratori, R. Waser, J. Dornseiffer and F.H. Haegel, *Preparation, processing, and characterization of nano-crystalline BaTiO3 powders and ceramics derived from microemulsion-mediated synthesis.* Journal of the American Ceramic Society, 2006. **89**(9): p. 2908-2916.

51. Duffy, W., B. Cheng, M. Gabbay and G. Fantozzi, *An elastic behavior of barium-titanate-based ceramic materials.* Metallurgical and Materials Transactions A, 1995. **26**(7): p. 1735-1739.

52. Lu, H.A., L.A. Wills and B.W. Wessels, *Electrical-Properties and Poling of BaTiO3 Thin-Films.* Applied Physics Letters, 1994. **64**(22): p. 2973-2975.

53. Thongrueng, J., T. Tsuchiya, Y. Masuda, S. Fujita and K. Nagata, *Properties and degradation of polarization reversal of soft BaTiO3 ceramics for ferroelectric thin-film devices.* Japanese Journal of Applied Physics Part 1-Regular Papers Short Notes & Review Papers, 1999. **38**(9B): p. 5309-5313.

54. Kim, S.J., K.J. Kim, N.J. Seong, J.B. Wang, H.J. Park and M.Y. Kim, *The degradation of barium titanate (BaTiO3) films under high electric fields*, in *1998 International Symposium on Electrical Insulating Materials, Proceedings.* 1998. p. 147-150.

55. Chaudhari, G.N., D.R. Bambole and A.B. Bodade, *Structural and gas sensing behavior of nanocrystalline BaTiO3 based liquid petroleum gas sensors.* Vacuum, 2006. **81**(3): p. 251-256.

56. Wan, F., J.G. Han and Z.Y. Zhu, *Dielectric response in ferroelectric BaTiO3.* Physics Letters A, 2008. **372**(12): p. 2137-2140.

57. Agoudjil, B., L. Ibos, Y. Candau and J.C. Majeste, *A comparative analysis of dielectric, rheological and thermophysical behaviour of ethylene vinyl acetate/BaTiO3 composites.* Journal of Physics D-Applied Physics, 2008. **41**(5).

58. Dang, Z.M., Y.F. Yu, H.P. Xu and J. Bai, *Study on microstructure and dielectric property of the BaTiO3/epoxy resin composites.* Composites Science and Technology, 2008. **68**(1): p. 171-177.

59. Kawai, H., *The Piezoelectricity of Poly (vinylidene Fluoride).* Journal of Applied Physics, 1969. **8**(975): p. 11.

60. Furukawa , M.D., E. Fukada, Y. Tajistu, A. Chiba, *Ferroelectric Behavior in the Copolymer of Vinylidenefluoride and Trifluoroethylene.* Journal of Applied Physics, 1980. **19**(L109).

61. Eberle, G., E. Bihler and W. Eisenmenger, *Polarization Dynamics Of Vdf-Trfe Copolymers.* Ieee Transactions on Electrical Insulation, 1991. **26**(1): p. 69-77.

62. Kaura, T., R. Nath and M.M. Perlman, *Simultaneous Stretching And Corona Poling Of Pvdf Films.* Journal of Physics D-Applied Physics, 1991. **24**(10): p. 1848-1852.

63. Kaura, T. and R. Nath, *Simultaneous Stretching And Corona Poling Of Pvdf And P(Vdf-Trife) Films. II*

Journal of Physics D-Applied Physics, 1992. **26**(1993): p. 469-473.

64. Luo, X.T., L.F. Chen, Q.J. Huang, Q.L. Wu and Y.P. Hong, *Preparation and properties of PVDF matrix piezoelectric composites containing highly aligned BaTiO3 whiskers.* Journal of Inorganic Materials, 2004. **19**(1): p. 183-188.

65. Ploss, B., *Influence of poling and annealing on the nonlinear dielectric permittivity of PVDF-TRFE copolymers.* Ieee

Transactions on Dielectrics and Electrical Insulation, 1998. **5**(1): p. 91-95.

66. Su, J., Z. Ounaies and J.S. Harrison, *Ferroelectric and piezoelectric properties of blends of poly(vinylidene fluoride-trifluoroethylene) and a graft elastomer*, in *Electroactive Polymers*, Q.M. Zhang, et al., Editors. 2000. p. 95-100.

67. Su, J., Z. Ounaies, J.S. Harrison, Y. Bar-Cohen and S. Leary, *Electromechanically active polymer blends for actuation*, in *Smart Structures and Materials 2000: Electroactive Polymer Actuators and Divices*, Y. BarCohen, Editor. 2000. p. 65-72.

68. Tang, Y.Z.X., Chan HLW, Choy CL. *Electron irradiation effects in electrostrictive P(VDF-TrFE) copolymers* in *THE 2001 12TH IEEE INTERNATIONAL SYMPOSIUM ON APPLICATIONS OF FERROELECTRICS.* 2001

69. Dveyaharon, H., T.J. Sluckin, P.L. Taylor and A.J. Hopfinger, *Kink Propogation as a Model for Poling in Poly(Vinylidene Fluoride).* Physical Review B, 1980. **21**(8): p. 3700-3707.

70. Gimenes, R., M.A. Zaghete, M. Bertolini, J.A. Varela, L.O. Coelho and N.F. Silva, *Composites PVDF-TrFE/BT used as bioactive membranes for enhancing bone regeneration*, in *Smart Structures and Materials 2004: Electroactive Polymer Actuators and Devices*, Y. BarCohen, Editor. 2004. p. 539-547.

71. Migahed, M.D., M.I. Abdel-Hamid and A. Wafa, *Relaxation behavior in polarized PVDF films under the influence of mechanical and thermal multistresses above glass-transition temperature.* Journal of Applied Polymer Science, 1998. **70**(5): p. 859-864.

72. Nam, Y.W., W.N. Kim, Y.H. Cho, D.W. Chae, G.H. Kim, S.P. Hong, S.S. Hwang and S.M. Hong, *Morphology and physical properties of binary blend based on PVDF and multi-walled carbon nanotube.* Macromolecular Symposia, 2007. **249**: p. 478-484.

73. Kim, G.H. and S.M. Hong, *Structures and physical properties of carbon nanotube reinforced PVDF composites.* Molecular Crystals and Liquid Crystals, 2007. **472**: p. 551-559.

74. Paradiso, R., G. Loriga and N. Taccini, *A wearable health care system based on knitted integrated sensors.* Ieee Transactions on Information Technology in Biomedicine, 2005. **9**(3): p. 337-344.

75. Ray, M.C. and R.C. Batra, *A single-walled carbon nanotube reinforced 1-3 piezoelectric composite for active control of smart structures.* Smart Materials & Structures, 2007. **16**(5): p. 1936-1947.

76. Betti, M., C.C. Baniotopoulos and G.E. Stavroulakis, *Modeling and simulation of piezoelectric-active control of wind-induced*

vibrations on beams, in *Topics on Mathematics for Smart Systems*, B. Miara, G. Stavroulakis, and V. Valente, Editors. 2007. p. 61-75.

77. Arous, M., H. Hammami, M. Lagache and A. Kallel, *Interfacial polarization in piezoelectric fibre-polymer composites.* Journal of Non-Crystalline Solids, 2007. **353**(47-51): p. 4428-4431.

78. Sakamoto, W.K., S. Shibatta-Kagesawa, D.H.F. Kanda, S.H. Fernandes, E. Longo and G.O. Chierice, *Piezoelectric effect in composite polyurethane - Ferroelectric ceramics.* Physica Status Solidi a-Applied Research, 1999. **172**(1): p. 265-271.

79. Topolov, V.Y., S.V. Glushanin and A.E. Panich, *Features of the piezoelectric response for a novel four-component composite structure.* Ferroelectrics, 2004. **308**: p. 53-65.

80. Tuncer, E., I. Sauers, D.R. James, A.R. Ellis, M.P. Paranthaman, T. Aytug, S. Sathyamurthy, K.L. More, J. Li and A. Goyal, *Electrical properties of epoxy resin based nano-composites.* Nanotechnology, 2007. **18**(2).

81. Hull , D.C.T.W., *An Intorduction to Composite Materials.* 2 ed. Cambridge Solid State Series. 1981.

82. Thamjaree, W., W. Nhuapeng , A. Chaipanich and T. Tunkasiri, *Fabrication of combined 0–3 and 1–3 connectivities PZT/epoxy resin composites* Applied Physics A: Materials Science & Processing, 2005. **Volume 81,** (7): p. 1419-1422.

83. Thomas, F.M., Victor F. Janas Ahmad Safari Roland L. Loh Richard B. Cass, *Novel Processing of 1-3 Piezoelectric Ceramic/Polymer Composites for Transducer Applications.* Journal of the American Ceramic Society, 1995. **78**(11): p. 2913-2916.

84. Lushcheĭkin, G., *New polymer-containing piezoelectric materials.* Physics of the Solid State, 2006. **48**(6): p. 1023-1025.

85. Kwok, K.W., C.K. Wong, R. Zeng and F.G. Shin, *AC Poling study of lead zirconate titanate/vinylidene fluoride-trifluoroethylene composites.* Applied Physics a-Materials Science & Processing, 2005. **81**(1): p. 217-222.

86. Luo, X.T., L.F. Chen, X.J. Chen and Q.J. Huang, *Preparation and electromechanical properties of PVDF matrix piezo-electric composites containing highly oriented BaTiO3 whiskers.* Journal of Materials Science & Technology, 2004. **20**(4): p. 441-444.

87. Luo, X.L.C., Xiaojun Chen, Qianjun Huang, *Preparation and Electromechanical Properties of PVDF Matrix Piezoelectric Composites Containing Highly Oriented BaTiO3 Whiskers.* Journal of Materials Science & Technology, 2004. **20**(4): p. 441-444.

88. Hauser , C., C. Sutcliffe, M. Egan and P. Fox. *Spiral Growth Manufacturing (SGM) – A Continuous Additive Manufacturing Technology For Processing Metal Powder by Selective Laser Melting.* in *Solid Freeform Fabrication Proceedings*. 2005.

89. Gebhardt, A., *Rapid Prototyping.* 1 ed. 2003, Muncih: Hanser.

90. Kruth, J.P., *Benchmarking of Different SLS/SLM Processes as Rapid Manufacturing Techniques*, in *International Conference of Polymers and Mould Innovations*. 2005, PMI: Gent, Belgium. p. 7.

91. Becker, H., S. Czerner, A. Ostendorf, P. Stippler and P. Matteazzi, *Technology improvements for micro scale laser sintering*, in *Opto-Ireland 2005: Photonic Engineering*, B.W. Bowe, et al., Editors. 2005. p. 467-474.

92. Venuvinod, P.K., *Rapid Prototyping-Laser Based and Other Technologies*. 2004: Kluwer Academic Publishers.

93. Wong, M., S. Tsopanos, C. Sutcliffe and E. Owen, *Selective laser melting of heat transfer devices*. Rapid Prototyping Journal, 2007. **13**(5): p. 291-297.

94. Morgan, R., C.J. Sutcliffe and W. O'Neill, *Density analysis of direct metal laser re-melted 316L stainless steel cubic primitives*. Journal of Materials Science, 2004. **39**(4): p. 1195-1205.

95. Pogson, S., P. Fox, W. O'Neill and C.J. Sutcliffe, *The direct metal laser remelting of copper and tool steel powders*. Materials Science and Engineering a-Structural Materials Properties Microstructure and Processing, 2004. **386**(1-2): p. 453-459.

96. Santosa, E.C., Masanari Shiomia, Kozo Osakadaa and Tahar Laouib, *Rapid manufacturing of metal components by laser forming*. International Journal of Machine Tools and Manufacture, 2006. **46**(12-13): p. 1459-1468

97. Savalani, M.M., L. Hao, Y. Zhang, K.E. Tanner and R.A. Harris, *Fabrication of porous bioactive structures using the selective laser sintering technique.* Proceedings of the Institution of Mechanical Engineers Part H-Journal of Engineering in Medicine, 2007. **221**(H8): p. 873-886.

98. Rehme, O., C. Emmelmann and D. Schwarze, *Selective Laser Melting of lattice structures in solid shells*, in *Virtual and Rapid Manufacturing - Advanced Research in Virtual and Rapid Prototyping*, P.J. Bartolo, et al., Editors. 2008. p. 529-535.

99. Salmoria, G.V., J.L. Leite, C.H. Ahrens, R.A. Paggi and A. Lago, *Manufacture by selective laser sintering of functionally graded PA6/PA12 components with applications in antiffiction materials*, in *Virtual and Rapid Manufacturing - Advanced Research in Virtual and Rapid Prototyping*, P.J. Bartolo, et al., Editors. 2008. p. 313-317.

100. Liu, B., J. Cheng, P.K. Bai and J.H. Wang, *Mechanical and thermal properties testing of rapid prepared molybdenum/copper composites*, in *Istm/2005: 6th International Symposium on Test and Measurement, Vols 1-9, Conference Proceedings*, T.D. Wen, Editor. 2005. p. 4663-4666.

101. Shishkovsky, I.V., L.T. Volova, M.V. Kuznetsov, Y.G. Morozov and I.P. Parkin, *Porous biocompatible implants and tissue scaffolds*

synthesized by selective laser sintering from Ti and NiTi. Journal of Materials Chemistry, 2008. **18**(12): p. 1309-1317.

102. Wehmoller, M., P.H. Warnke, C. Zilian and H. Eufinger, *Implant design and production - a new approach by selective laser melting*, in *Cars 2005: Computer Assisted Radiology and Surgery*, H.U. Lemke, et al., Editors. 2005. p. 690-695.

103. Beal, V.E., P. Erasenthiran, C.H. Ahrens and P. Dickens, *Evaluating the use of functionally graded materials inserts produced by selective laser melting on the injection moulding of plastics parts.* Proceedings of the Institution of Mechanical Engineers Part B-Journal of Engineering Manufacture, 2007. **221**(6): p. 945-954.

104. Shishkovsky, I., I. Yadroitsev, P. Bertrand and I. Smurov, *Alumina-zirconium ceramics synthesis by selective laser sintering/melting.* Applied Surface Science, 2007. **254**(4): p. 966-970.

105. Gahler, A., J.G. Heinrich and J. Gunster, *Direct laser sintering of Al2O3-SiO2 dental ceramic components by layer-wise slurry deposition.* Journal of the American Ceramic Society, 2006. **89**(10): p. 3076-3080.

106. Wua, B.Q. and A. Kumar, *Extreme ultraviolet lithography: A review.* Journal of Vacuum Science & Technology B, 2007. **25**(6): p. 1743-1761.

107. Killi, S., *Custom design, more than custom to fit!*, in *Virtual and Rapid Manufacturing - Advanced Research in Virtual and Rapid Prototyping*, P.J. Bartolo, et al., Editors. 2008. p. 777-783.

108. Bassoli, E., A. Gatto, L. Iuliano and M.G. Violante, *3D printing technique applied to rapid casting.* Rapid Prototyping Journal, 2007. **13**(3): p. 148-155.

109. Charmeux, J.F., R. Minev, S. Dimov, E. Brousseau, E. Minev and U. Harrysson, *Benchmarking of three processes for producing castings incorporating micro/mesoscale features with a high aspect ratio.* Proceedings of the Institution of Mechanical Engineers Part B-Journal of Engineering Manufacture, 2007. **221**(4): p. 577-589.

110. Mu, J.X. and X.F. Yin, *Application of microfluidic reactors on synthesis reactions.* Progress in Chemistry, 2008. **20**(1): p. 60-75.

111. Wohler, T., *Wohlers Report 2008.* 2008, Fort Collins: Wohlers Associates Inc.

112. Fico, M., M. Yu, Z. Ouyang, R.G. Cooks and W.J. Chappell, *Miniaturization and geometry optimization of a polymer-based rectilinear ion trap.* Analytical Chemistry, 2007. **79**(21): p. 8076-8082.

113. Roy, S., *Fabrication of micro- and nano-structured materials using mask-less processes.* Journal of Physics D-Applied Physics, 2007. **40**(22): p. R413-R426.

114. Drews, M.E. and D.A. Forman, *Low cost, real-time simulation of an Unmanned Aerial Vehicle*, in *Aiaa Modeling and Simulation Technologies Conference - a Collection of Technical Papers*. 1999, Amer Inst Aeronautics & Astronautics: Washington. p. 284-292.

115. Dawson, P.H., *Quadrupole Mass Spectrometry and its Applications*. American Vacuum Society Classics. 1995, New York: AIP Press.

116. Blain, M.G., L.S. Riter, D. Cruz, D.E. Austin, G.X. Wu, W.R. Plass and R.G. Cooks, *Towards the hand-held mass spectrometer: design considerations, simulation, and fabrication of micrometer-scaled cylindrical ion traps.* International Journal of Mass Spectrometry, 2004. **236**(1-3): p. 91-104.

117. Gibson, J.R. and S. Taylor, *Prediction of quadrupole mass filter performance for hyperbolic and circular cross section electrodes.* Rapid Communications in Mass Spectrometry, 2000. **14**(18): p. 1669-1673.

118. Badman, E.R., R.C. Johnson, W.R. Plass and R.G. Cooks, *A miniature cylindrical quadrupole ion trap: Simulation and experiment.* Analytical Chemistry, 1998. **70**(23): p. 4896-4901.

119. Yin, W.W., M. Wang, A.G. Marshall and E.B. Ledford, *Experimental Evaluation of a Hyperbolic Ion Trap for Fourier-Transformation-Cyclotron Resonance Mass-Spectrometer.* Journal

of the American Society for Mass Spectrometry, 1992. **3**(3): p. 188-197.

120. Taylor, S. and R.F. Tindall, *Silicon based Quadrupole Mass Spectrometry using Microelectromechanical Systems.* J. Vac. Sci Technol. B, 2001(19): p. 557-562.

121. Wapelhorst, E.H. and J.P. Müller, *A Fully Integrated TOF Micro Mass Spectrometer.* J. Complex MEMS Sensors and Actuators A, 2007: p. 138, 22-27.

122. Pau, S.P., C. S.; Low, Y. L.; Moxom, J.; Reilly, P. T. A.; Whitten, W. B.; Ramsey, J. M., *Microfabricated Quadrupole Ion Trap for Mass Spectrometer Applications.* Phys. Rev. Lett, 2006. **96**: p. 120801.

123. Van Amerom, F.H.W.C., A.; Cardenas, M.; Bumgarner, J.; Short, , *R.T. Microfabrication of Cylindrical Ion Trap Mass Spectrometer Arrays for Handheld Chemical Analyzers.* Chem. Eng. Comm, 2008(195): p. 98-114.

124. Song, Y.W., G.; Song, Q.; Cooks, R. G.; Ouyang, Z.; Plass, W, *Novel Linear Ion Trap Mass Analyzer Composed of Four Planar Electrodes.* J. Am. Soc. Mass Spectrom, 2006. **17**: p. 631-639.

125. Austin, D.E.W., M.; Tolley, S. E.; Maas, J. D.; Hawkins, A. R.; Rockwood, A. L.; Tolley, H. D.; Lee, E. D.; Lee. M. L., *Halo Ion Trap Mass Spectrometer.* Anal. Chem, 2007(79): p. 2927-2932.

126. Bower, C.A., K.H. Gilchrist, J.R. Piascik, B.R. Stoner, S. Natarajan, C.B. Parker, S.D. Wolter, J.T. Glass and *On-Chip Electron Impact Ion Source using Carbon Nanotube Field Emitters.* Appl. Phys. Lett., 2007. **90**: p. 124102.

127. Dixon, R.H.T., *Powder Metallurgy for Engineers.* 1971, London: The Machinary Publishing Co.

128. Tonshoff, H.K., A. Ostendorf, K. Korber and A. Beil, *Flexible machining system to produce micro prototypes*, in *Micromachining and Microfabrication Process Technology Vi*, J.M. Karam and J. Yasaitis, Editors. 2000, Spie-Int Society Optical Engineering: Bellingham. p. 182-192.

129. Wang, F., J. Mei and X.H. Wu, *Direct laser fabrication of Ti6Al4V/TiB.* Journal of Materials Processing Technology, 2008. **195**(1-3): p. 321-326.

130. Interrante, L.V. and M.J. Hampden-Smith, *Chemistry of Advanced Materials An Overview.* 1998, New York: Wiley-VCH.

131. Goodhew, P.J. and F. Humphreys, *Electron Microscopy and Analysis.* 1988, London: Taylor and Francis.

132. Guanghan, W.X., Xiang Jiang, and Darius Nikanpour, *Measurement of specific heat, latent heat and phase transformation temperatures of shape memory alloys.* High temperatures-high pressures, 2007. **37**: p. 91-107.

133. Chiang, L.J., C.H. Li, Y.F. Hsu and W.H. Wang, *Effects of thermal cycling on multiple-stage transformation in Ti49.3Ni50.7 shape memory alloy.* Journal of Alloys and Compounds, 2008. **462**(1-2): p. 47-51.

134. Khalil-Allafi, J., A. Dlouhy and G. Eggeler, *Ni4Ti3-precipitation during aging of NiTi shape memory alloys and its influence on martensitic phase transformations.* Acta Materialia, 2002. **50**(17): p. 4255-4274.

135. Poon, R.W.Y., J.P.Y. Ho, X.Y. Liu, C.Y. Chung, P.K. Chu, K.W.K. Yeung, W.W. Lu and K.M.C. Cheung, *Anti-corrosion performance of oxidized and oxygen plasma-implanted NiTi alloys.* Materials Science and Engineering a-Structural Materials Properties Microstructure and Processing, 2005. **390**(1-2): p. 444-451.

136. Agarwala, M., D. Bourell, J. Beaman, H. Marcus and J. Barlow, *Direct selective laser sintering of metals.* Rapid Prototyping Journal, 1995. **1**: p. 26-36.

137. Gall, K., N. Yang, H. Sehitoglu and Y.I. Chumlyakov, *Fracture of precipitated NiTi shape memory alloys.* International Journal of Fracture, 2001. **109**(2): p. 189-207.

138. Frick, C., A. Ortega, J. Tyber, K. Gall and H. Maier, *Multiscale structure and properties of cast and deformation processed*

polycrystalline NiTi shape-memory alloys. Metallurgical and Materials Transactions A, 2004. **35**(7): p. 2013-2025.

139. Kroger, A., R. Wernhardt, C. Somsen, G. Eggeler and A. Wieck, *In situ transmission electron microscopy-investigations on the strain-induced B19 '-phase in NiTi shape memory alloys structured by focused ion beam.* Materials Science and Engineering a-Structural Materials Properties Microstructure and Processing, 2006. **438**: p. 513-516.

140. Cuevas, F., M. Latroche, F. Bourée-Vigneron and A. Percheron-Guégan, *A conjoint XRD-ND analysis of the crystal structures of austenitic and martensitic Ti0.64Zr0.36Ni hydrides.* Journal of Solid State Chemistry, 2006. **179**(11): p. 3295-3307.

141. Tobushi, H., Y. Ohashi, T. Hori and H. Yamamoto, *Cyclic deformation of TiNi shape-memory alloy helical spring.* Experimental Mechanics, 1992. **32**(4): p. 304-308.

142. Smith, W.A., A. Shaulov, and B. A. Auld,, *Tailoring the properties of composite piezoelectric materials.* IEEE Ulfrason.Symp, 1985: p. 642-647.

143. Mustofa, S., T. Araki, T. Furusawa, M. Nishida and T. Hino, *The PLD of BaTiO3 target produced by SPS and its electrical properties for MLCC application.* Materials Science and Engineering B-Solid State Materials for Advanced Technology, 2003. **103**(2): p. 128-134.

144. Sanjurjo, J.A., R.S. Katiyar, S.P.S. Porto, , *Temperature dependence of dipolar modes in ferroelectric BaTiO3 by infrared studies.* Phys. Rev. B, 1980. **22**(2396).

145. Envisiontec. *R5 Material Properties Data Sheet.* 2007 [cited 2009 15 January]; Available from: www.stratatec.co.nz/material-properties-sheets/r5-r11.pdf.

146. Chan, H.L. and J.UNSWORTH, *Simple Model for Piezoelectric Ceramic/Polymer 1-3 Composites Used in Ultrasonic Transducer Applications.* IEEE Transactions on Ultrasonics, Ferroelctrics and Frequency Control, 1989. **36**(4): p. 7.

147. Bowen, C.R., A. Perry, H. Kara and S.W. Mahon, *Analytical modelling of 3-3 piezoelectric composites.* Journal of the European Ceramic Society, 2001. **21**(10-11): p. 1463-1467.

148. Consort, *BS EN ISO 527-2: Plastics —Determination of tensile properties Part 2: Test conditions for moulding and extrusion plastics*, B. standard, Editor. 1996.

149. Grimm, T., *User's Guide to Rapid Prototyping.* 2004, Society of Manufacturing Engineers.

150. CPO-Programs. 2009 [cited 2009 January 20th]; Available from: www.electronoptics.com.

151. Gibson, J.R.T., S.; Leck, J. H, *Detailed Simulation of Mass Spectra for Quadrupole Mass Spectrometer Systems.* J. Vac. Sci. Technol. A, 2000. **18**: p. 237-243.

152. Turchette, Q.A.K., D.; King, B. E.; Leibfried, D.; Meekhof, D. M.; Myatt, C. J.; Rowe, M. A.; Sackett, C. A.; Wood, C. S.; Itano, W. M.; Monroe, C.; Wineland, D. J., *Heating of Trapped Ions From the Quantum Ground State.* Phys. Rev. A, 2000. **61**: p. 063418.

153. Taylor, S. and J.R. Gibson, *Prediction of the Effects of Imperfect Construction of a QMS Filter.* J. Mass Spectrom., 2008. **43**: p. 609-616.

154. Associates, W. *Organisational Meeting for Proposed New ASTM Activity on Additive Manufacturing Technologies.* 2009 [cited 5th March 2009]; Available from: http://wohlerassociates.com/agenda.pdf.

155. Youssef, E.A., *Imaging Properties of a Novel Electristatic Lens.* Canadian Journal of Physics, 1971. **49**(21): p. 7.